PRESSURE LOSSES EXPERIENCED BY LIQUID FLOW THROUGH PDMS MICROCHANNELS WITH ABRUPT AREA CHANGES

by

JONATHAN D. WEHKING
B.S. University of Central Florida, 2005

A thesis submitted in partial fulfillment of the requirements
for the degree of Masters of Science in ThermoFluids
in the Department of Mechanical, Materials, and Aerospace Engineering
in the College of Engineering and Computer Science
at the University of Central Florida
Orlando, Florida

Summer Term
2008

ABSTRACT

Given the surmounting disagreement amongst researchers in the area of liquid flow behavior at the microscale for the past thirty years, this work presents a fundamental approach to analyzing the pressure losses experienced by the laminar flow of water (Re = 7 to Re = 130) through both rectangular straight duct microchannels (of widths ranging from 50 to 130 micrometers), and microchannels with sudden expansions and contractions (with area ratios ranging from 0.4 to 1.0) all with a constant depth of 104 micrometers. The simplified Bernoulli equations for uniform, steady, incompressible, internal duct flow were used to compare flow through these microchannels to macroscale theory predictions for pressure drop. One major advantage of the channel design (and subsequent experimental set-up) was that pressure measurements could be taken locally, directly before and after the test section of interest, instead of globally which requires extensive corrections to the pressure measurements before an accurate result can be obtained. Bernoulli's equation adjusted for major head loses (using Darcy friction factors) and minor head losses (using appropriate K values) was found to predict the flow behavior within the calculated theoretical uncertainty (~12%) for all 150+ microchannels tested, except for sizes that pushed the aspect ratio limits of the manufacturing process capabilities (microchannels fabricated via soft lithography using PDMS). The analysis produced conclusive evidence that liquid flow through microchannels at these relative channel sizes and Reynolds numbers follow macroscale predictions without experiencing any of the reported anomalies expressed in other microfluidics research. This work also perfected the delicate technique required to pierce through the PDMS material and into the microchannel inlets, exit and pressure ports without damaging the microchannel. Finally, two verified explanations for why prior

researchers have obtained poor agreement between macroscale theory predictions and tests at the microscale were due to the presence of bubbles in the microchannel test section (producing higher than expected pressure drops), and the occurrence of localized separation between the PDMS slabs and thus, the microchannel itself (producing lower than expected pressure drops).

I am indebted to my father and mother for encouraging the pursuit and support of advanced education. I am thankful for Chase's unwavering dedication and tireless persistence in our microfluidics research efforts. I am blessed that this work indirectly led me to the most important person in my life, Rebekah. Finally, through this work, I am reinvigorated and renewed by what it means to discover, and most importantly, to do what you love in your chosen vocation.

TABLE OF CONTENTS

LIST OF FIGURES

LIST OF TABLES

LIST OF ACRONYMS/ABBREVIATIONS

CAD	Computer Aided Design
CFD	Computation Fluid Dynamics
Kn	Knudsen number: Ratio of mean free path over channel length
MEMS	Micro Electro Mechanical Systems
Micron	Abbreviation for micrometers
PDMS	Poly(DiMethylSiloxane): A type of silicon used to cast microchannels
Po	Poiseuille number: Measure of flow resistance
PSI	Pounds per Square Inch: A unit of pressure
Re	Reynolds number: A non-dimensional ratio of viscous and inertial forces

CHAPTER ONE: INTRODUCTION

It is the nature of human beings to pack common everyday entities into ever decreasing amounts of space. Sparse amounts of people that once roamed miles upon miles of open land are now more frequently packed into a few acres of homes, town homes, or even vertically stacked abodes called apartments. Forms of currency, which conventionally appeared as tangible objects representing a specific value, have taken the more common form of signatures, bits and bytes, and plastic cards. Books and documents representing the latest advances in human discovery that were once stored in high security vaults, simply because they had yet to be copied and distributed to the masses, have been replaced by .doc and .pdf files., theoretically taking up no physical space whatsoever! Origins of the necessities for survival, food, water, and rest, must be overly abundant and within a few steps away for everyday life to be considered normal. And of course, there have been light years worth of advances in the area of processing and storing data electronically utilizing microchips. Wouldn't it be inconvenient not have any room for your bed because the equivalent of your laptop computer is taking up the majority of your bedroom? Whether it be the ever looming notion of possibly overcrowding the Earth with people that keeps this "minimalist" thinking hardwired into the subconscious part of the human brain, or the simple need to manipulate the law of conservation of space, the consistent requirement for making effects fit into smaller and smaller physical volumes is ever pressing on the advancement of scientific discovery.

Such is the case with all artifacts associated or connected with the miniaturization race. If a microchip decreased in size by 50%, would it make sense to still use the same CPU fan that

cooled its predecessor? The original fan would still be 50% larger than the new smaller chip, making the decrease in size of the overall system less significant. An additional field that contains cooling as one of its possible uses, and that has recently joined the miniaturization race, is the flow of fluids through miniaturized geometries. These miniaturized geometries have been dubbed microchannels, and will be referred to as such for the remainder of this work. The focus on fluid flow through microchannels developed as a result of numerous requirements spawning from a multitude of fields. Given their macro scale counterparts, including everyday brass or PVC plumbing pipes, microchannels arouse as more of a reaction to shrinking counterparts, such as microchips, micro-spray nozzles, and technological advances in prosthetics . Biomedical necessities include the modeling of various bodily fluids flowing through both naturally grown and artificially manufactured bodily chambers, namely lung alveoli, and glomerular filtration systems in the kidneys [1]. More rigorous mechanical applications include the modeling of flow parameter requirements and pressure losses as a result of pumping, cooling, or mixing uses of various liquids and gasses [2]. The volumetric and mass limitations of space travel due to extreme costs make miniaturized systems extremely attractive [3]. Wherever their use, microchannels are becoming increasingly popular in a plethora of scientific fields.

The types of microchannels available for study today are as numerous as their potential uses. Any macroscale parent geometry available is most certainly available in a "micro-version" equivalent, making this field an overly abundant resource in research topics. For this reason, the scope of this work is limited further by the type of geometry being studied, namely sudden expansion and sudden contraction microchannels. One apparent reason for this selection is that sudden changes in geometry represent a geometric "bridge" between flow possibly beginning as macroscale, and potentially ending as microscale, depending on the size order of magnitude.

The link between these two orders of fluidic magnitude is analogous to the ever ambiguous link between two other types of flow: laminar and turbulent flow, or the transition flow regime. For the sake of clarity, the laminar flow regime will be used for the duration of this work, as added layers of complexity are not yet warranted. It is the purpose of this work to develop a simple working microfluidic model of a sudden expansion/contraction flow system for use in extrapolating accurate and meaningful flow parameter data.

CHAPTER TWO: LITERATURE REVIEW

The following section will present an all-encompassing review of the relevant literature and theory associated with the methodology and analysis presented in anon sections of this work. First, a summary of current efforts in the microfluidics arena will be presented, followed by briefly discussing any relevant manipulations of flow theory that may be used to baseline microchannel flow modeling. Then, a significant paper by F.F. Abdelall et al. [4] that focuses on modeling two-phase flow through sudden expansion/contraction microchannels will be offered, as the geometry studied in Abdelall's work is very similar in configuration to the geometry utilized in this work.

Straight Duct Microchannels

One of the most complete and all encompassing compendiums of MEMS literature is the MEMS Handbook, edited by Mohamed Gad-el-Hak. In the chapter entitled "Liquid Flow in Microchannels," one of the primary researchers in microfludics (K. V. Sharp et al.), gives a fairly detailed overview of the field, starting with the long list of potential applications that may result from discoveries in microfluidics research. The authors then proceed to address the question of when it is suitable to legitimately discount macroscale hydrodynamics and fluid mechanics in favor of velocity slip conditions and free molecular flow analysis techniques. Then, an overview of macroscale fluid mechanics is given for pressure driven internal flow. These equations and derivations represent the foundational assumptions, theories, and flow behaviors of Newtonian fluids, and can be found in most introductory textbooks on the subject [5, 6]. Finally, the authors

have a section devoted to the undeniable trend of discord among results obtained in microfluidics research to date as to whether or not macroscale fluid mechanics adequately models flow at the microscale. This disagreement in the field has as created an unsettling debate over how to handle flows when designing duct networks, MEMS devices, and any other applicable use for transporting liquids through small channels. How can humanity progress further in this direction when there is conflict at its very foundation?

There are plenty of theories as to why researchers are getting anomalies in their various experiments, but the authors of this highly controversial chapter in the MEMS Handbook do a great job of simply presenting the tangible findings of the other works' discussed, leaving all interpretation of these findings for the individual researchers to justify. They classified the findings into three categories, all of which compare experimental results for the friction factor (and subsequent pressure drop) of the flow to theoretical predictions from macroscale fluid mechanics. The first category is experimental results that predicted a friction factor higher than what theory depicts. The second is experimental results in agreement with macroscale friction factor predictions, and the third is experiments that show lower than expected friction factors when compared to classic macroscale fluid mechanics. The channel flow geometries were all straight ducts, of various cross-sectional areas (circular, trapezoidal, rectangular, etc.), exhibiting laminar flow ranges for the Reynolds number. Figure 1 represents the resulting parameter space for this comparison, and Figure 2 shows a sample of the experimental results for the normalized friction factor, a classic quantity representative of macro theory, and a quantity that will be discussed in greater detail in later sections.

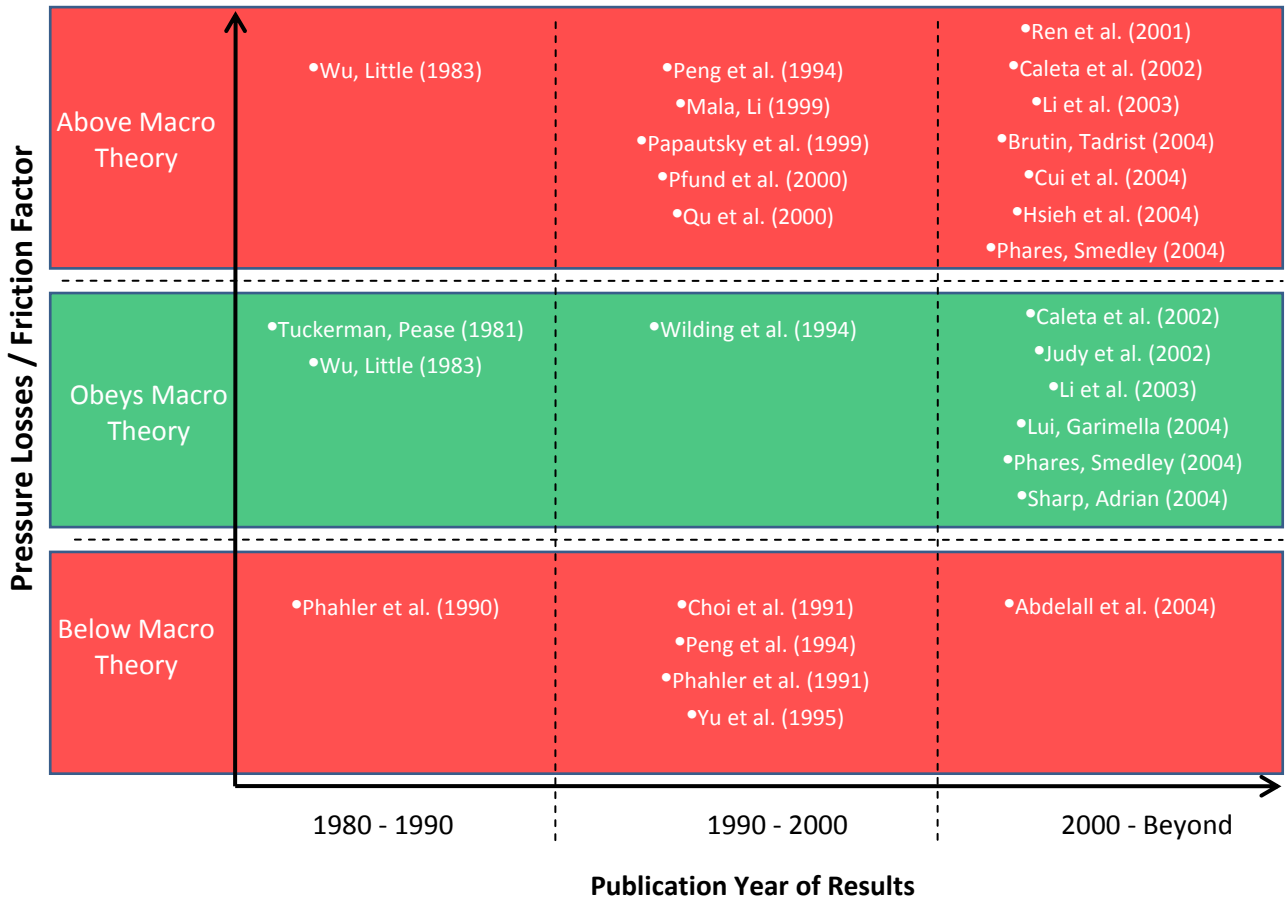

Figure 1: Parameter space of experimental flow behavior in straight ducts. Data from [7].

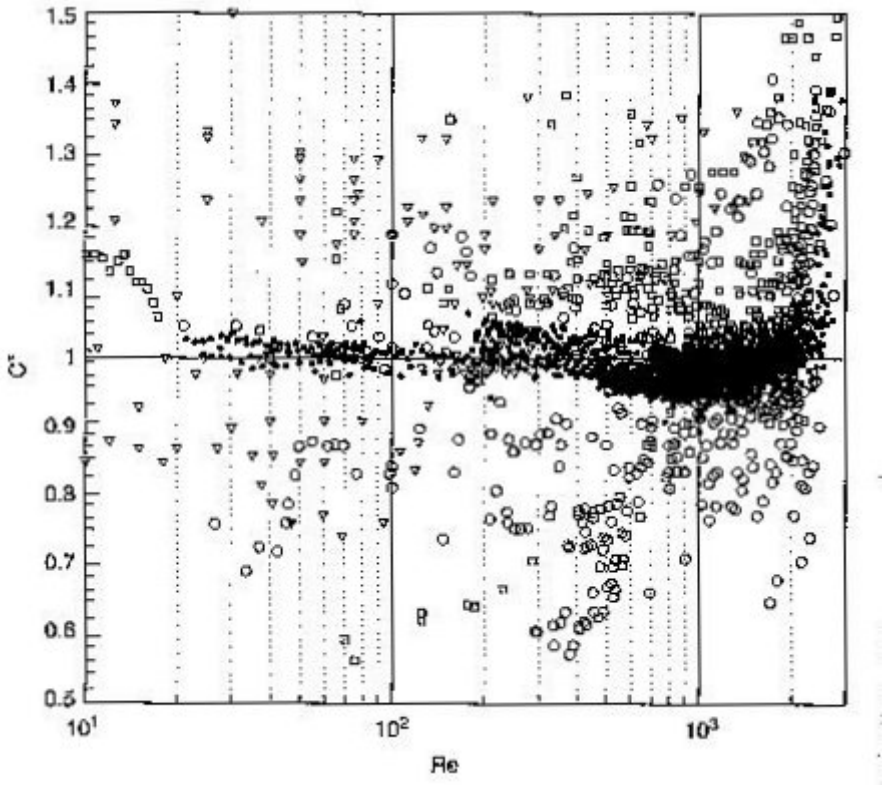

Figure 2: Plot of experimental results from prior research for the normalized friction factor [7].

With reference to the scatter of data points in Figure 2, each plotted shape represents results from a different research effort. Results that were claimed to follow macroscale predictions fell on or around the horizontal centerline marking a unity normalized friction factor ($C^*=1$), which is described below by Equation 1.

$$C^* = \frac{(f \cdot Re)_{experimental}}{(f \cdot Re)_{theoretical}} \qquad \textbf{Equation 1}$$

Data points that fell above this line were said to predict results above that of macroscale theory, and data points that fell below were said to predict results lower than macroscale theory.

It is also interesting to note the trend over time of the efforts in this field (gathered form Figure 1). From the early 1990's to 2000, most of the research showed disagreement from macroscale fluid mechanics tracking pressure drop behavior either above or below macroscale predictions. It is hypothesized that as more and more researchers were finding that liquid flows at small scales were potentially unable to be predicted by classical fluid mechanics, even more efforts were coordinated and initiated to find out if this was in fact true, and what phenomena could be causing this critical notion. As efforts increased, and time approaches present day the split in findings now appears to be between results that are in agreement with macroscale theory, and results that are exhibiting higher than normal friction factors and pressure drops.

The following discussions delve into some of these individual research efforts, offering currently popular explanations as to why experimental results are differing from what theory predicts, when warranted.

Early Transition to Turbulence

Rands et al. [8] was primarily concerned with quantifying the transitional flow regime in microfluidics, and mapping any deviations experienced from macroscale predictions. The incentive for such an investigation was stated to be the increase in driving pressure requirements for turbulent flow becoming even greater than the already high driving pressure values of laminar flow through microtubes. The classical macro laminar Reynolds number/friction factor product for circular flow sections (Equation 2) was examined for the different tube diameters over Reynolds numbers ranging from 300 to 3400 to examine at what Reynolds number(s) departure from this value occurred, if any.

$$f \cdot Re = 64 \qquad \textbf{Equation 2}$$

Another independently calculated result of this work based on the fluid mixed-mean temperature reaffirmed the results: the viscous heating parameter (=32 for Equation 2) was considered as secondary proof of the observed transition Reynolds number(s) deduced from the frictional measurements. They found that transition to turbulence occurred at approximately Re = 2100 to Re = 2500 for all tube sizes, which was considered consistent with macroscale behavior, and that uncertainty in frictional calculations/measurements were 16-29%, dominated by $\pm$ 1 micrometer diameter tolerance. Uncertainties in the viscous heating calculations/measurements were not stated, though it is important to note that the thermocouple used for temperature measurements was not directly placed in the working fluid (but rather on the outside surface). It was concluded that the critical Reynolds number may increase slightly with decreasing diameter [8].

Xu et al. [9] focused on numerically simulating fully developed turbulent flow of water through microtubes on the size order of 50 micrometers to 254 micrometers in diameter. The incompressible, two-dimensional, steady, time averaged Navier-Stokes equations of momentum and continuity, along with Wolfshtein's one-equation turbulence model for kinetic energy were used. All equations were simplified where applicable, coupled, solved iteratively, and compared to a convergence factor until convergence was satisfied. It was determined that transition to turbulence occurred at lower Reynolds numbers for smaller microchannel diameters (which is in agreement with Rands et al. [8]), proposing the notion that microtubes with larger diameters have stronger turbulence effects. Also, for lower Reynolds numbers, the turbulent velocity profiles

were very close to laminar velocity profiles, and that with larger diameters, and higher Reynolds numbers, the velocity profile approaches that of a typical macro velocity profile (somewhat flat-topped). It was concluded that micro-flow phenomena should be considered for diameters smaller than 130 micrometers, offering a concrete cut-off point for when to switch from macroscale theory to microscale theory [9].

Mixing Fluids in Microchannels

Decre'e et al. [10] were interested in decreasing the mix time/length of two incompressible liquids through channels on the order of 65 x 320 micrometers in size. The idea was to microfabricate a microchannel on a rotating disc in order to take advantage of the centrifugal forces to drive the liquids down the channel, and enhance mixing using the Coriolis forces inherent to the rotating frame. Incompressible, steady state Navier-Stokes and continuity equations were modified to account for the rotating "disk frame," incorporating the centrifugal field as a flow driver and Coriolis effects as a flow mixer. The flow was first simulated using computer programs, then compared to experimental trials. It was concluded that key parameters impacting Coriolis mixing capabilities are channel length, aspect ratio and rate of rotation, and as rotational speed increases, mixing is enhanced for channels of identical length. Also, as aspect ratio decreases, decrease in diffusion time is proportional to the square decrease in diffusion length.

Sudarsan and Ugaz [11] also looked into effective ways of mixing two fluids using an array of spiral microchannels on the order of 49 micrometers in size. Mixing of blue and yellow food dyes was evaluated by the amount of green color that was generated when two streams

mixed, providing a percentage of mixing for the different trials. There were five different spiral designs, which varied the number of arcs, and length of the mixing section for Reynolds numbers between 0.02 - 18.6 (very low flow rates, 0.0001 to 0.1 mL/min). Trials of a single spiral design, along with trials of three spiral designs connected in series were measured for intensity of mixing. A two-arc spiral channel with a sudden expansion was also examined for a possible mixing geometry. It was found that at lower flow rates, diffusion is the primary mechanism by which mixing occurs, and that at higher flow rates, secondary Dean effects come into play and contribute to increased levels of mixing. Centrifugal effects are strongest at the innermost regions of the spiral (highest percentage of mixing), and by abruptly increasing the cross-sectional area of the spiral, expansion vortices result and can be harnessed to further reduce overall mixing lengths. Subsequently, the footprint of the mixing area is significantly reduced than if straight channels were used, thus concluding that the benefits of Dean effects (due to centrifugal forces) reduces the required overall mixing length [11].

Goullet et al. [12] considered the use of "pulse mixing" of two fluids for microchannels around 160 micrometers in size, and for a Reynolds number range of 0.3 to 30. The study was a completely numerical Fluent simulation that consisted of four different flow geometries with separate entry ports for the two fluids (perpendicular, Y, T, and arrowhead shaped), and 1 configuration with bends around all 3 spatial axes where both fluids have the same entry point. A modification was made to the perpendicular flow geometry for one experiment by adding ribs. Navier-Stokes and continuity equations were used for the simulation, and no supporting experiments were performed. The idea was to view how much more effective the fluid confluence and geometrically induced secondary flows were to mixing opposed to diffusion alone. It was discovered that for geometries with different entry ports, pulsing the flow 90^{o} out

of phase enhanced mixing by promoting chaotic advection, also, adding ribs to the perpendicular flow trial coupled with out of phase pulsing further enhanced mixing (0.78 degree of mixing, with 1.0 being completely mixed). Increasing pulse frequency from 5 to 20 Hz increased the degree of mixing by 0.2, and increased mean velocity for the tri-axial geometric case also assisted with constituent mixing.

Heat Exchanger Benefits

Niklas et al. [13] conducted an investigation utilizing a row of 54 triangular shaped microchannels for possible micro-heat exchanger applications. However, the hydraulic properties of the fluid through the microchannels was the main focus of the work. Size was on the order of 110 micrometers (hydraulic diameter), and flow rate was on the order of $Re < 1000$. First, experiments were carried out to see how accurate the set-up would be to the classical fully-developed laminar Poiseuille number (flow resistance) of 13.3. Then, numerical simulations were carried out in Fluent to show agreement or disagreement to this value due to a number of loss criteria. It is important to note that the different types of losses simulated were only observed individually, and never compounded (or layered) in an effort to show individual contributions from each. Experimental results showed departure from $Po = 13.3$ at about $Re = 10$, and is claimed to be the result of early transition to turbulence. Additionally, an uneven flow rate between the microchannels was observed because of the fluid entrance and exit ports to the flow inlet/outlet reservoirs. Therefore, uses in heat exchanger applications were deemed futile given this particular work's experimental set-up and models. Table 1 presents an outline of quantifiable pressure loss contributions accumulated during this work [13].

Table 1: Fluent Simulations with applicable pressure losses.

Fluent Geometry	Simulation	% Contribution to Pressure Loss
Single Microchannel	Viscous Losses	20%
"	Entrance Effects (BL)	5%
"	Local Losses	20%
Microchannel Network	Mixing	30%
"	Recirculation	80%

Flow Effects at Small Scales

Koo and Kleinstreuer [14] were primarily concerned with numerical simulations of water through microchannels at or around 100 micrometers in hydraulic diameter, and investigating which macroscale effects remain predominant in microscale flow modeling. First, seemingly out of courtesy for the field (and the reader, of course) the author grouped the related microchannel investigatory literature thus far into three observational areas when considering friction factor/pressure gradient changes in microchannels: 1) early transition to turbulence, 2) surface phenomena (roughness, electrokinetic forces, temperature effects, microcirculation near the wall), and 3) no differences when compared to conventional macroscale flow theory. This work then sought to provide a list of flow effects to be considered (with subsequent justification) when modeling microfluidic flow behavior based on a numerical simulation. The equations used included the Navier-Stokes equations (for continuity and momentum), Fanning and Darcy friction factor relations, low Reynolds number k-w model modifications to the Navier-Stokes equations (for investigating turbulence), and the energy equation to extrapolate thermal effects. Table 2 summarizes the six flow effects evaluated, with a recommendation as to whether or not the effect should be considered based on the results obtained.

Table 2: Flow effects considered with results/recommendations.

Effect	Should it be considered?	Rationale
Entrance	Yes	A function of channel length, aspect ratio and Reynolds number.
Non-Newtonian	Yes	Important for polymeric liquids and particle suspension flows.
Wall Slip	No	Average slip velocity accounted for only 0.0014% of the average fluid velocity.
Surface Roughness	Yes	A function of the Darcy number, Reynolds number, and cross-sectional configurations.
Turbulence	Yes	Important for Reynolds numbers above 1000 (less than conventional macroscale theory), and are evident with geometric contractions in the channels.
Viscous Dissipation	Yes	Taken into account for channels with less than 100 micron hydraulic diameters.

Celata et al. [15] investigated the possibility of wall roughness effects and geometric deviations for microtubes ranging from 31 to 326 micrometers. The intent was to model how accurately fluid flow behaved in accordance with the classical Hagen-Poiseuille flow (refer to Equation 2) for different diameter microtubes, and to possibly see around what size deviation from this accepted flow model occurred. Different materials including fused silica, glass (with siliconated, roughened, and untouched inner diameters), and Teflon were considered creating a matrix of 10 different trials/experiments. An uncertainty analysis was carried out for the Darcy equation, and a slip parameter (β) was incorporated into the laminar velocity profile equation to extrapolate a modified Darcy equation. It was found that adherence to Hagen-Poiseuille was verified for all size microtubes for Re > 300 and at the microscopic scale, geometric non-uniformities have a greater impact on comparison inaccuracies than surface roughness. In fact,

roughened channels did not show any diversion from classic predictions. In addition, slip effects encountered by other researchers were proposed (though not verified) to most likely be the result of an undetected presence of desorbed nanobubbles on the hydrophobic surface. It was also concluded that viscous heating becomes important at diameters below 100 micrometers (influences Reynolds number through changes in fluid viscosity).

Steinke and Kandlikar [16] presented a conference proceeding constructed for the purpose of compiling a historiography of the current microchannel research. The author created a database comprised of over 40 different papers that compared year of publication, subject fluid, shape and size of channel, Reynolds number, non-dimensionalized friction factor, treatment of heat transfer (adiabatic or not), and if the experiments accounted for losses in their calculations. The final parameter was if the measurements were in agreement with numerical computations for classical laminar flow theory. The authors then created their own experimental set-up, and measured the pressure drop across a microchannel on the size order of about 200 micrometers and a Reynolds number range of Re = 0 to Re = 800. An uncertainty discussion was also included. The trend in the database was that experiments and subsequent calculations that did not account for entrance/exit losses, developing region, and frictional losses showed disagreement with classical theory. Also, the uncertainty analysis indicated a $\pm$ 40% deviation, with the size parameter accounting for the highest contribution to this result. From the authors' experiments, departure from conventional laminar flow theory occurred around a Reynolds number of 300, and is explained as an early transition to turbulence [14]. Considering the conclusions offered by Xu et al. that microscale theory should be considered around a size of 130 micrometers [9], it would seem that Steinke’s work provides a specific flow regime limit to

supplement this size regime limit for when to begin expecting the onset of microscale flow phenomena.

Qu et al. [17] concentrated on flow development and pressure drop for water in a 222 x 694 micrometer microchannel for Reynolds numbers ranging 196 to 2215. Micro-particle image velocimetry (microPIV) was used to capture and extrapolate the flow development, and velocity field contour plots were created based on each of the different flow rates. Pressure drop was measured using pressure transducers strategically placed at either end of the microchannel. Numerical results were also obtained in order to facilitate the mapping of velocity fields and pressure drop values using the coupled Navier-Stokes and continuity equations. The SIMPLE algorithm was employed utilizing a Gauss-Seidel iterative solution method. Overall, there was fairly good agreement between model predictions and the measured velocity field. Also, numerical, experimental, and theoretical correlations all showed good agreement for pressure drop when considering inlet contractions, outlet expansion, and developing region effects. The authors claimed that given the proper treatment and inclusion of all major and minor loss considerations, the Navier-Stokes equations are more than sufficient for predicting liquid flow in microchannels [17].

Bahrami et al. [18] focused on developing a new technique of modeling flow through rough microtubes and comparing this new technique with existing data from other researchers. The group utilized Hagen-Poiseuille behavior as the macroscale flow model, accounting for friction factors in their equations (major losses). Also, a new term was developed called the frictional resistance, such that the mass flow rate was represented as a function of pressure drop and this frictional resistance term only. Surface roughness was averaged and integrated both radially and axially as a Gaussian distribution of peaks and valleys around a mean radius. These

values were curve fitted in the original (but normalized) frictional resistance equation, as well as curve fitted (as a function of roughness) for an array of roughness values. The roughness values utilized were from other researchers' data, as the scope of work for these experiments involved the development and evaluation of the new frictional resistance term only. For this study, roughness was not deemed a function of microtube radius (though this may be considered a flaw). Rarefaction, compressibility, and slip-on-wall effects were assumed to be negligible, and it was found that the effects of roughness could be neglected when relative roughness contributions reached less than 3% [18].

Hansel [19], worked concurrently with the efforts of this research endeavor, and provided tremendous insight and influence into the microchannel design, size realm, test equipment selection, and experimentation philosophies that will be expounded upon in later sections. The comparison and extrapolation techniques for both Hansel's work and this work are very similar in nature, as the ultimate vision of this research group is to provide flow behavior models for all pressure loss effects experienced at the microscale using macroscale fluid mechanics equations as the initial (or default) predictor. Hansel focused on mapping pressure losses experienced by liquid flow through microchannels rectangular (approximately 100 x 100 micrometers) in cross-section for sweeping bends of various angles and radii. It was first thought that straight duct theory could be used to predict the static pressure drop without taking into account any minor loss effects due to the gradual change in flow direction. However this assumption seemed to break down past a Reynolds number of 30 due to secondary (Dean) flow effects. An empirical correlation was extrapolated based on trend observation and an exponential curve fitting algorithm for the loss coefficient through bends for $Re > 30$, the result of which can be found in

Equation 3 where θ is the channel bend angle, R is the bend radius, w is the channel width, f is the friction factor for straight ducts, and Re is the Reynolds number.

$$K_{bend} = \frac{\theta}{90deg} \cdot \left[\frac{3}{2} \cdot \left(\frac{R}{w} \right) \cdot \frac{f}{Re} + 1 \right] \qquad \textbf{Equation 3}$$

The following research group conducted analyses utilizing geometry nearly identical to the geometry presented in this work. Abdelall et al. [4] investigated the effects of abruptly increasing or decreasing the flow channel geometry using water, air, and a water/air mixture as the subject flow medium. Figure 3 portrays a sample of the geometry used in this work.

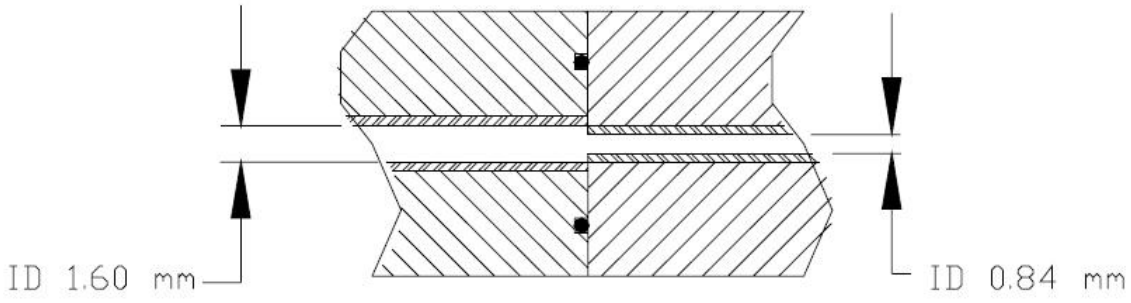

Figure 3: Schematic of geometry used in [4]. Area ratio is approximately 0.276.

Channel size was on the order of 840-1600 micrometers, and flow rates analyzed were on the order of Re = 870-12960. First, a theoretical solution for single-phase fluid flow through an

expansion/contraction was found in terms of a pressure differences. Next, a theoretical solution for two-phase flow through an expansion/contraction was found in terms of similar pressure quantities. Finally, equations in terms of the expansion/contraction coefficients were formulated with pressure difference quantities that must be determined experimentally. Equation 4 and Equation 5 show the relations used, where K is the expansion/contraction coefficient, P_2 is the pressure at the smaller diameter tube, P_1 is the pressure in the larger tube, u_1 is the fluid velocity, and σ is the area ratio.

$$K_e \cdot \left(\frac{1}{2} \cdot \rho \cdot u_1^{\,2} \right) = \left(P_2 - P_1 \right) - \frac{1}{2} \cdot \rho \cdot u_1^{\,2} \cdot (\sigma - 1) \qquad \textbf{Equation 4}$$

$$K_c \cdot \left(\frac{1}{2} \cdot \rho \cdot u_1^{\,2} \right) = -\left(P_2 - P_1 \right) + \frac{1}{2} \cdot \rho \cdot u_1^{\,2} \cdot (\sigma - 1) \qquad \textbf{Equation 5}$$

Experiments were carried out, substituted into these equations, and then compared to accepted theory of macroscale expansion/contraction geometric solutions. Vena-contracta effects were assumed to take place in the same location for both single-phase and two-phase flow solutions. The plotted results of these coefficients and subsequent comparison to macroscale predictions can be found in Figure 4 for expansion channels, and Figure 5 for contraction channels.

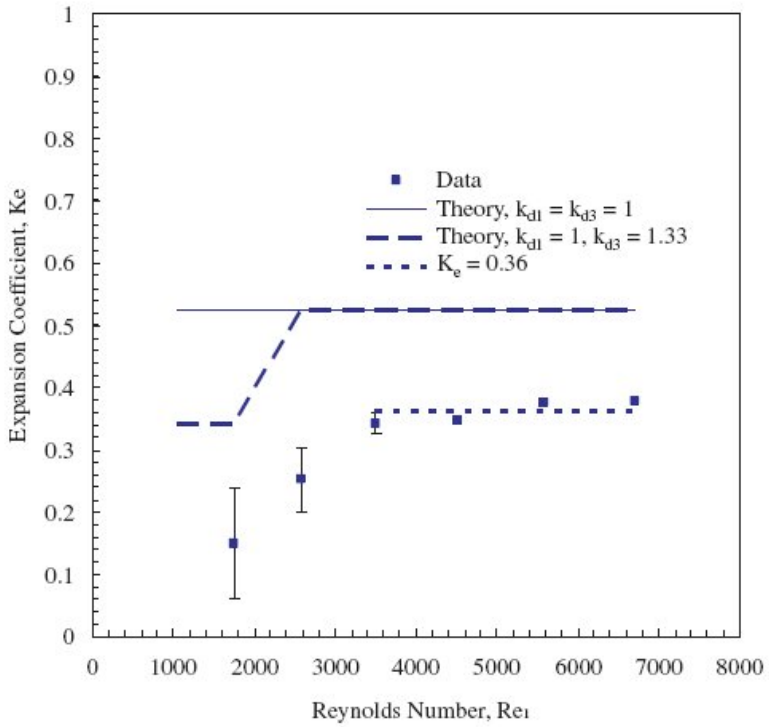

Figure 4: Expansion coefficients from [4] compared to macroscale predictions.

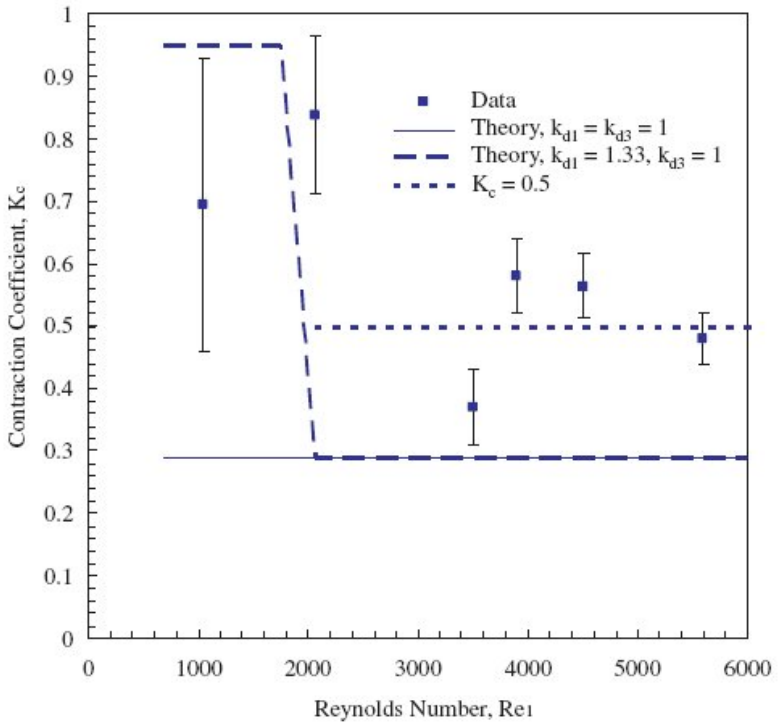

Figure 5: Contraction coefficients from [4] compared to macroscale predictions.

Expansion/contraction coefficients were examined for the single-phase (liquid) portion of the experiments, and it was found that the expansion coefficient values, K_e, fell consistently below macroscale predictions at approximately 0.36 (with theoretical values around 0.6) and the contraction coefficient values, K_c, fell consistently above macroscale predictions at approximately 0.5 (with theoretical values around 0.3). K_c for gas was a bit closer to the accepted value of 0.3. Generally, however, there was poor agreement between the values measured and accepted macroscale theory for these systems. One potential reason for such a disparity is because of the analysis conducted on the above flow geometry. Given that major losses were present in the resulting experimental set-up due to frictional effects (friction factor

straight duct losses), and because these losses carry with them an overwhelming effect on the resulting pressure drop, it is hard to separate any uncertainty in the measurement due to these major losses from the minor losses experienced due to the sudden expansion and contraction. Averages aside, simply solving for expansion and contraction coefficients (K_e and K_c, respectively) using the pressure drop data measured is siphoning all of the uncertainty into the calculations of the coefficients themselves, resulting in major inaccuracies. This effect will be taken into account in this work.

Results of the two-phase flow system in this work showed only a small offset from accepted slip flow models with vena-contracta effects considered for all Reynolds number ranges. A correlation was provided for the two-phase contraction flow losses accounting for significant velocity slip. While the focus of these experiments were primarily concerned with modeling two-phase fluidics, a portion of the resulting data, namely the single phase segments, can be used for comparison to the analysis carried out in this work.

It is by no means a hyperbole to state that there is a surfeit of prior work in the analysis and utilization of modeling flow through microchannels and microtubes. However, there still seems to be major disagreement between research groups that claim their experiments follow that of macroscale fluid mechanics, and other researchers that conclude their experiments are not adequately described by these battle-hardened theories. Subsequent sections will reveal how this work brings to light a notion that most groups seem to think is too simplistic exemplified by the field's lack of attention to it: flow modeling over simple geometry with direct pressure measurement techniques.

CHAPTER THREE: METHOLODGY

Overview

It is the ultimate aspiration of this work to provide a tangible, useful method of calculating pressure loss due to abrupt area changes in microchannels. The foremost question to answer is if the current cornerstone macroscale fluid mechanics is adequate enough to model microscale fluid flow. This is a question largely disputed amongst the current literature, where a plethora of varying results and conclusions have been elucidated and argued many times over. It is hypothesized that there are additional effects to account for in the microscale regime of fluid flow that are not typically required in macroscale fluidics. That being said, this work does not intend to explore the chasms of missing mathematics behind the theory of fluid flow through small channels in detail (provided they exist), but will hope to provide a temporary remedy to the current salvo of differing (and at times, inconclusive) solutions to microchannel fluid models. This proposed remedy (if needed) will be in the form of an empirical correlation between pressure drop and various flow parameters/properties, and supported by data collected through a barrage of controlled experiments rather than an elegant derivation beginning from first principles. It is sufficient to compare this type of empirical solution to the types of solutions for Nusselt numbers (and/or heat transfer coefficients) in the turbulent flow regime, where solutions contain relations based on other non-dimensional numbers with sometimes peculiar exponents and coefficients. When compared to their elegantly derived counterpart solutions in the laminar flow regime, the empirical "data-based" methodology behind their creation is almost immediately apparent. Continuing with this analogy, it is helpful to think of the empirical

solution for pressure drop delivered in this work as the equivalent of a microscale counterpart of the macroscale solution for common, everyday pipe flow, where the details of what differentiates the two theoretically will be left for future researchers.

Size Regime Considerations

The study of microfluidics brings with its controversy another unanswered problem: What is the relative characteristic size of a microchannel? The unwritten rule in the literature seems to be between 1 micron and 1milimeter (1 – 1000 micrometers) [7] for channel hydraulic diameters, as channels below this range are considered nanochannels, and ducts above this size range are considered normal pipes, but that still leaves the question of at what size ranges *should* the equations of macroscale fluid mechanics break down due to phenomena yet unknown?

In the field of gas dynamics, there is a non-dimensional measure that answers this question. The Knudsen number (Kn) of a system is the ratio of the mean free path of the subject gas (γ) to a characteristic length scale of the flow (L, usually the channel hydraulic diameter). This relation can be found in Equation 6 [20].

$$Kn = \frac{\gamma}{L} \qquad \textbf{Equation 6}$$

The limiting ranges for how to model gas flow is divided into four areas, and is summarized in Table 3.

Table 3: Limiting values for Knudsen numbers and applicable treatment.

Knudsen Number	Analysis Treatment
$Kn < 10^{-3}$	Continuum assumption valid
$10^{-3} < Kn < 10^{-1}$	Continuum assumption with slip at boundary
$10^{-1} < Kn < 10$	Transitional Flow Regime
$10 < Kn$	Free Molecular (Rarified) Flow

The term "rarified" refers to a flow regime where the mean free path of the gas molecules (the average distance a molecule travels before striking another molecule) is on the same order of size as the flow geometry itself (i.e. channel size). During this type of gas flow, there are significant statistical fluctuations in flow behavior (as it is largely determined by the molecular behavior of the test gas) that must be modeled using intensely numerical coding techniques such as Direct Simulation Monte Carlo (DSMC) or molecular dynamics (MD).

For fluids, there is an equivalent measure for when the liquid can no longer be treated as a free flowing continuum. The equation remains the same (as shown in Equation 6), only the mean free path term (γ) is replaced by δ, which is the lattice spacing of the molecules in the test fluid [7]. This lattice spacing term is represented by the following calculation:

$$\delta = \left(\frac{V_1}{N_A} \right)^{\frac{1}{3}} \qquad \textbf{Equation 7}$$

Where V_1 is the molar volume, and N_A is Avogadro's number. This quantity is equivalent to 0.3 nanometers for water. If this value for the equivalent "fluid mean free path" is substituted into Equation 6 for γ, the result gives Kn = 6E-6 for a 50 micrometer hydraulic diameter, and Kn =

3E-4 for a 1 micrometer hydraulic diameter, which are both well within Kn < 10^{-3} continuum assumption. Using these measures, the smallest size channel size that can be used before entering the modified slip boundary conditions for continuum fluid flow is 3 nanometers (this size is about 650 nanometers for air at STP due to greater spacing of gas molecules). This value is well below even the accepted range of microchannel sizes for the majority of research in microfluidics, suggesting that flow through microchannels above 3 nanometers in size should behave according to the theories provided by macroscale fluid mechanics.

Macroscale Fluid Mechanics for Internal Flow

After providing theoretical justification that flow at the microscale should be treated as a continuum and described adequately by macroscale fluid mechanics, it is appropriate to present what is accepted as the cornerstone of macroscale flow theory through these channel geometries. It is the ultimate goal of this work to unearth differences in pressure that result from straight duct frictional effects and abrupt changes in geometry, and as such it is fitting to begin the derivation from conventional, time-honored laws that have been gracing the pages of fluidic/thermodynamic literature for centuries.

Starting from first principles, the energy equation (first law of thermodynamics) is considered in its most basic form as applied to a control volume shown in Equation 8 with the relation for the integrated energy term shown in Equation 9.

$$Q - W_s - W_{shear} - W_{other} = \frac{d}{dt}\int e\cdot\rho\, dV + \int (e + \rho\cdot v)\cdot\rho\cdot V\, dA \qquad \textbf{Equation 8}$$

$$e = u + \frac{V^2}{2} + g\cdot z$$

Equation 9

Given that the fluid is incompressible, the flow is steady, all work exiting the system is zero (surface, shear, etc.), and there is a uniform internal energy and pressure distribution, the energy equation, when coupled with the kinetic energy coefficient (α, as shown in Equation 10), can be reduced to Bernoulli's equation (Equation 11).

$$\alpha = \frac{\int \rho \cdot V^3 \, dA}{m \cdot V^2} \qquad \textbf{Equation 10}$$

$$\left(\frac{p_1}{\rho} + \alpha_1 \cdot \frac{V_1^{\,2}}{2} + g \cdot z_1 \right) = \left(\frac{p_2}{\rho} + \alpha_2 \cdot \frac{V_2^{\,2}}{2} + g \cdot z_2 \right) + \sum H_{loss} \qquad \textbf{Equation 11}$$

The head loss term is the total energy loss per unit mass, and is comprised of the irreversible conversion of mechanical energy at the entrance of the channel to unwanted thermal energy, and loss of energy via heat transfer [6]. Loss terms often include frictional effects, changes in geometry, and surface roughness effects due to material properties.

There are two elements of head loss to consider in fluidics pressure calculations: major losses and minor losses. The major losses, which typically account for a majority of the energy loss in a given channel flow system, contain contributions due to frictional effects and surface roughness effects. Roughness calculations take into account the channel geometry, flow rate, surface quality, and are based on flow regime (laminar vs. turbulent). A tabulated summary of the accepted theoretical behavior of this friction factor and its turbulent experimental

counterparts as a function of Reynolds number can be found in Figure 6. This figure is called the Moody diagram and is widely used in modeling flow behavior for both laminar and turbulent flow systems.

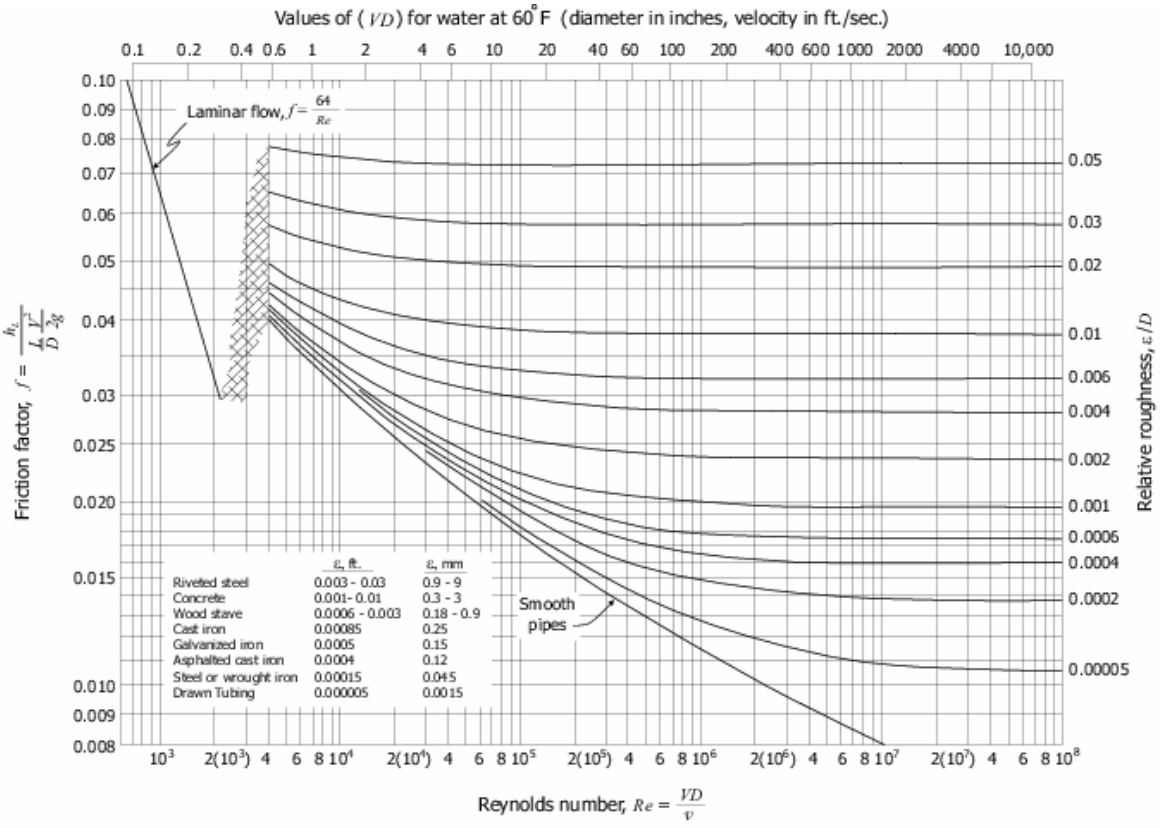

Figure 6: Moody chart - correlation of friction factor *f* and Reynolds number [5].

Given that this work suspects to consider flow in the laminar regime only (per later discussions in subsequent sections), Equation 12 is an appropriate value for the friction factor term *f*.

$$f = \frac{64}{Re} \cdot \left[\frac{1}{\frac{2}{3} + \frac{11}{24} \cdot \left(\frac{b}{h}\right) \cdot \left(2 - \frac{b}{h}\right)} \right] \qquad \textbf{Equation 12}$$

Equation 12 is a modified form of Equation 2 which takes into account that the cross sectional area of the flow will be rectangular (b is the channel base, h is the channel height), where Equation 2 is used for circular ducts. This yields the following expression for the major head loss term derived from energy balance, and with appropriate substitutions for fully developed pressure driven internal flow.

$$H_{loss.major} = \rho \cdot f \cdot \frac{L}{D_h} \cdot \frac{V^2}{2} \qquad \textbf{Equation 13}$$

Now that major losses have been accounted for, minor losses must be considered. For this work, abrupt changes in area (sudden expansions and contractions) are the only minor losses that the flow will be subjected to, though other traditional minor losses that are frequently considered when designing flow systems are sweeping/miter bends, flow inlet/exit phenomena, and other size transition geometries (nozzles and diffusers). All of these minor losses must be taken into account when determining total head loss (and summed with the major losses). Usually, the contribution to the final head loss from these minor losses account for less than 10% of the total head loss when there are very few minor loss terms, or if the liquid first must travel steadily over some undisturbed distance (thus experiencing major losses). The minor losses are nearly always represented in the following manner:

$$H_{loss.minor} = K \cdot \frac{V^2}{2}$$ **Equation 14**

Where K is a loss coefficient that must be determined for the given minor loss configuration. For sudden expansions and contractions in flow geometry, V. L. Streeter [21] provides correlations for these K values that are used by most foundational fluid mechanics textbooks today. Streeter determined that a sudden expansion loss coefficient K_e is dependent on the area ratio of the two channel sizes, and follows the relation:

$$K_e = (1 - AR)^2$$ **Equation 15**

For the sudden contraction loss coefficient K_c, Streeter conducted experiments and compiled data to graphically represent the numerical values of the loss coefficients (K) as a function of the area ratio of the channel, as no closed form analytical solution could be obtained. This is due to the vena-contracta effect, or narrowing of the flow below the channel walls after passing through the contraction feature, and is still not well understood enough for these contraction coefficient values to be calculated analytically as with the expansion coefficient values. A summary of these minor coefficient values (for both expansion and contraction) can be found in Figure 7.

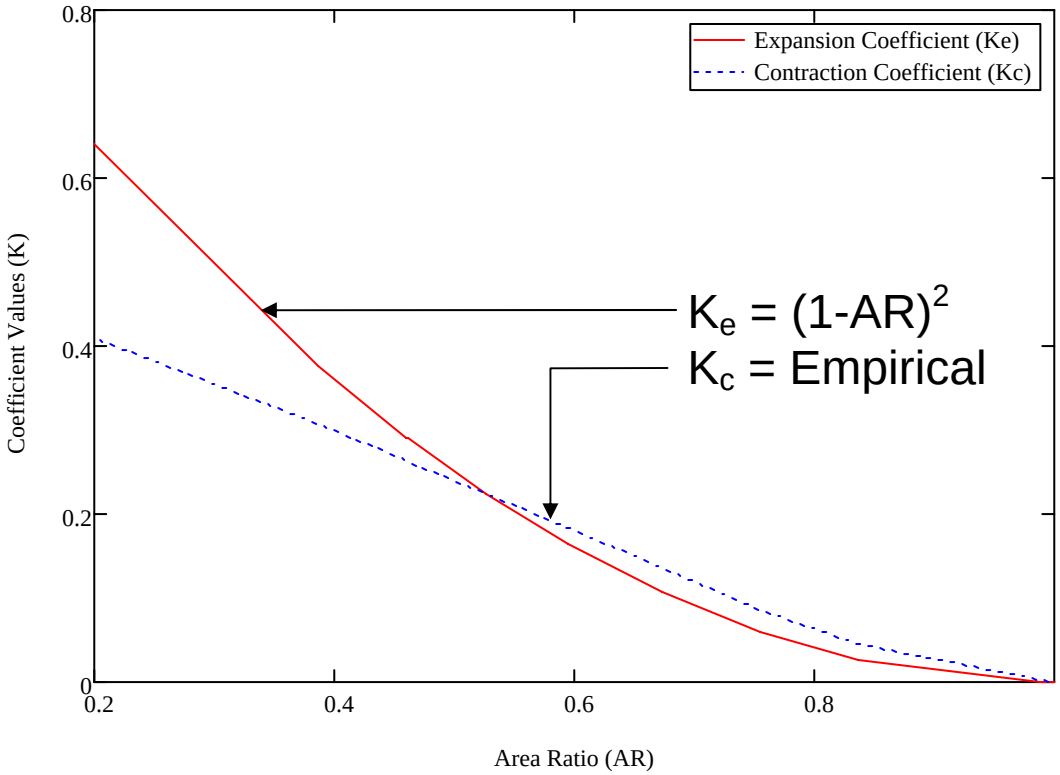

Figure 7: Tabulation of expanding/contracting loss coefficients as a function of area ratio.

It should be noted that the velocity used for these minor loss calculations is always the average velocity in the smaller channel size. Having these two coefficients to describe minor head losses will be extremely useful in filling in Bernoulli's equation (Equation 11) with appropriate head losses.

In simplifying these equations further, thereby making them more suitable for this work's flow system, flow through the channel may be considered to be unaffected by gravity in the streamwise direction, and the kinetic energy coefficients can be assumed to provide negligible impact to the kinetic energy terms of the equation. Equation 16 represents the resulting equation having taken these assumptions, and is shown incorporating the major and minor loss values.

$$\left(\frac{p_1}{\rho}+\frac{V_1^{\,2}}{2}\right)=\left(\frac{p_2}{\rho}+\frac{V_2^{\,2}}{2}\right)+\left(\rho\cdot f\cdot\frac{L}{D_h}\cdot\frac{V^2}{2}\right)+\left(K_{e.or.c}\cdot\frac{V^2}{2}\right) \qquad \textbf{Equation 16}$$

Now that a general overview of the fundamental analysis techniques that will be used throughout this work have been provided, the following sub-sections will continue to depict the detailed journey of the material selection, microchannel design, experimental set-up, and test philosophy of this work's methodology.

Microchannel Material Selection

The material used to fabricate the microchannel test section in this work went through multiple iterations. Many considerations such as surface properties, material/manufacturing costs, and procurement time all had to be evaluated before a material was finally chosen. A polymer fabricated via soft lithographic techniques called poly(dimethylsiloxane), or PDMS, was decided upon because it provided the optimal combination of all these categories, and brings with it many documented uses in microchannel research (specifically in biomedical applications such as capillary electrophoresis) [22].

The fabrication process begins with a master sample of the layout design using a CAD program. The sample is generated using high resolution ($\geq$ 20,000 DPI) printing on a transparency (i.e. Mylar), reflecting the "true size" of the design geometry. The transparency is then brought into a 10k clean room and utilized as a mask to create a positive relief of the channels via photolithography, where photoresist is employed as the material with which to create these "male" versions of the channels on a silicon wafer. This silicon wafer with the array

of microchannel shaped phtoresist protrusions is considered the master mold. Liquid PDMS is then poured over the male mold master, cured using the necessary temperature exposure requirements, then peeled off the wafer to produce the actual microchannels troughs. Another blank piece of PDMS that was cured on a blank piece of silicon is then bonded to the original piece of PDMS with the microchannels to "sandwich seal" the channels by exposing both surfaces of PDMS to oxygen plasma for 1 minute. This oxygen plasma bonding procedure produces an irreversible seal that is said to be stronger than the bulk PDMS material itself, and can also be used to bond PDMS irreversibly to a plethora of other materials such as glass, silicon, silicon oxide, silicon nitride, quartz, polyethylene, and glassy carbon [1]. The resulting irreversible bond between these two slabs of PDMS has been verified to withstand internal pressures up to 5 bars [7].

There are of course numerous advantages, as well as a few disadvantages, to using PDMS as the channel material. One is that the material is an elastomer, meaning it is rubber-like, elastic, and pliable. This is a positive characteristic of the test section material because there aren't too many worries of damaging the material if it is dropped or mishandled accidentally, and any effects used to induce flow or take pressure measurements where piercing is involved will be adequately sealed by the PDMS after piercing occurs. If a more rigid material were used, sealing around the pressure ports and infusion/removal ports would be troublesome. Later sections describe how this "elastic advantage" was used for sealing around all interfaces between test equipment and the microchannel. One disadvantage to the elastomeric material properties of PDMS, especially given that the geometric sizes are on the order of micrometers, is that a channel could be easily collapsed by any excessive (or unknown) force or deflection induced on the material.

Another advantage to using PDMS is how inexpensive it is to fabricate the flow geometry. Given the process outlined above, a reusable silicon master can be fabricated for well under $100 in material costs after high-resolution printing and photolithography. This is significantly cheaper than the extensive time and money spent attempting to machine the channel geometries into a rigid piece of material such as silicone, glass, or any metallic substance, where costs can approach the $1500 range. After the silicon master was created, it could then be reused to make multiple copies of additional PDMS slabs containing the microchannels at less than ½ day per copy.

Impact of material selection on flow properties were of utmost importance, since all aspects of the experiments had to be well known and controlled due to the unknown and controversial nature of microchannel research. The channel shape as a result of fabrication and PDMS surface quality were two material characteristics that proved to be of significant criticality. The electronic CAD drawing (and subsequent high-resolution transparency printout) provided a two dimensional footprint for exposure of the photoresist in the photolithographic fabrication process, where surface imperfections were directly related to the resolution of the printout. Thus, a higher resolution transparency printout provided a less “pixeled” surface in the resulting PDMS microchannel, as shown in Figure 8.

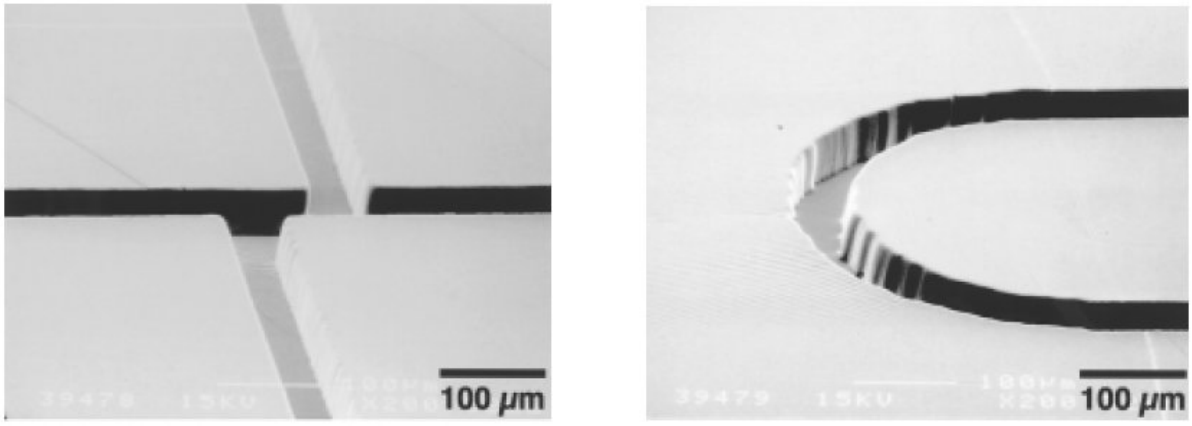

Figure 8: Smooth vs. rough channel quality as a result of differing transparency resolution [1].

The transparency printout supplied an outline of the channel array on the silicon wafer master, where the channel depth (or protrusion height) was controlled by the amount of exposure to the photoresist through the mask. For ease of construction, a constant height of 100 micrometers was chosen for every geometric shape on the array. This created a rectangular test section where cross sections and fluidic calculations had to be considered using hydraulic diameters instead of circular pipe diameters.

Another chemical quality of PDMS is that the material surface itself is naturally hydrophobic, or resistive to wetting. This creates an environment opposed to complete surface coverage or "wetting" by the flow medium (water in this case), and causes adverse effects in laminar, steady, fully developed flow. When the flow medium is resisted by the surface itself, changes in already high surface tension create unwanted slip effects (and support the formation of detested gas bubbles) not usually experienced during laminar flow, the effects of which can be drastic on calculated flow parameters in such small geometries. This adverse material property is prevented though through the conformal oxygen plasma process used to bond the two PDMS slabs together (one blank, and one with microchannel cavities). The oxidized surface of bonded

PDMS pieces develops a hydrophilic layer in contact with the flow medium, creating an easily wetted channel material that supports flow properties desired in the laminar regime. There are concerns with the durability of this hydrophilic layer however, in that research has indicated diversion from hydrophilic behavior with respect to the fluid contact angle when hydrophilic surfaces are left open to atmosphere for periods longer than 15 minutes. A well behaved hydrophilic fluid contact angle is acute (or less than 90 degrees), where a hydrophobic contact angle is obtuse (or greater than 90 degrees) [20]. Morra et al. [23] indicated that when oxidized PDMS was exposed to atmosphere for 15 minutes, the contact angle changed from 30 to 79 degrees. After 45 minutes of exposure to atmospheric conditions, the angle became 93 degrees. The native contact angle of non-oxidized hydrophobic PDMS is 108 degrees. With this in mind, great care was taken not to expose the oxidized PDMS to atmosphere for great lengths of time.

Microchannel Design

The design chosen for the microchannel layout combines usability, practicality, and efficiency into a single 4" diameter piece of sandwiched PDMS. Since the focus of this work is to measure and correlate the pressure drop experienced over a sudden change in geometry (due to an expansion or contraction), a complete array of area ratios was considered ranging from 0.1 to 1.0. Not only was it necessary to ensure that an adequate sample of all the possible area ratios were accounted for, but also that repeated configurations of the same area ratio were at hand to ensure reproduction of the pressure drops measured/calculated for a single area ratio. Area ratios were considered in increments of 0.1, starting from 0.1 and ending with 1.0 (straight channel with no sudden changes in geometry). Also, an area ratio of 0.276 was placed in the series for

comparison to the work of Abdelall et al. in their study of single phase flow through sudden expansions and contractions in flow geometry.

The larger channel size was designed to remain at 100 micrometers, and an appropriate calculation was performed to extrapolate the smaller channel size to ensure an accurate area ratio. The reasoning behind this size selection is multifaceted. The driving requirement however is to facilitate ease of governing equation simplifications and desired system stability at the laminar flow regime. It was therefore suitable to model the channel geometry around this requirement, performing rough order of magnitude calculations to ensure laminar flow is achieved, the macro scale limit of which is Re~2300 for internal pipe flow. For the various channel sizes mentioned above for each of the incremental area ratios, the Reynolds number range is between Re = 7 and Re = 130, which is well below the transitional limit of 2300, and gives approximately a 16X minimum buffer to account for any early transition to turbulence in the microscale regime (as proposed by other research groups). It is fitting then to foretell that no other flow regime will be encountered for the entirety of this work.

In addition to testing microchannels with abrupt area changes due to sudden expansions and sudden contractions, it was also of interest to test an array of straight ducts with no expansions or contractions of similar relative size. The purpose of this was to test the validity of straight duct macroscale fluid mechanics as applied to microchannels prior to examining flow behavior with minor loss considerations factored in. As such, each 4” piece of PDMS had half its surface area coated with simple straight ducts of various diameters (similar in relative size and length to the channels with expansions and contractions) to facilitate this analysis.

The final layout of the 4" diameter piece of PDMS contained 99 microchannels (49 straight duct channels, and 50 area ratio channels), with at least 4 copies of each channel to

achieve the desired repeatability of the system. Figure 9 illustrates the final layout of the microchannels, represented by a CAD drawing.

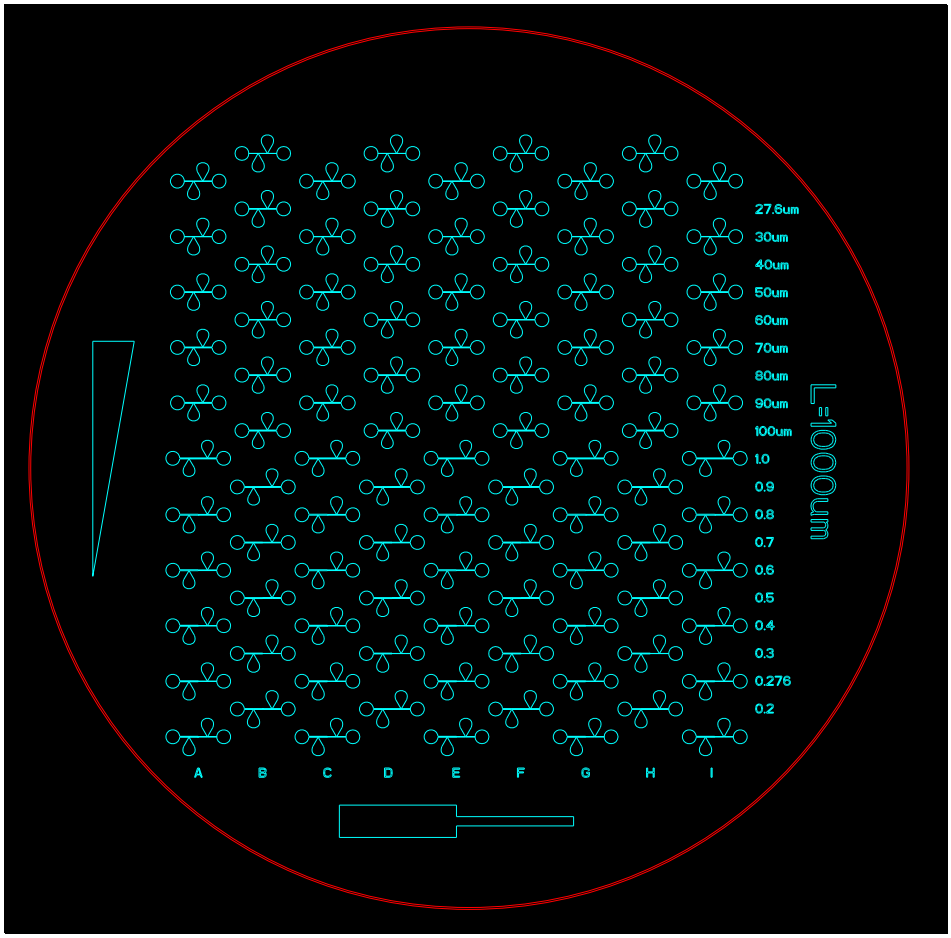

Figure 9: CAD of microchannel layout on a 4" diameter slab of PDMS.

It should be noted that certain additional drawing features were included around the perimeter of the channel array. These features were incorporated for tracking the numerous tests, and will be discussed later. Each channel contained four distinct ports: the entry port, exit port, and two pressure ports (on each side of the test section). Figure 10 outlines these ports for a straight

channel sample, and Figure 11 shows these ports for a channel with a sudden expansion/contraction feature. It should be noted that the channel in Figure 11 served as the test channel for both expansion as well as contraction testing, in that only the flow direction had to be reversed to create the opposite flow configuration. In Figure 11, the upper text in the port labels represents the configuration required to conduct a test in the sudden expansion configuration (flow travels from right to left), while reversing the flow direction (as well as the pressure ports) would be required to conduct a test in the sudden contraction configuration (flow travels from left to right), as indicated by the lower text in the port labels.

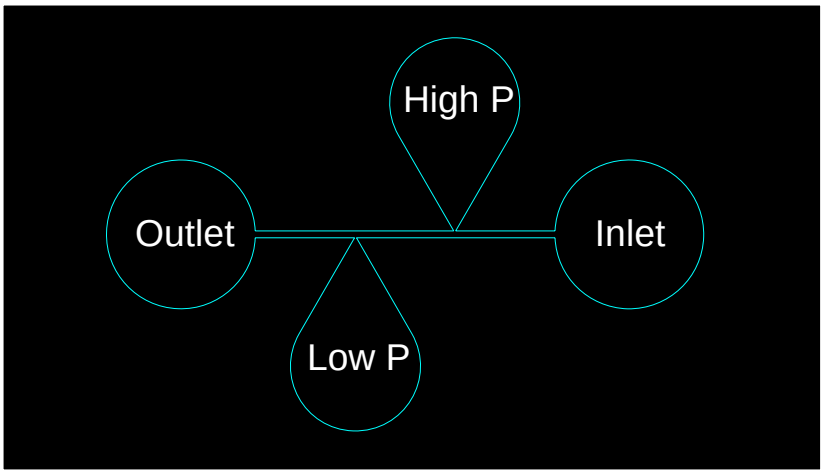

Figure 10: Single straight duct microchannel design.

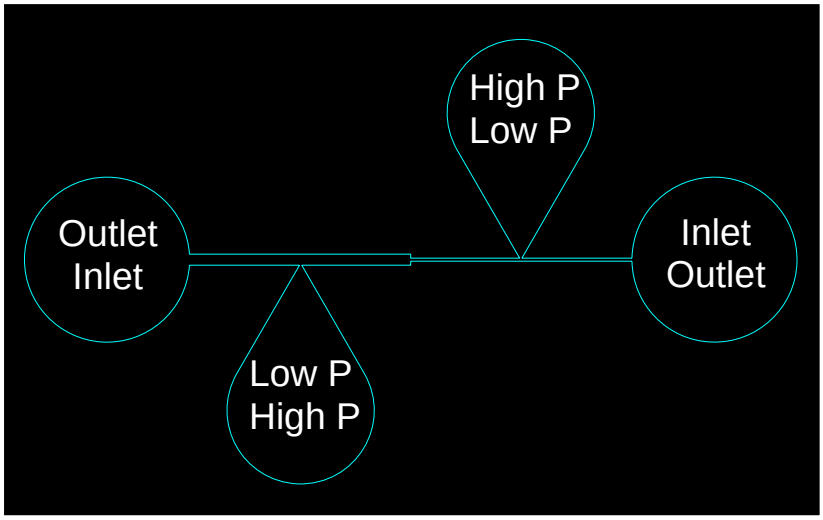

Figure 11: Single expansion/contraction microchannel design.

The philosophy behind this channel design revolved around eliminating as much unimportant measured data as possible. One of the major flaws in most microfluidics research today is the coarse measurement of global pressure losses between a point many stages before the test section of interest, and at the very end of the flow system when the test fluid is discharged to atmosphere. It is then required to "calculate out" everything but the test section of interest to the effort (i.e. microchannel geometry) in order to analyze the behavior of the flow with respect to the pressure drop and/or friction factor. This method seems attractive due to the reduction of complexity to the flow system (i.e. placement of pressure measurement equipment), often allowing for a single pressure measurement to be extrapolated very early in the flow network, and assuming discharge pressures to be that of atmospheric pressure. However, the "correction" calculations necessary often include the factoring out of infusion/discharge plumbing, various fittings, changes in material roughness, dissimilar materials that construct the channel walls, scaling parameters, etc. all of which could easily contain either some kind of

overlooked anomaly, or ranges of error that are too large to be of any practical use. With the channel design used in this work, pressure measurements can be taken immediately before and directly after a test section of uniform wall materials with no additional “corrections” to consider, and can be easily done with most commercially available differential pressure transducers. It should be noted that the flow medium must initially venture up in and fill these channel pressure ports in order for the pressure reading to accurately transmit from the channel to the pressure port, then, finally, to the pressure transducer, but these effects are considerably less pronounced and quickly accomplished than if the flow underwent several "regime changes" as with prior experiments in other works.

Since the pressure ports produce a measurement that is at a specific point in the flow field, but outside of the flow itself, any measurement device used for obtaining the pressure at these points would be measuring the static pressure. Thus, the rearrangement of Equation 16 provides a theoretical quantity for what this work will be measuring: differences in static pressure across the test section. This rearrangement will be referred to as Equation 17.

$$p_1 - p_2 = \frac{1}{2}\cdot\rho\cdot\left(V_2^2 - V_1^2\right) + \sum H_{loss.major} + \sum H_{loss.minor} \qquad \textbf{Equation 17}$$

The channel design also factored in the necessary entrance length to ensure the flow would reach a steady, uniform state prior to arriving at the first pressure port. A rough order of magnitude calculation was performed using the macroscale relation for entrance length

(Equation 18) to ensure the fluid had enough "settling distance" to iron out all the flow non-uniformities from entering the channel.

$$L_{ent} = 0.06 \cdot Re \cdot D_h \qquad \textbf{Equation 18}$$

For each of the channel sizes utilized, the estimated entrance length range was calculated to be between 30 and 500 micrometers. This gives a 1X minimum buffer for the channel designs outlined above (as the average distance between the entry ports and first pressure ports is 1000 micrometers), providing a more than adequate entrance length to ensure the flow is uniform in the test section.

Microchannel Fabrication

Once the microchannel test sections were designed, and the material selected, it was time to begin fabrication. First, on campus facilities and capabilities were recruited to fabricate the PDMS microchannels via the soft lithographic reverse casting process described above and found in [1, 7, 20, 22], as they were readily available and incurred little or no cost to this effort. Seeing as this micro fabrication process for creating channels of such small size is still under intense research and development as a field in and of itself, microchannels made from these resources produced relatively poor test sections. These channels contained extremely rough flow surfaces, and "muffin-tops," an undesirable phenomenon where the liquid PDMS material does not penetrate the area around sharp corners of the cured photoresist adequately, but rather rounds out these corners. "Muffin-topping" causes the channel cross-sectional area to be very difficult

to measure, as there is now complex curvature from which to calculate geometric flow parameters as shown in Figure 12 (image captured using a digital microscope).

Figure 12: "Muffin-topping" of channel cross section.

In addition to "muffin-topping" the channel cross-sections, the rounding out of sharp corners causes the abrupt expansion and contraction features to look more like nozzle and diffuser features. These features are critical to this work's analysis, and any defects contained in them would be detrimental to the results measured without severe corrections in the analyses. A sample image from these channels can be found in Figure 13.

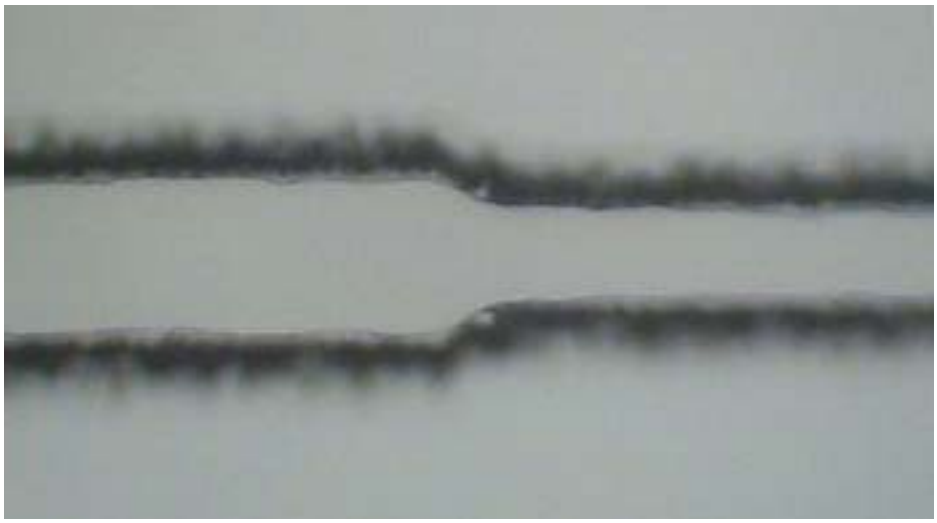

Figure 13: Rounding-out of expansion and contraction features.

With the abundance of these unwanted effects, efforts were refocused to procuring the channels from an outfit that was a bit more specialized in such fabrication techniques.

The Stanford University Microfluidics Foundry ended up being the outfit of choice due to design capabilities and lead time benefits, and supplied all the microchannels tested in this work. The CAD drawing shown in Figure 9 was supplied electronically and two copies of 4" PDMS "chips" were delivered containing the array of microchannels shown. The silicon master (containing the cured photoresist) from which the channels were molded was also delivered should additional copies ever want to be made. Figure 14 shows the silicone master and Figure 15 shows the resulting chip of microchannels cast from this wafer.

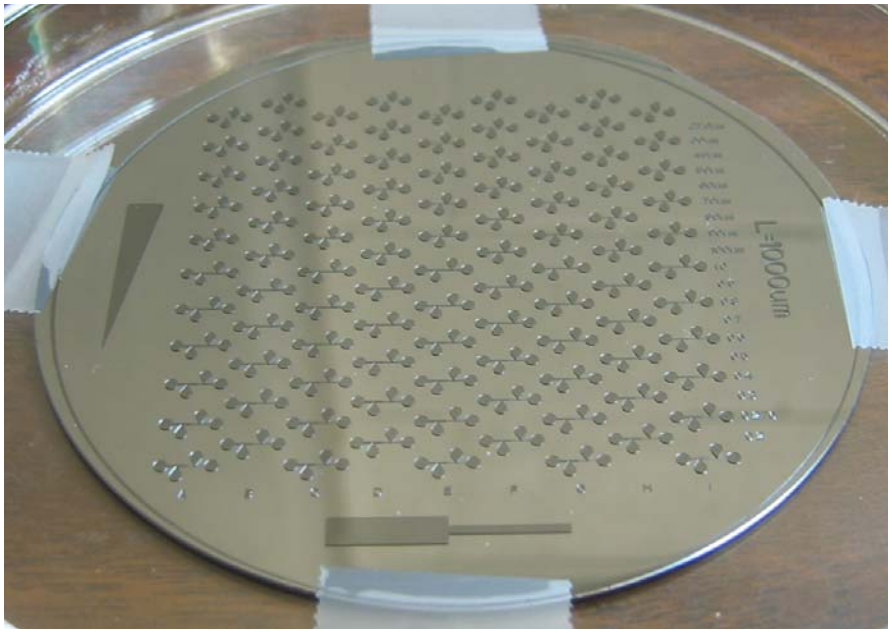

Figure 14: Silicone master.

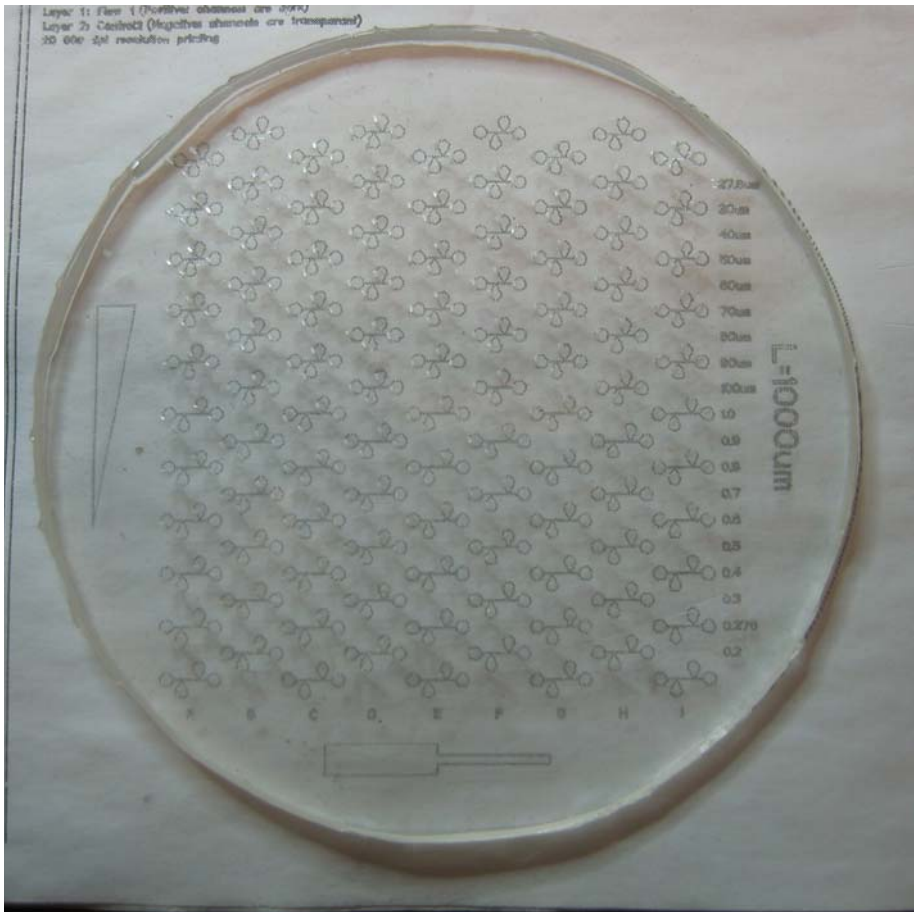

Figure 15: Microchannel chip cast from silicone master.

As mentioned before, the fabrication process for manufacturing these channels is still under much development itself, but the supplier outlined their limitations very clearly so that channels could be designed with adequate parameter tolerances (channel size, spacing, aspect ratios, etc.) to withstand these inconsistencies and still be adequate for testing. It should also be noted that reference and alignment features were cast directly into the molded PDMS so that human error would be minimized during testing, a looming terror when trying to keep track of nearly 200 unique channels. One of these features was an oversized area ratio diagram marking the general configuration (and direction) of the expansion/contraction geometry (as seen at the

very bottom of the chip). This represented the direction of area reduction for all the channels containing this feature, as they were often hard to see with the naked eye. The horizontal lines that created both the large and small rectangular shapes of this feature were 1" in length, so that this feature served the dual purpose of providing a directional as well as a relative size reference to the chip. Another size reference feature was a nonsymmetrical triangle of prescribed lengths (triangle at left). The length of the vertical side was 1". There were also locating features outlining a grid, where each one of the channels in the array would occupy one of the unique 99 cells in this grid. The columns were identified by the letters A through G (molded below the array), and the rows were identified by the most obvious feature size of the channels (and molded to the right of the array). The straight channels (top half) were identified by their channel width, and the expansion/contraction channels (bottom half) were identified by their area ratios. Each row contained 4 to 5 copies of each channel, repeated over the respective columns. For each row, the channels were repeated with a blank cell between each copy in the row to keep adequate spacing between the channels. For instance, the "30μm" row (fourth row from the top) would contain five 30μm straight duct channels placed in columns A, C, E, G, and I. The next row (which contained four 40μm straight duct channels) had its channels placed in columns B, D, F, and H. This staggered spacing allowed the maximum number of microchannels (99) to be placed on a single ship without causing leaks or breakages during testing due to inadequate spacing. All channels were guaranteed to withstand pressures of up to 20 psi by the supplier given the channels were adequately spaced.

Since there were many variables during the fabrication process that could affect the resulting channel shape/size, it was imperative that each of the channel dimensions be measured

as precisely and thoroughly as possible to ensure an accurate macroscale theoretical prediction of the flow would be modeled. It was also desired to verify that the channel interior surfaces and stepped area features be of a higher quality than previous channels made with on campus resources. The digital microscope was once again employed to take clear and accurate images of the channels (another benefit to using a transparent material to fabricate the channels). Figures below give a composite image of multiple pictures (at 4x magnification) pieced together to form an entire straight channel (Figure 16) and an entire channel with an area reduction (Figure 17). Figure 18 gives a 10x close-up of the straight channel surface. Figure 19 gives a 10x close-up of one of the area ratio features.

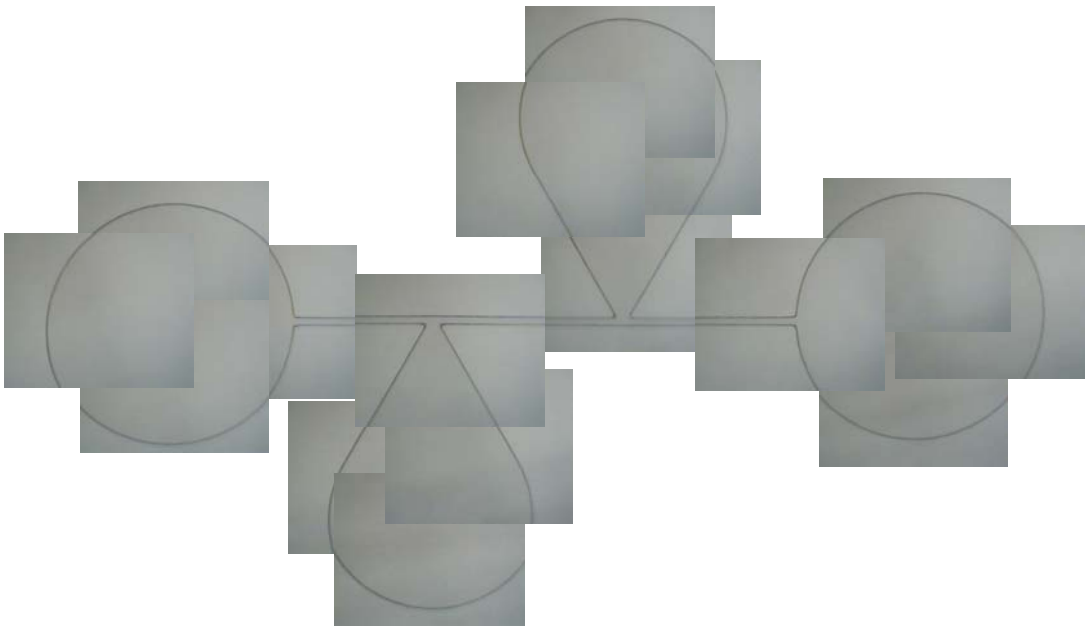

Figure 16: Composite image of an entire straight channel.

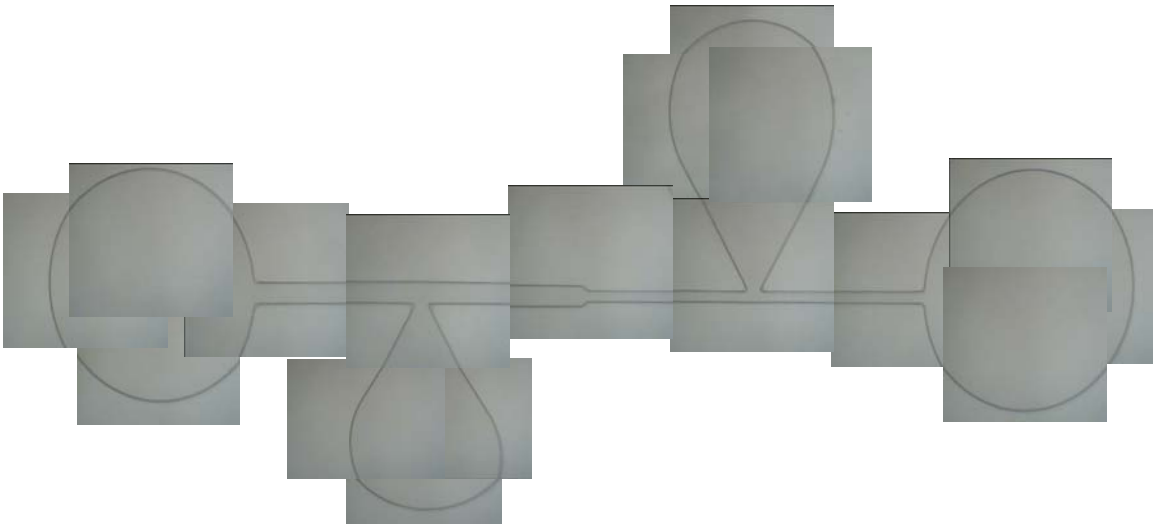

Figure 17: Composite image of an entire channel with an area reduction.

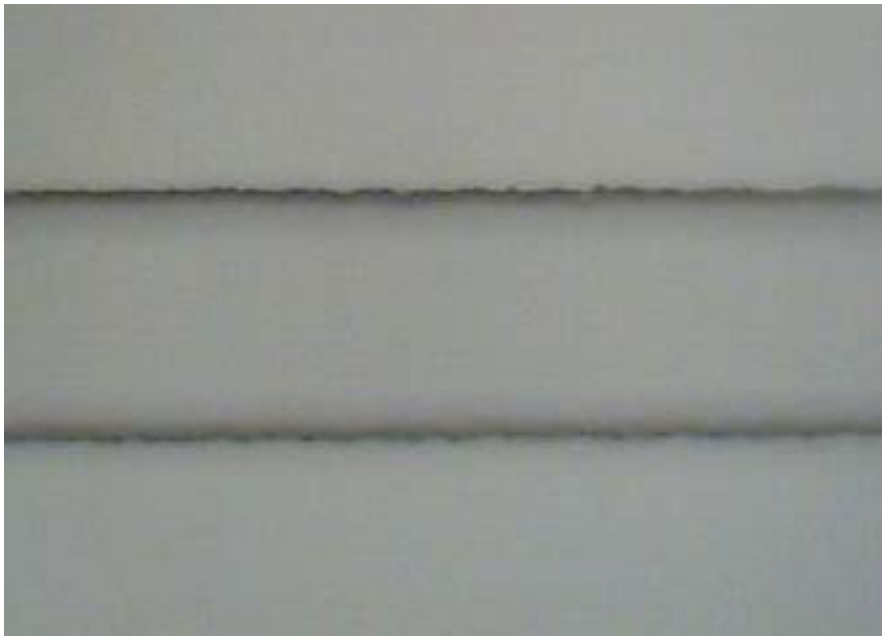

Figure 18: Surface of a straight duct channel at 10x magnification.

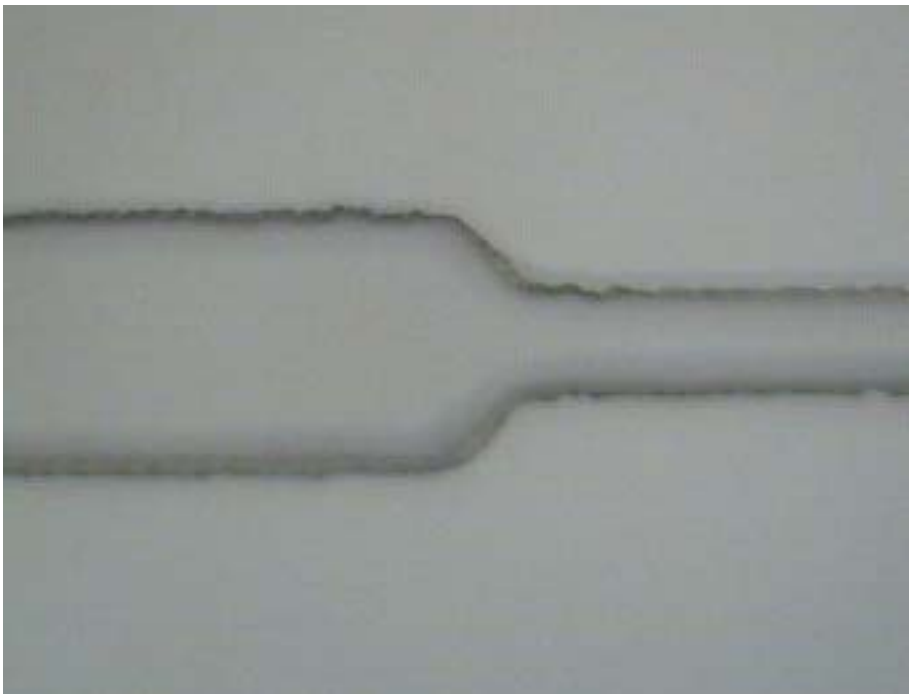

Figure 19: Area reduction at 10x magnification.

It can be concluded from the figures that the quality of channels supplied by the Stanford Microfluidics Foundry far surpassed that of the quality of channels supplied by other resources. There were still some anomalies to note that would require some adjustments to the macroscale flow models, however. One was that the same rounding-out of corners was still present in the expansion/contraction area reduction features, though not nearly as drastic or extreme as the channels fabricated and shown earlier, and limiting their more drastic form to smaller area ratios.

The most severe of these anomalies was that the actual channel dimensions came out larger than originally designed due to expansion/relief adjustments induced (and required) during the soft lithography manufacturing process. This caution was issued by the supplier, so its occurrence was not detrimental to the experiments. Channel width, for example, came out be consistently 30 micrometers above the design dimensions submitted in the original CAD

drawing. This meant that all theoretical predictions had to be corrected to calculate using actual channel dimensions, as relations that used these geometric quantities (such as Reynolds number, friction factors, etc.) would be prone to massive errors and produce inaccurate results. Therefore, it was decided to measure all channel widths and lengths such that the inaccuracies due to variability in the channel dimensions would be drastically reduced, and nearly eliminated from the theoretical calculations. To facilitate these measurements, a digital microscope was once again employed. Digital images were captured and channels were measured in screen pixel units using a computer graphics manipulation program. A calibrated micrometer scale with both 10 and 1 micrometer graduations, shown in Figure 20, was used to convert pixel measurements from digital images to micrometers after a simple calibration at 4x and 10x magnifications.

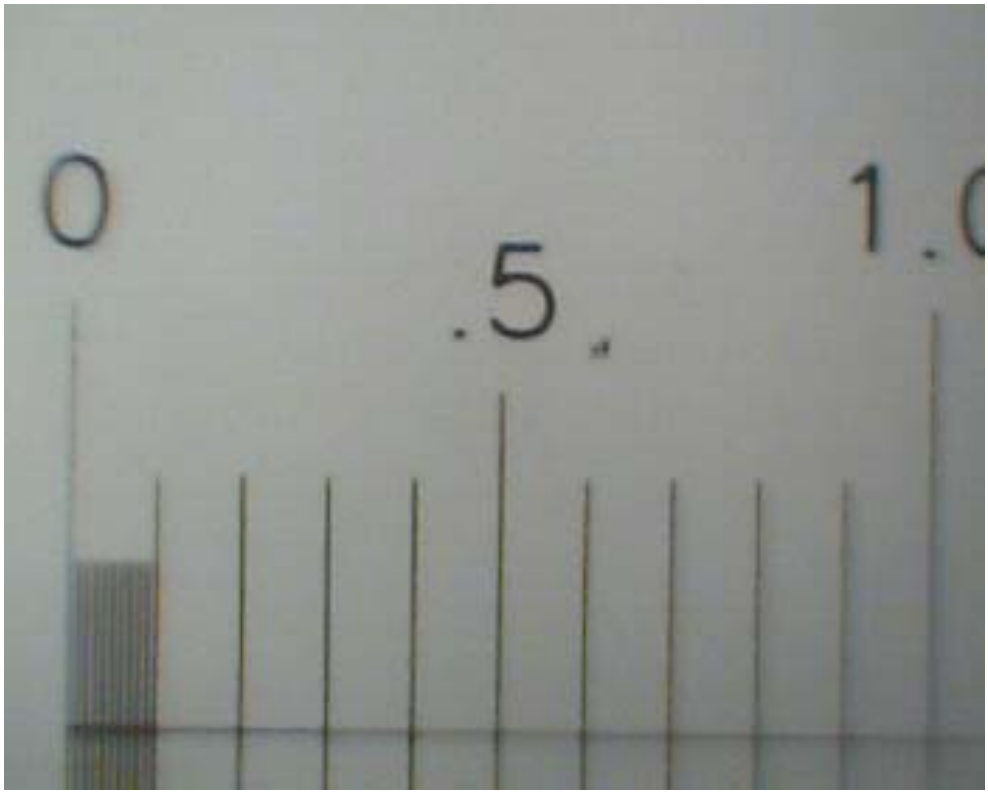

Figure 20: Micrometer scale used to calibrate digital microscope.

Given the massive variation in length and width, it was feared that the channel depth (height) would also have the same dimensional inconsistency. Therefore, a sample of channels were sliced perpendicular to the cross-section of the flow using a sharp blade, and measured using the same methods employed to measure lengths and widths (after testing, of course, due to the destructive nature of this measurement). The channel heights measured were found to be much more consistent in their dimensions than the other channel dimensions (consistently around 104 micrometers). Figure 21 depicts one of the these sample channel cross sections. There was little to no "muffin-topping" to be seen on any of the channels viewed in cross-section.

Figure 21: Cross-sectional slice of a sample microchannel.

One limiting characteristic of the supplier in general that affected this work was the aspect ratio requirements of their manufacturing process. This characteristic caused some of the perimeter channel geometry (and subsequent height dimensions) to be more varied because their aspect ratios were close to or in violation of the fabrication limits of the fabrication process. The maximum Y:X ratio (Y = channel height, X = channel width) was 5:1, meaning for a constant 104 micrometer height, the smallest possible designed channel width must be above 20 micrometers. At this limit, manufacturing limitations begin to severely warp the microchannels, and results extrapolated from testing become extremely unreliable (unless great care is taken to map the channel exactly as it was produced). The design of these microchannel configurations intentionally included channels with dimensions that violated this design rule, more as an experiment of how the manufacturing process would hold up. The channels in these size ranges, as warned, came out contorted, disfigured, and sometimes even collapsed. See Figure 22 for a sample of channels in this aspect ratio regime.

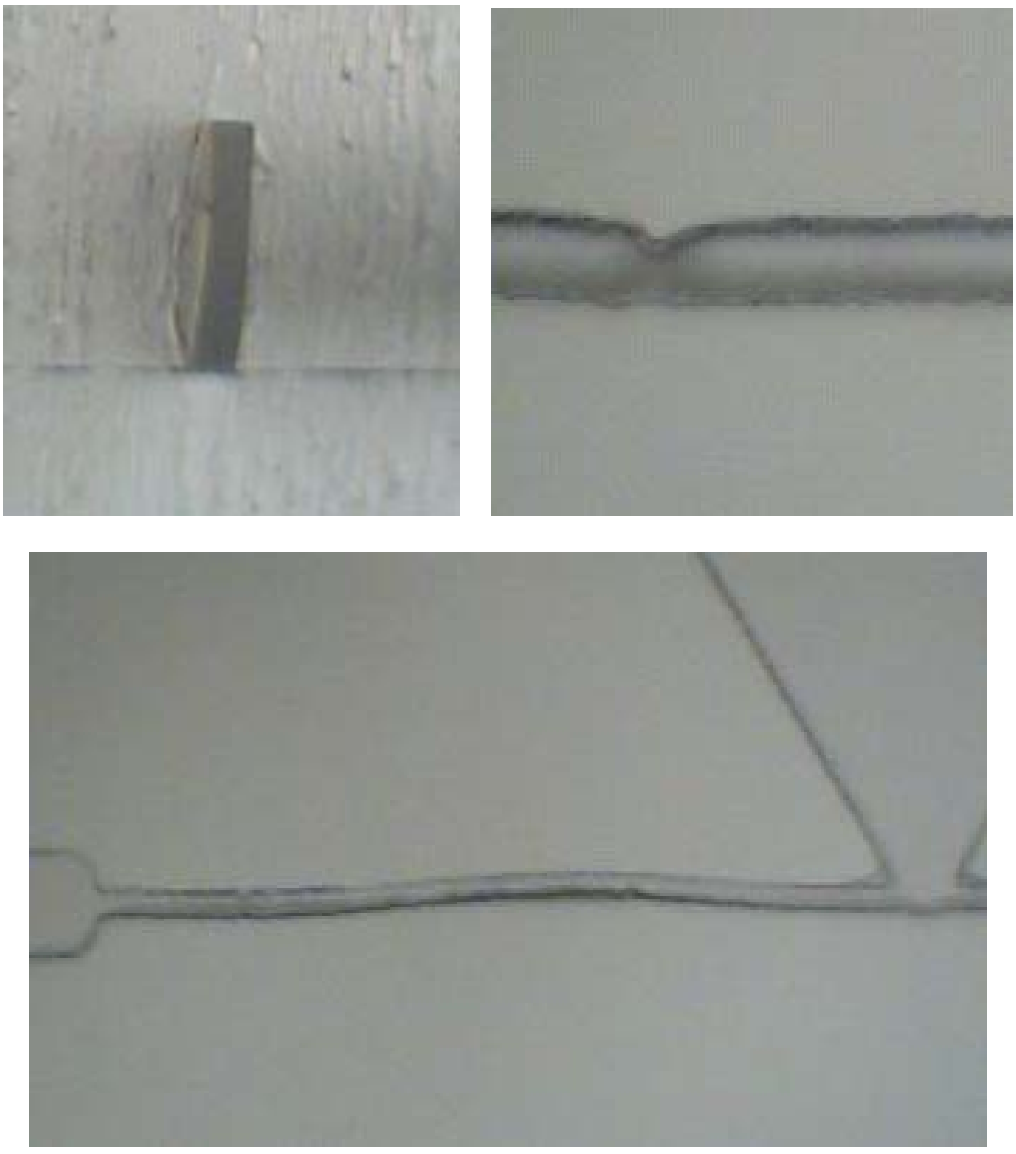

Figure 22: Images of channels that violate a 5:1 aspect ratio.

With all of these adverse manufacturing elements contributing to the final channel design, great care was taken to ensure each was considered as accurately as possible within the theoretical macroscale flow predictions. It should be noted that due to the necessary dimensional alterations as a result of the manufacturing process (up to a 30μm increase in length and width channel dimensions), the size range of subsequent testing was adjusted to include straight

channels of widths ranging from 50 micrometers to 130 micrometers, and area ratios ranging from 0.4 to 1.0, all with 104 micrometer heights.

Experimental Set-Up

As with any set-up, there are advantages and disadvantages to consider when evaluating and implementing a microfluidic system design. Advantages to the global pressure measurement systems aforementioned include their credibility of producing verifiable field data from prior works in microchannel research, and ease of assembly. Having been so widely used by other researchers and producing what appear to be reliable results, it is easy for one to duplicate the system while simply replacing the test section with the flow geometry specific to their focus. This also gives rise to the advantage of allowing the results of the two works to be compared while attributing little deviation to the experimental set-up itself, as this variable would be nearly unaltered for the two systems. Disadvantages include silencing the perpetuating argument that continuously improving prior work is the essence of applied research. Why settle for what has already been done (because it is readily available) when improvements can make the system, and thus results, more applicable, usable, and robust? Time and effort is saved, but contributions to the field are minimized. It is for this reason that the decision was made to utilize a new microfluidics testing system that made significant improvements on the system described above. The two major philosophical changes to the improved experimental set-up included the facilitation of direct pressure measurements via pressure ports designed directly into the microchannel itself, and the automated administration of flow into (and extraction from) the microchannel.

Set-Up Design and Equipment Selection

It was decided to employ the robust experimental set-up developed by Chase Hansel [19], as it was readily available and concurrently designed and developed with the efforts of this work in mind. Hansel, for his work, also designed test sections such that pressure measurements could be taken directly from ports stemming from the microchannels themselves, though test sections in that work focused on sweeping pipe bends over various angle and radii. While an overview of the equipment set-up and test process will be outlined here, the details of the selection methodology behind each of the individual components can be found in Hansel's work [19]. Figure 23 represents a schematic of the experimental set-up, and Table 4 gives the detailed product information for each component. Figure 24 is an actual photograph of the set-up labeled in the same way as Figure 23 (with additional non-numbered reference materials needed) whose information can be cross referenced using Table 4.

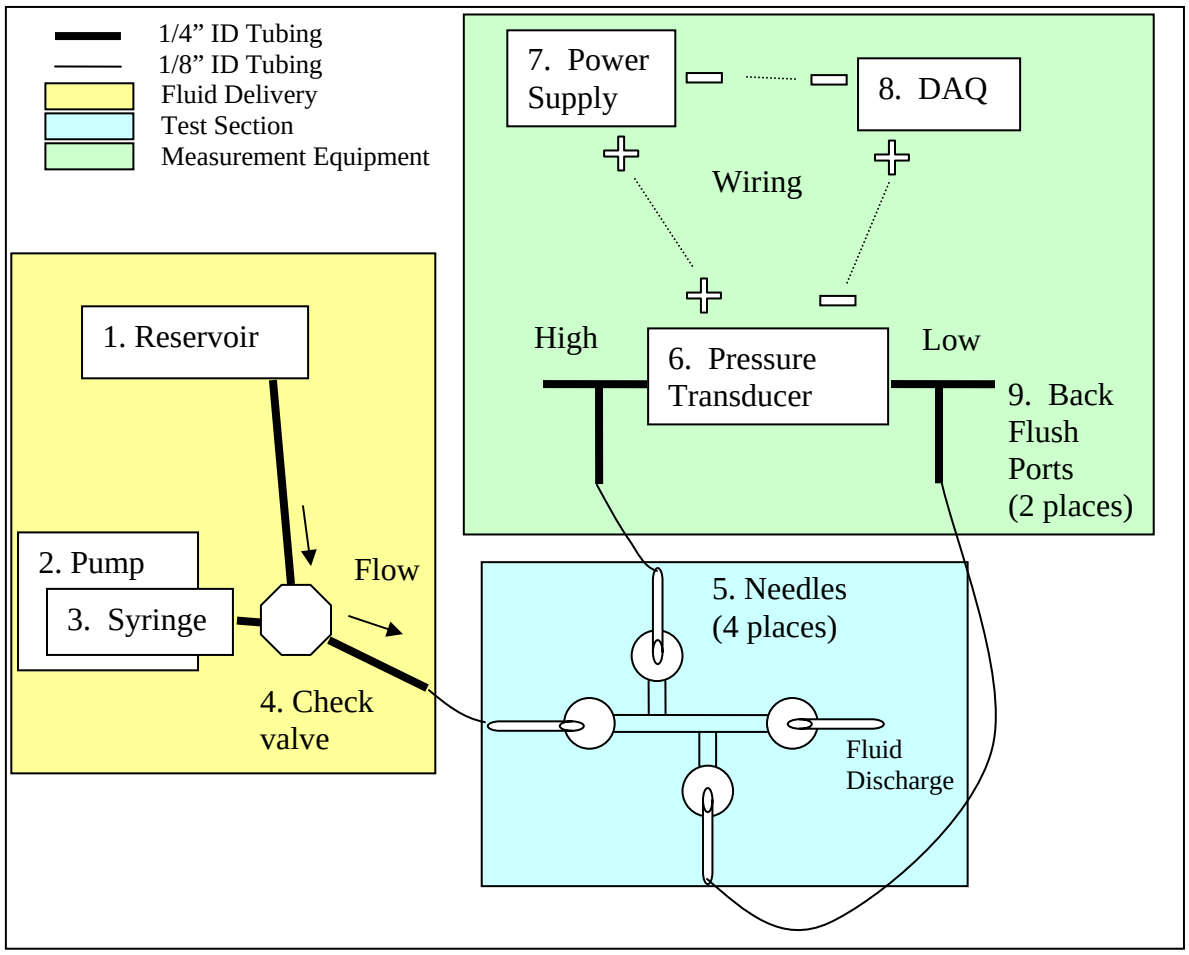

Figure 23: Experimental set-up schematic [19].

Table 4: Product information for each component [19].

Schematic Number	Name	Component Information
1	Reservoir	Covered tank for holding test fluid
2	Syringe Pump	NE-1000 Single Syringe Pump
3	Syringe	6cc Monoject with leur lock
4	Check Valve	One way check valve
5	Needles	McMASTER-CARR: 75165A757 (21 gauge)
6	Transducer	Omega: PX2300-2DI
7	Power Supply	Omega: PSS-D12B
8	DAQ	Omega: OM-CP-QUADVOLT
9	Back Flush Ports	Allows back flushing of pressure lines

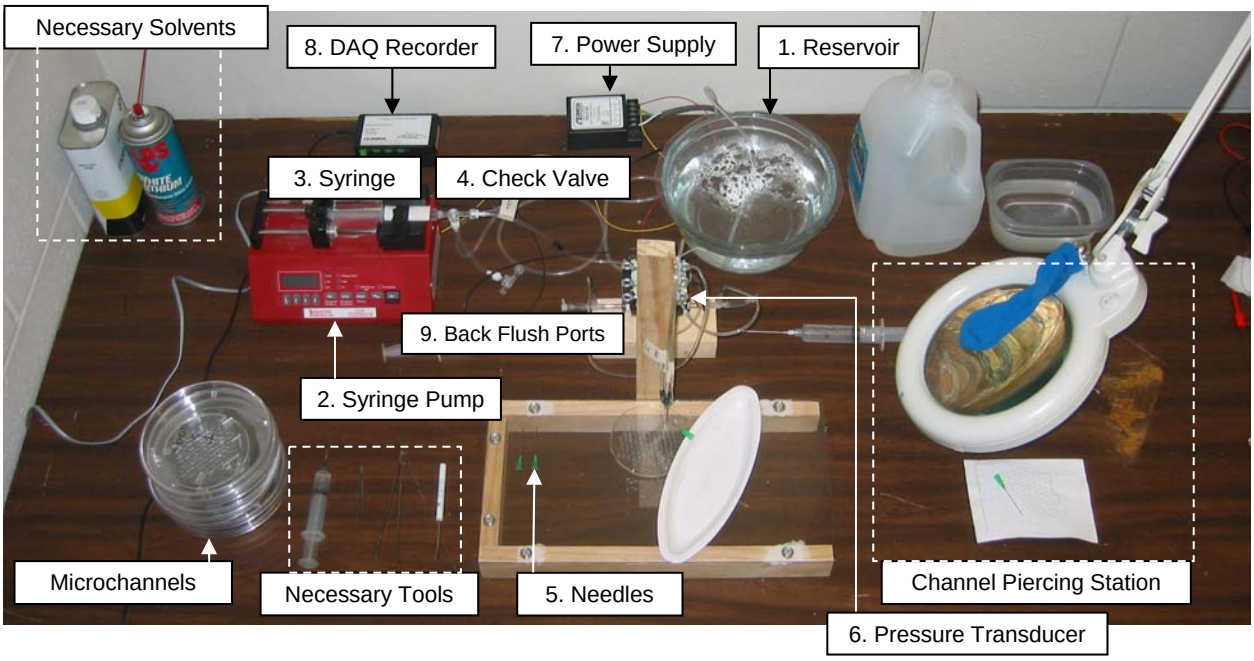

Figure 24: Photograph of experimental set-up.

The test liquid chosen was distilled water for its ease of procurement, handling, and already extensive (and applicable) use in the field of microfluidics. The NE-1000 syringe pump (schematic number 2) was chosen as the flow rate controller due to its highly precise (threaded shaft, worm gear) pumping capability, simple user interface, and additional time saving features. One of these features that were heavily used, the programming feature, allowed for the pump to run autonomously, testing multiple flow rates at different time intervals without any user interface necessary. This allowed lengthy tests to be administered without any supervision, thereby greatly increasing productivity. Another element of the set-up that made this

programming feature possible was the design and implementation of a test fluid storage reservoir (schematic number 1). In the pump's program, a "withdraw" command could be initiated to reverse the pumping direction and pull back the syringe plunger, however, the withdrawing of liquid back out of the channel test section was not the desired intent of this feature. A check valve (schematic number 4) was strategically placed at the junction in piping between the syringe, reservoir, and infusion line to the channel in order to block the reservoir tube during normal pumping operations (when fluid is pumped directly from the syringe into the microchannel), while blocking the infusion path to the microchannel during withdraw operations (allowing liquid to refill the syringe as its pulled from the reservoir). See Figure 25 for a picture of this configuration.

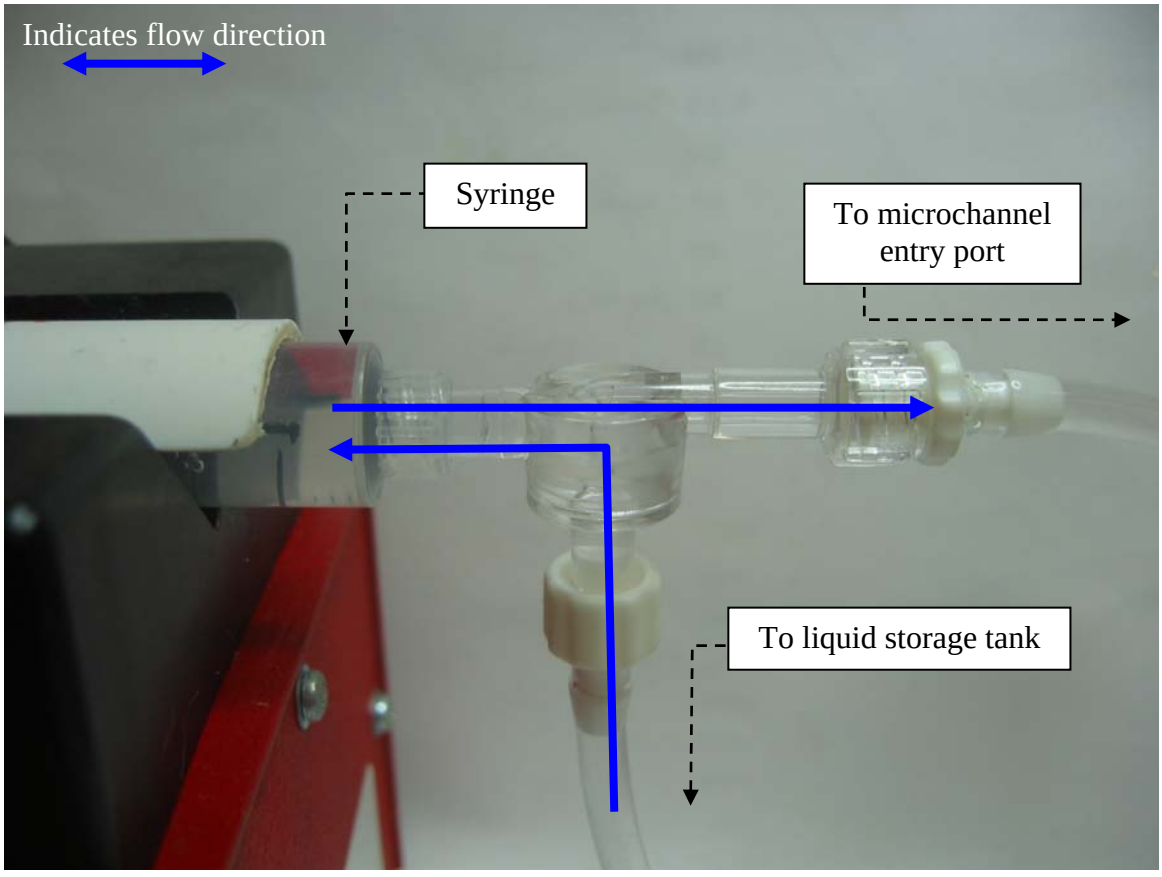

Figure 25: Check valve between syringe, fluid storage tank, and microchannel infusion tube.

The flow rates selected for testing were carefully chosen to ensure the flows throughout the entire duration of the tests were kept laminar. As mentioned before, the microchannels were designed to encounter only laminar flow in the range of Re = 7 to Re = 130, so the flow rates selected were based on this Reynolds number range. As the pump flow rates could only be set in units of micro/milliliters per hr/min, this put our pumping volumetric flow rates in the range of 50 to 500 microliters per minute, with increments in 50 microliters per minute. Therefore, a complete test would experience 10 different flow rates (and subsequently 10 different Reynolds numbers), for approximately 10-15 minutes in order to obtain enough steady state voltage/pressure loss data at each flow rate. After each of the flow rates, the withdraw function was called in the pump program to refill the syringe with water from the storage tank through the check valve. The entire duration for a single test that went through each of the required flow rates lasted about 2.5 hours. Table 5 outlines the programmed flow rates experienced by a single 100 micrometer wide channel with extrapolated Reynolds numbers.

Table 5: Sequence of flow rates for all tests, with extrapolated Re for 100μm straight channel.

Vol (μL/min)	50	100	150	200	250	300	350	400	450	500
Re	8.17	16.35	24.52	32.70	40.87	49.04	57.22	65.39	73.57	81.74

The transfer of fluid to and from the microchannel test section proved to be another major improvement to prior set-ups. This is both a function of the channel design, as well as the material selected for creation of the microchannel test sections (PDMS). The elastomeric

properties of the material allow for it to be deflected away from its free (molded) state, with an inherent need to return to this free state. Thus, any object that pierces the cured slab of this isotropic rubbery material will create an air-tight seal around the interface between the PDMS and the object itself, which was a critical aspect that allowed for this experimental set-up to be fruitful. Designing entry/exit ports for the flow medium, and pressure ports casted directly into the PDMS microchannel (set at the same depth as the channel itself), allowed for delicate penetration into the microchannel through the top layer of PDMS using 21 gauge needles (schematic number 5). These needles acted as the interface between the channel, and any piece of flow or measurement equipment in the test system. As seen form Figure 23, there are tubes connecting the inlet port to the check valve (and, as a result, the syringe pump), the outlet port to a discharge reservoir, and the high and low pressure ports to their representative counterparts on the pressure transducer, all of which pass through a 21 gauge needle piercing through the top layer of PDMS and forming an airtight/watertight seal. Before this test configuration is achieved though, a very delicate, technique governed procedure must be followed to ensure successful testing.

Test Procedure

The set-up procedure also very closely follows the methods outlined in Hansel's experiments, save for a few critical observations and adjustments unique to this work. The set-up process will be given for a single unique test (for a single microchannel), and assume that the syringe pump is programmed, all equipment needed to operate and record data (transducer connected to power supply and DAQ system, and DAQ software ready to record) is installed and

operational, and there is ample test liquid loaded in the storage reservoir. This process had to be repeated for every test, where additional periodic maintenance of the system occurred every 20 to 30 tests or so. These periodic maintenance items included lubricating the worm gear mechanism of the syringe pump, replacing the infusion syringe, flushing the bleed screws on the pressure transducer (through the pressure ports), and topping-off the test fluid reservoir that refills the syringe during withdraw steps in the pumping program. The procedure for setting up single a test (minus these periodic maintenance items) is as follows:

1. Save any acquired data from prior tests on the computer attached to the DAQ system.
2. Remove the needles from any prior test channels by carefully lifting the (qty. 4) 21 gauge needles directly upward out of the inlet port, exit port, and two pressure ports.
3. Place and align the clear PDMS chip over a 1-to-1 (true size) printout of the microchannel array using alignment marks/features on the chip (large triangle, scaled channel shape diagram, etc.). See Figure 26 for reference.

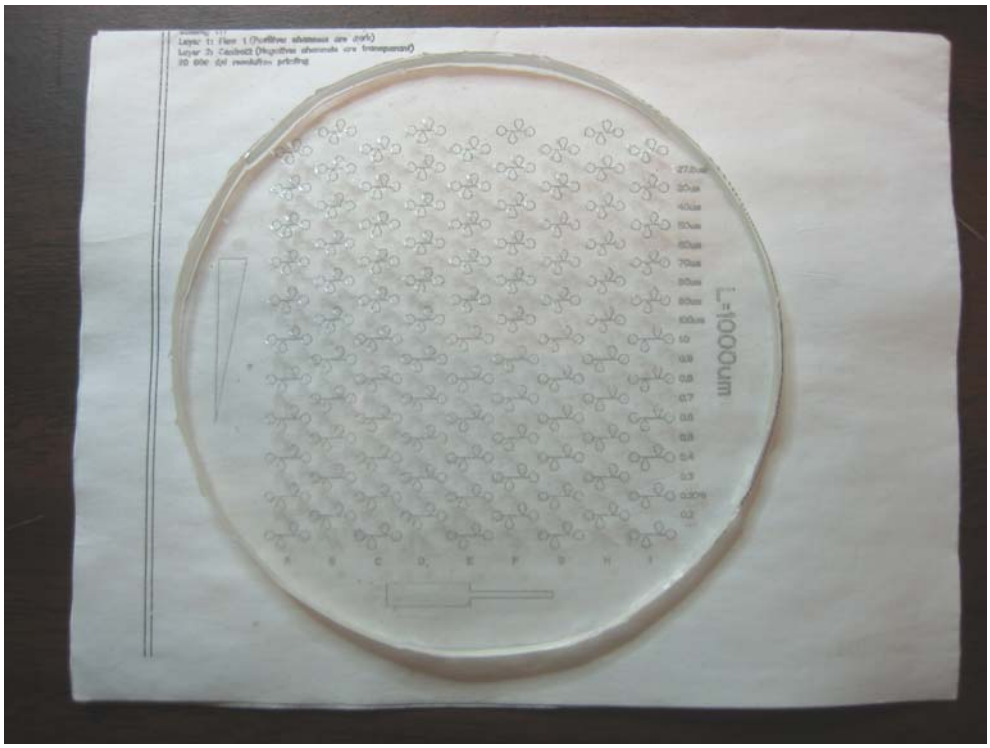

Figure 26: PDMS test chip aligned over 1-to-1 computer printout.

4. Using an unmodified 21 gauge needle (same type needle that is used for actual testing, only not connected to any tubing or ports) align the tip directly centered over the right most port using the 1-to-1 printout under the PDMS as a guide (see Figure 27).

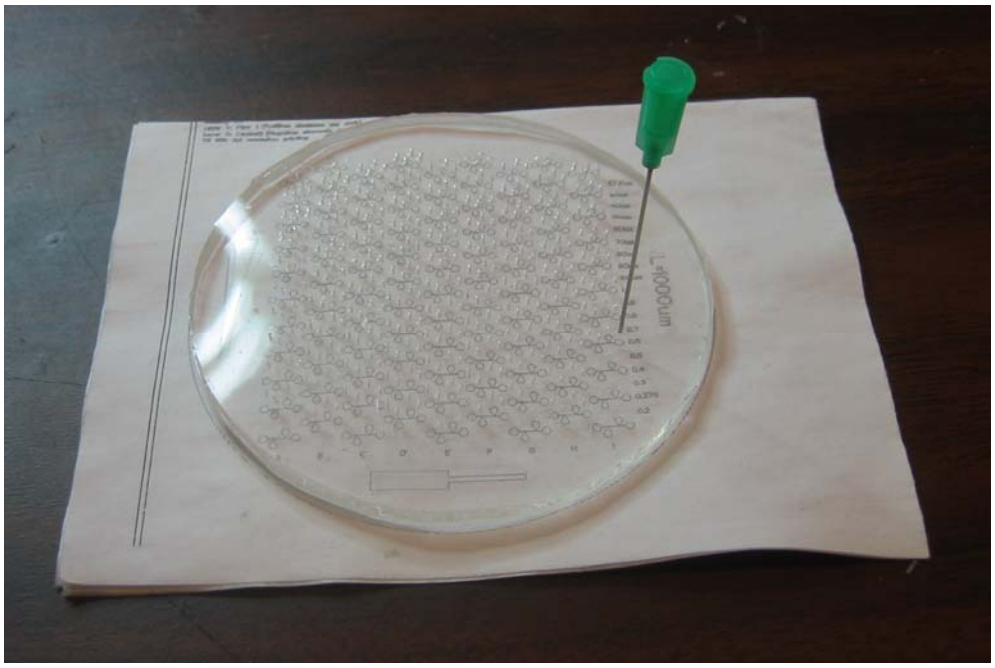

Figure 27: PDMS chip with needle inserted.

5. Delicately, but firmly, press directly downward without any twisting motion through the top layer of PDMS and stop just before breaking through to the microchannel.
6. The next few millimeters of piercing must be done *very* slowly to ensure the needle tip doesn't break through the top layer of PDMS too rapidly and press down vigorously on the channel floor, causing the two slabs of PDMS to delaminate. Press down slowly and stop immediately after breaking through the top layer of PDMS.
7. Choose a twisting direction (clockwise or counterclockwise), and keeping the needle as vertical as possible, twist slowly in the chosen direction and pull up lightly as if disengaging or unscrewing the needle from the PDMS. It should be noted that after a twisting direction is chosen, the opposite direction *should not* be used, as this may

"bore" an oversized hole in the PDMS. Violent extraction may also cause the two layers of PDMS to delaminate. Great care should be taken in this step.

8. If successful, a small cylindrical piece of PDMS should be sticking out of the needle tip once the needle is pulled completely out of the slab. Remove this piece from the tip and continue (no cleaning is required). If the small cylinder is not in the needle tip, it still remains in the PDMS slab. Do not attempt to reinsert the needle into this hole, as the cylindrical piece of PDMS will likely be pressed into the channel port making it virtually impossible to extract (see Figure 28). Using small tweezers is the next best option for extraction of this small piece.

Figure 28: PDMS cylinder lodged into port.

9. Continue with steps 3 through 8 for the remaining (qty. 3) ports. It is important to commence with testing within 10 minutes from the first pierce to prevent the hydrophilic coating provided by the oxygen-plasma treatment from becoming hydrophobic due to prolonged exposure to atmosphere.
10. Open a new file in the DAQ computer program, and start recording voltage information from the DAQ voltage recorder. The program will capture voltage information during all of the following steps. It will be evident in future steps that this is done to verify proper flushing of the pressure ports to be tested.
11. Set the PDMS slab in position on the test bench.
12. Insert the infusion port into the desired end of the microchannel test section by pressing directly downward. Stop the needle point approximately halfway down the top slab of PDMS so as not to block the channel port with the needle tip or risk delaminating the microchannel by deforming its base (as cautioned during the piercing step).
13. Set the pump to a flow rate that will register a reading (but not overexert) the pressure transducer and DAQ software, and begin pumping. Water will begin to fill the microchannel and discharge out of the high pressure port (and possibly the exit port).
14. When a decent sized pool of water collects over the high pressure port of the microchannel (see Figure 29), pause the syringe pump and open the high end of the pressure transducer back flush ports. Carefully insert a syringe with an adequately sized tip into the tubing of the back flush port, and pump water into the port. This water should travel through the 1/8” tubing and be discharged out the end of the high port 21 gauge needle.

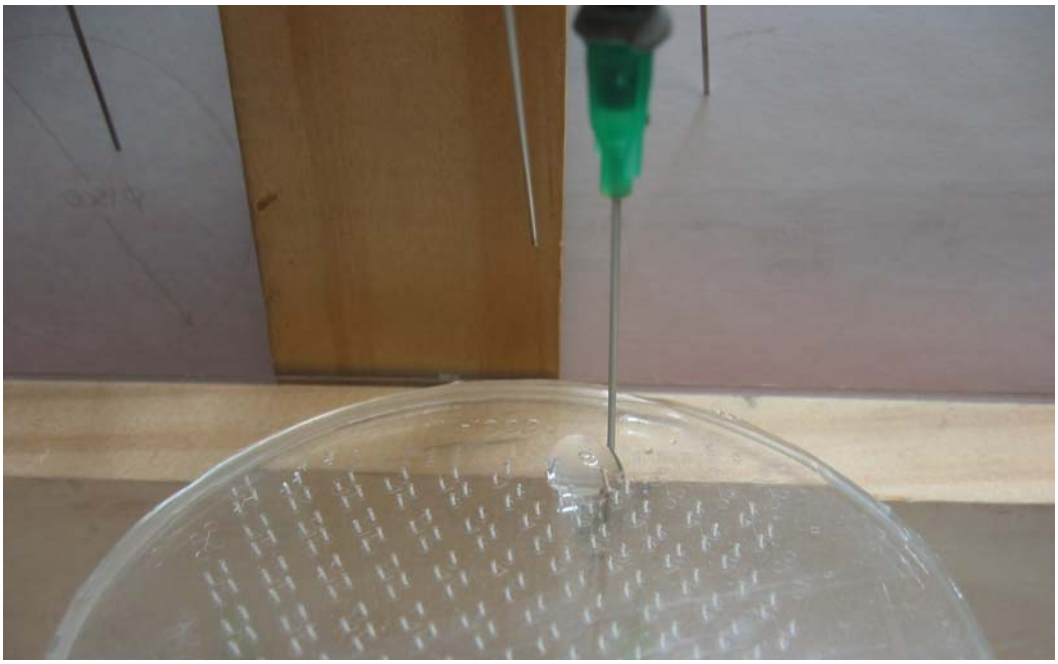

Figure 29: Microchannel with infusion needle inserted and a pool of liquid over the high port.

15. Place the tip of the high port needle into the pool of water over the high pressure port of the microchannel, and squeeze some more water out of the syringe in the back flush tube. This is to ensure no air pockets exist between the needle connected to the high port on the pressure transducer and the high port of the microchannel.
16. Insert the high port needle into the high port of the microchannel exactly how the infusion needle was inserted (about halfway through the top PDMS slab).
17. Remove the extra syringe from the high port back flush tube and ensure no bubbles exist in this tube.
18. Turn on the syringe pump and watch how water is pumped up through the high port pressure tubing and out of the back flush tube on the pressure transducer.

19. Wait for a drop or two to drip out, then turn off the syringe pump and plug up the back flush tube.
20. When the syringe pump is turned on again, liquid will be forced to travel out of the low pressure port (and possibly the exit port) since the high port has been plugged up.
21. Repeat steps 13 though 19 for the low pressure port.
22. When the syringe pump is turned on again, liquid will be forced to come out of the exit port only. After a pool of water forms over the exit port, insert the exit needle and ensure the liquid discharged is collected in an appropriate temporary storage tank that facilitates disposal after the test.
23. Turn the syringe pump back on and allow liquid to flow through the system for some time. Observe the DAQ software to ensure a pressure reading is being registered.
24. Turn off the pump, pull up a clean sheet to record voltage data from the actual test, and load the desired pumping program.
25. Start the actual test.

Now that the system has been adequately prepped and readied to conduct a test, a brief journey that the liquid will experience during a typical test will be described that shows how the flow provides measurable information that can be extracted from the set-up instrumentation. The interface between the macroscale and microscale worlds in this set-up with regards to test medium handling (flow delivery to channel, extraction from channel, and taps into the pressure ports) were all carefully controlled using the 21 gauge needles installed in the procedure above. The flow medium (distilled water) started in the 6cc syringe (after being drawn in from the storage tank previously), and was squeezed out of the syringe via the syringe pump at a

prescribed flow rate. The flow then passed through the check valve shown in Figure 25, entered 1/4" inner diameter tubing, stepped down to a 1/8” inner diameter tubing, and then flowed into the back of one of the 21 gauge needles and into the entry port of the microchannel test section. The flow then passed through the microchannel, depositing bits of water in the pressure ports on its way out of the channel until the ports were pressurized and the transducer began to register. After a short period, once the flow reached steady state, the test section was full of fluid and pressure measurements were extracted from the two pressure ports on either side of the microchannel test section utilizing two additional 21 gauge needles which led to the high and low ports of the differential pressure transducer via more 1/8” inner diameter tubing. Steady state flow (static pressure) information at each of the pressure ports was transferred very rapidly from the channel itself through the 20μm port opening in the flow stream, up the 21 gauge needle and 1/8” tubing, and into the differential pressure transducer for both the upstream and downstream pressure ports because the tubing was filled with the same incompressible fluid (distilled water) as the flow medium (through the back flushing process described above). If the ports were to be filled with a compressible gas (such as air at STP), the gas would first need to be compressed and equilibrated before pressure information could pass steadily through it and register a reliable measurement in the transducer. After passing through the test section, the flow is discharged to atmosphere via another 21 gauge needle at the exit port. As stated earlier, the only critical part of the test section is between the two pressure ports branching off the microchannel, as what happens upstream and downstream of these pressure ports is of no significance since it is either before the high pressure port, or after the low pressure port. The pressure transducer interprets the differences in pressures from each of the ports as a voltage difference, and relays that information to the DAQ system, which is connected (via voltage

recorder) to a computer terminal. At the computer terminal, the DAQ software records the voltage readings over the duration of the test at a sampling rate of about 1 reading per second (1 Hz) over the entire length of the test. The raw data is then saved in a format conducive to manipulation for analysis.

CHAPTER FOUR: RESULTS

The results and discoveries both during and after extensive testing never ceased throughout the entire duration of this work. The impending question of exactly how much to include in the scope of this work was ever present, and truncating interesting results and opportunities for further progress proved a difficult task. However, this work brought to light a very conclusive, though less glamorous, argument in support of the capabilities that macroscale fluid mechanics exhibit when modeling flow at the microscale in the presented size domains and Reynolds number regimes without any correlations or correction factors to describe anomalous effects being necessary. Before these results are shown, error tendencies in the data will be presented, along with applicable solutions to these problematic indicators to turn what may look like a bad test into a usable test upon retesting the exact same channel. Finally, some qualitative notions will be discussed as to why some tests should be questioned more than others, and recommendations made for future researchers.

Building the Comparison

After a test was conducted, the raw voltage data must first be converted into usable pressure data. Figure 30 represents a sample of raw voltage data sensed by the pressure transducer exported from the DAQ software into Microsoft Excel, with each of the flow rates marked above their respective shelves.

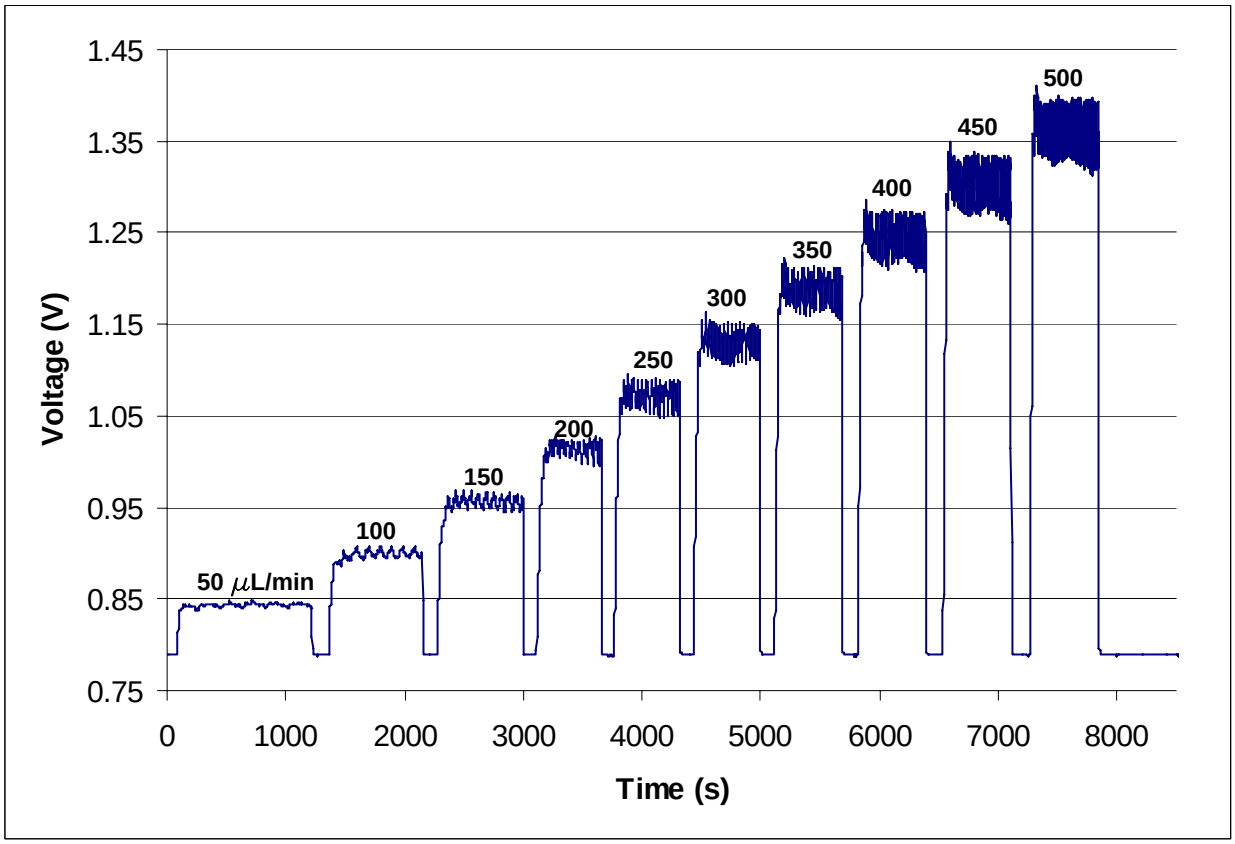

Figure 30: Raw voltage data.

A correlation between voltage and pressure was extrapolated via calibration using a u-tube water manometer. The pressurized end of the water manometer was connected to the high pressure port of the differential pressure transducer used for testing while the opposite ends of both the manometer and pressure transducer (low ports) were left open to atmosphere. Therefore, both the transducer and water manometer were functioning as a measure of the pressure difference between the pressurized end of the manometer, and atmospheric pressure. A correlation was extrapolated, the result of which is shown in Figure 31.

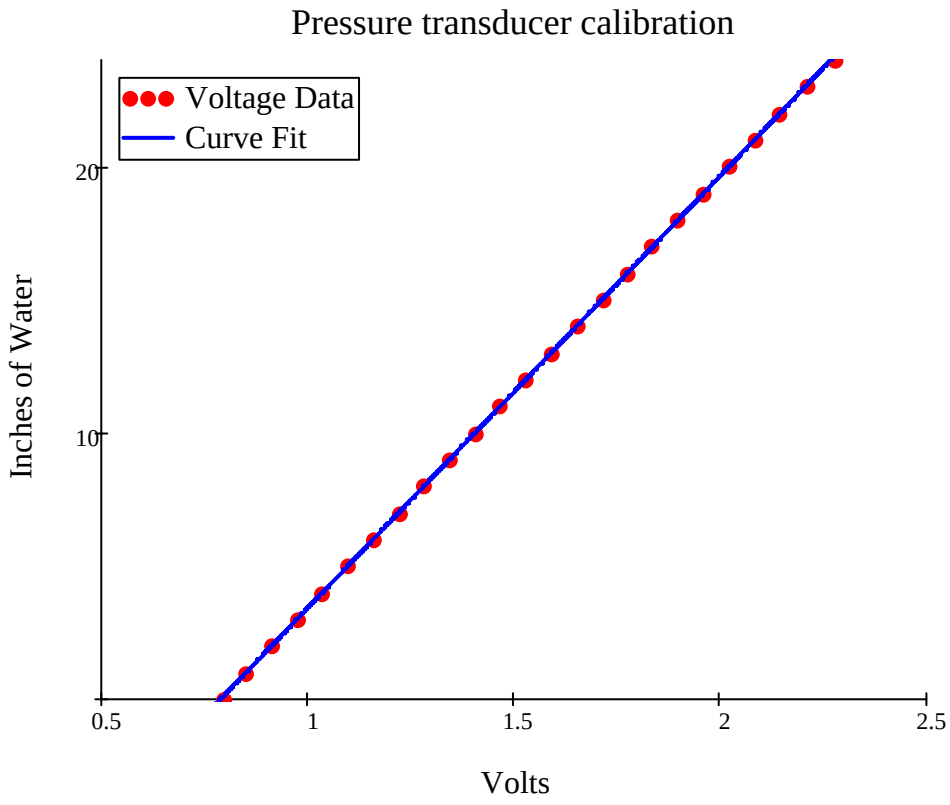

Figure 31: Calibration of differential pressure transducer. R^2 = 0.9999.

The voltage values at each of the 10 different flow rates in Figure 30 were averaged, and converted to pressure for comparison to theoretical predictions. Once this averaging and conversion process took place, the pressure was plotted as a function of Reynolds number, a typical plot for which can be found in Figure 32.

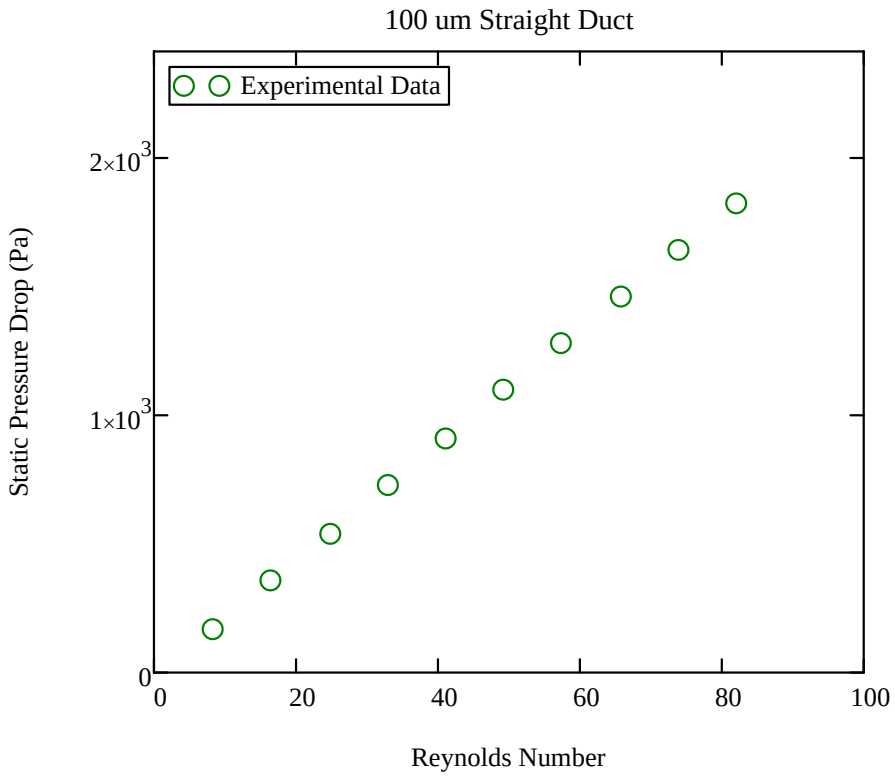

Figure 32: Plot of experimental data as a function of Re.

For the sake of thoroughness, the form of the theoretical modified Bernoulli equations used for comparison to this data can be found below for straight duct channels (Equation 19) and channels with sudden expansions and contractions (Equation 20). The theoretical predictions were plotted on the same graph with the experimental results to facilitate the comparison between the two. See Figure 33 for a graphical representation of this comparison for a sample straight duct.

$$p_1 - p_2 = \rho \cdot f \cdot \frac{L}{D_h} \cdot \frac{V^2}{2}$$ **Equation 19**

$$p_1 - p_2 = \left(\rho \cdot \frac{V^2}{2}\right)_{area_2} - \left(\rho \cdot \frac{V^2}{2}\right)_{area_1} + \left(\rho \cdot K \cdot \frac{V^2}{2}\right)_{area_{small}} + \left(\rho \cdot f \cdot \frac{L}{D_h} \cdot \frac{V^2}{2}\right)_{area_1} + \left(\rho \cdot f \cdot \frac{L}{D_h} \cdot \frac{V^2}{2}\right)_{area_2}$$

Equation 20

Dynamic Pressures Minor Losses Major Losses

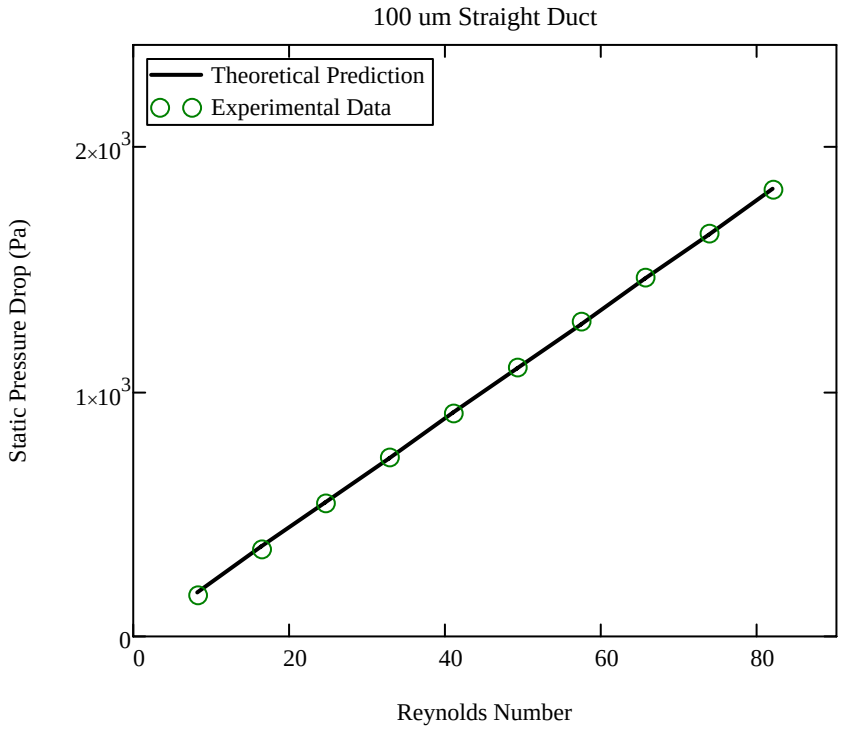

Figure 33: Sample comparison between theoretical predictions and experiments.

An uncertainty analysis was also carried out to quantitatively determine if deviations from theoretical predictions were due to expected error from the equipment (and or environment), or if these effects were due to some phenomena yet uncharted by the droves of

theory available. Table 6 gives a summary of the error accounted for, and Figure 34 is a copy of Figure 33 with the error bars representing the expected uncertainty in the pressure measurements.

Table 6: Uncertainty considered in all calculations.

Variable	Uncertainty
4x Pixel Conversion Measurements (for channel width)	8μm
10x Pixel Conversion Measurements (for channel length)	4μm
Fluid Temperature (affects fluid density & viscosity)	$\pm$ 1°C
Flow Rate	10%

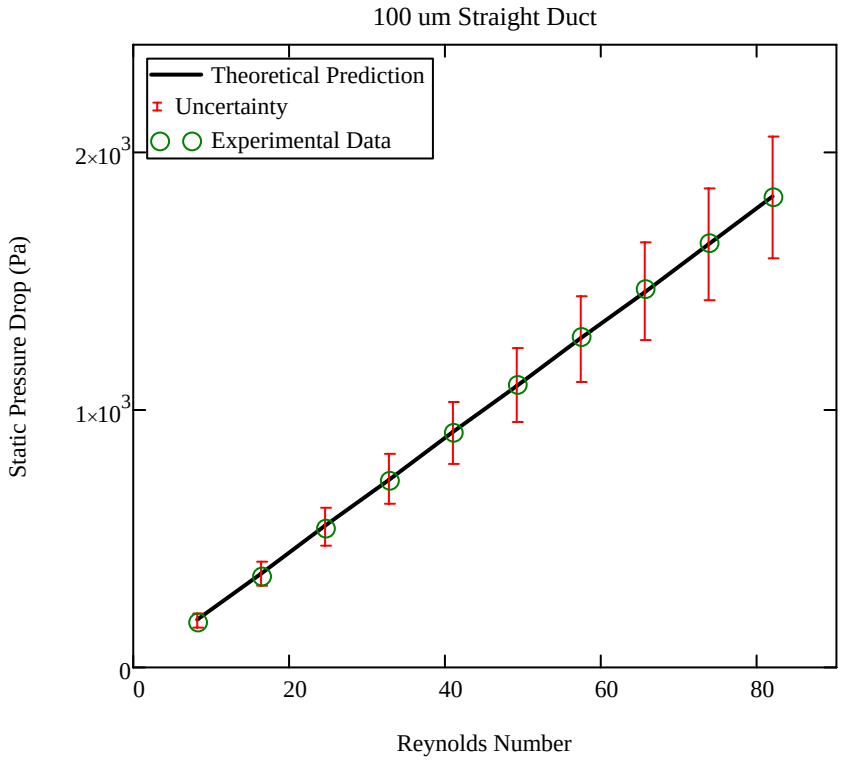

Figure 34: Figure 33 with error bars included.

The individual elements making up the uncertainty calculation remained constant per Table 6, but their constant values propagated through the entire data analysis for theoretical

predictions. As a result, greater error was seen for smaller sized channels because the uncertainty in distance measurements of the channel geometry made up a greater percentage of the overall channel size. Conversely, larger channels exhibited a lower range of uncertainty due to this scaling relation. That being the case, uncertainty ranged from about 8% for larger channels to as much as 19% for smaller channels. The error bars will be present in all future figures of experimental and theoretical comparisons.

Explanations for Deviations from Theoretical Predictions

At this point, it is appropriate to discuss the fidelity of the data obtained from the 300+ experiments conducted. One of the first questions that came up during testing in observation of the many graphs (such as Figure 30) was "How do I know if I've got a good test?" The answer to that question is undoubtedly, "Every test is a good test," because more information is obtained about the channels, equipment, and set-up process with each test allowing for any improvements to be implemented into one (or multiple) of the critical components that make up thsese experiments. The question of whether or not the integrity of flow thorough the channel was maintained at desirable conditions was the more pointed (though also more difficult) question that demanded a response, but this also proved to be answerable once enough data was extracted and analyzed. A brief account of these error indicators will be presented at this point.

The first trend that revealed itself was the tracking of measured pressure values that fell below that of what macroscale theory predicted. As with any trend that deviated from theoretical predictions, it was initially hypothesized that this represented a phenomena of microfluidics that supported findings from other researchers, the notion that flow at these size domains should be

treated differently than their macroscale counterparts. However, to make this argument irrefutable, it had to be proven that no other adverse effects had taken place during testing to any of the many components of the test set-up or microchannels themselves. After careful observations, it was discovered that these tests were the result of a break in the oxygen-plasma bond between the two slabs of PDMS that allowed the channel geometric dimension to expand past their manufactured nominal size. This increased the channel hydraulic diameter (and subsequently, the flow path) registering lower than expected pressure drops across the test section. Figure 35 shows digital imagery of these effects taken with the digital microscope.

Figure 35: Channel leakage due to PDMS slab separation.

The major contributor to this detrimental effect was during the channel piercing process (outlined step-by-step in earlier sections). If the channels were pierced too roughly, or if the 21 gauge needle was in any way mishandled during the piercing process, this could result in the type of delamination mentioned above. If the channels were subjected to flow rates that increased the internal pressure to values greater than 20psi, as indicated by the Stanford

Microfluidics Foundry supplier, the channels would also be at risk of rupturing. The importance of technique when piercing these channels became a critical element during preparation and readiness processes prior to testing, and after improvements were made to this process, no further rupturing was experienced. Figure 36 gives a graphical depiction of a sample data set (with its theoretical prediction without any channel ruptures) of how this error manifested itself in the experiments. It can be seen from the figure that this type of error falls much lower than the calculated uncertainty deems allowable. Unfortunately, once a channel is believed to be ruptured, it cannot be repaired without tedious and time consuming methods, and is unusable in future experiments.

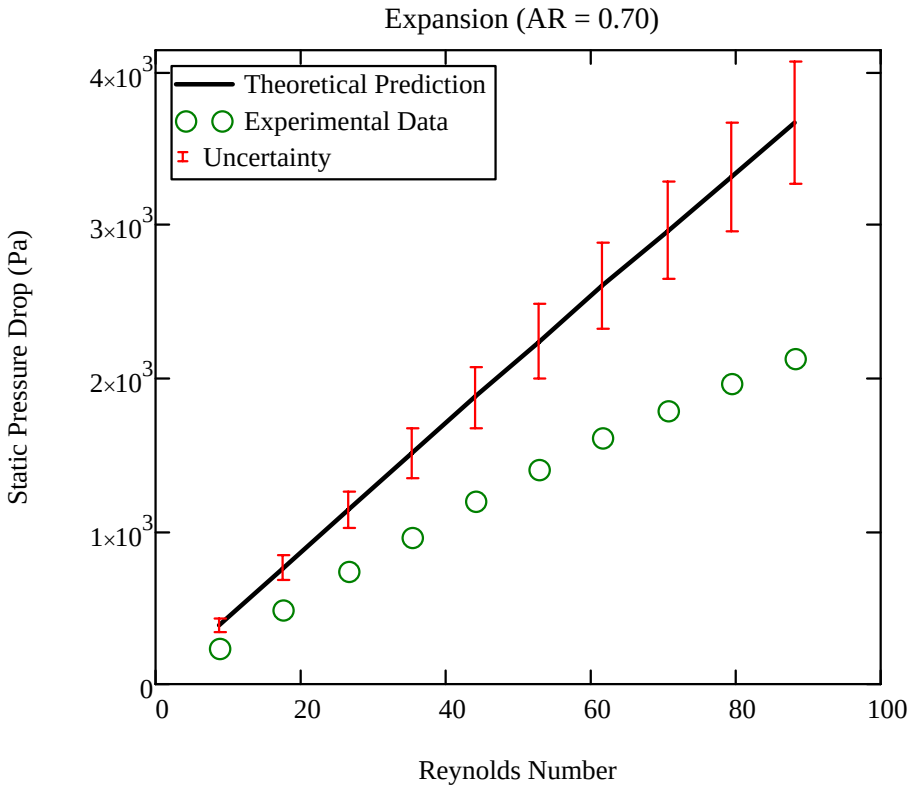

Figure 36: Data trend due to channel rupture compared to theoretical predictions.

Another type of error that produced a result quite contrary in behavior to the separation issue described above, though proved to be just as disadvantageous, was found in tests that contained measured pressures much greater than that of macroscale theoretical predictions. Once again, these measurements were thought to contain the presence of phenomena unconsidered by macroscale fluid mechanics and unique to flow only at the microscale. What is more is that this type of trend appeared more frequently at smaller scales than at larger ones, further supporting this notion of microscale effects occurring at smaller scales (and presenting a possible channel size transition region). However, these results underwent even greater scrutiny than the separation issue in order to verify that this effect wasn't a result of some defective characteristic of the set-up and experimentation procedure, as they were closely matched to the trends reported by researchers claiming that flow behavior deviated from macroscale theory at small scales. After rigorous analysis and experimentation, it was found that bubbles were present in the test sections of channels exhibiting these deviating results. This caution is present in a fair amount of the microfluidics literature on flow through microchannels, as well as micro fabrication literature. Due to the high surface to volume ratio of these small channels, capillary forces and surface tension are extremely high. If a bubble gets lodged in the channel and adheres to the channel wall due to this higher than normal surface tension effect, it would produce an undesirable (or additional) feature for the flow to pass over (similar to a nozzle/diffuser combination), thus producing higher than expected pressure losses when measured. Figure 37 is the digital image of a bubble just prior to the low pressure port in one of the microchannel test sections.

Figure 37: Bubble obstructing the flow in the test section.

Since the error in pressure data caused by the presence of bubbles in the test section was nondestructive in nature (as opposed to the channel leakage error type), the bubble could be carefully cleared out and the channel retested. Figure 38 shows a plot of a 60 micrometer straight duct tested with and without a bubble compared to its theoretical predictions.

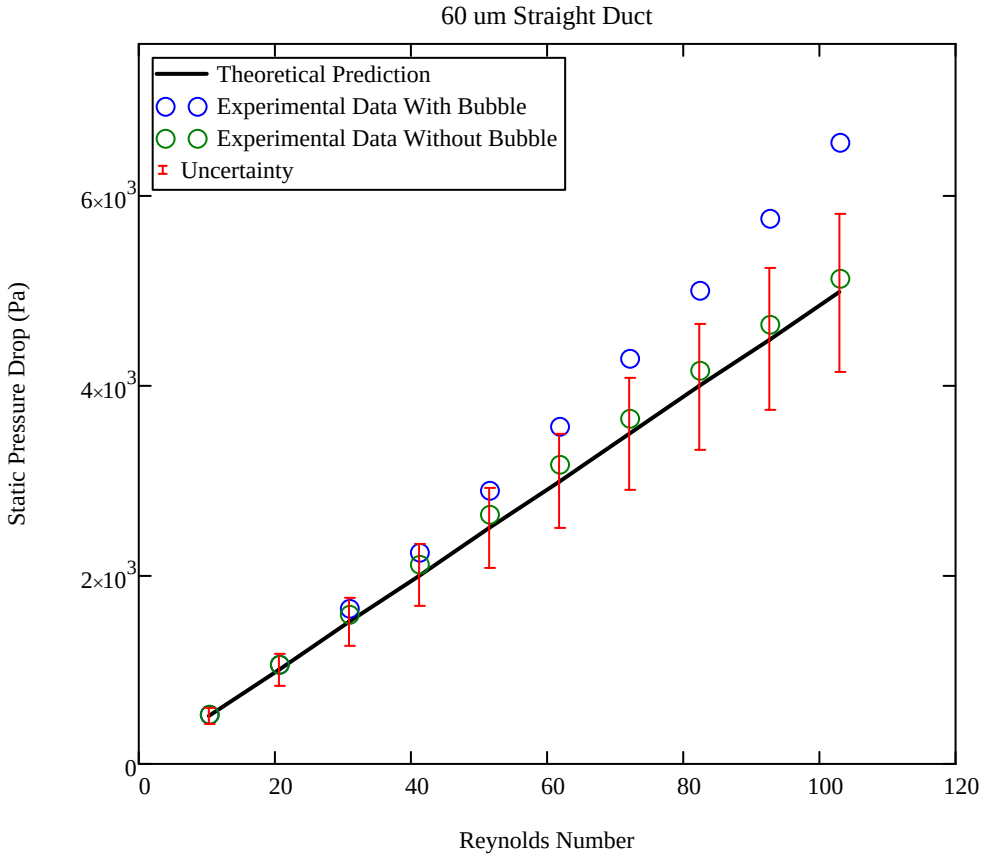

Figure 38: Plot of data with and without bubbles.

With these failure modes in place, two very critical "zones of error" can be marked as governing philosophies for the initial analysis of all data. Any trends exhibiting pressure values severely greater than macroscale predictions should be examined for the presence of bubbles. These bubbles can be flushed out of the channel test sections by carefully plugging up ports and flushing liquid through the channels at higher flow rates. Once flushed, the channels can be retested and clean, accurate data obtained. Trends exhibiting pressure values much lower than microscale predictions should be carefully examined for any leakage or separation between the

slabs of PDMS. Unfortunately, this type of occurrence renders the channel of no use to future experiments. Figure 39 depicts a sketch with these error zones identified.

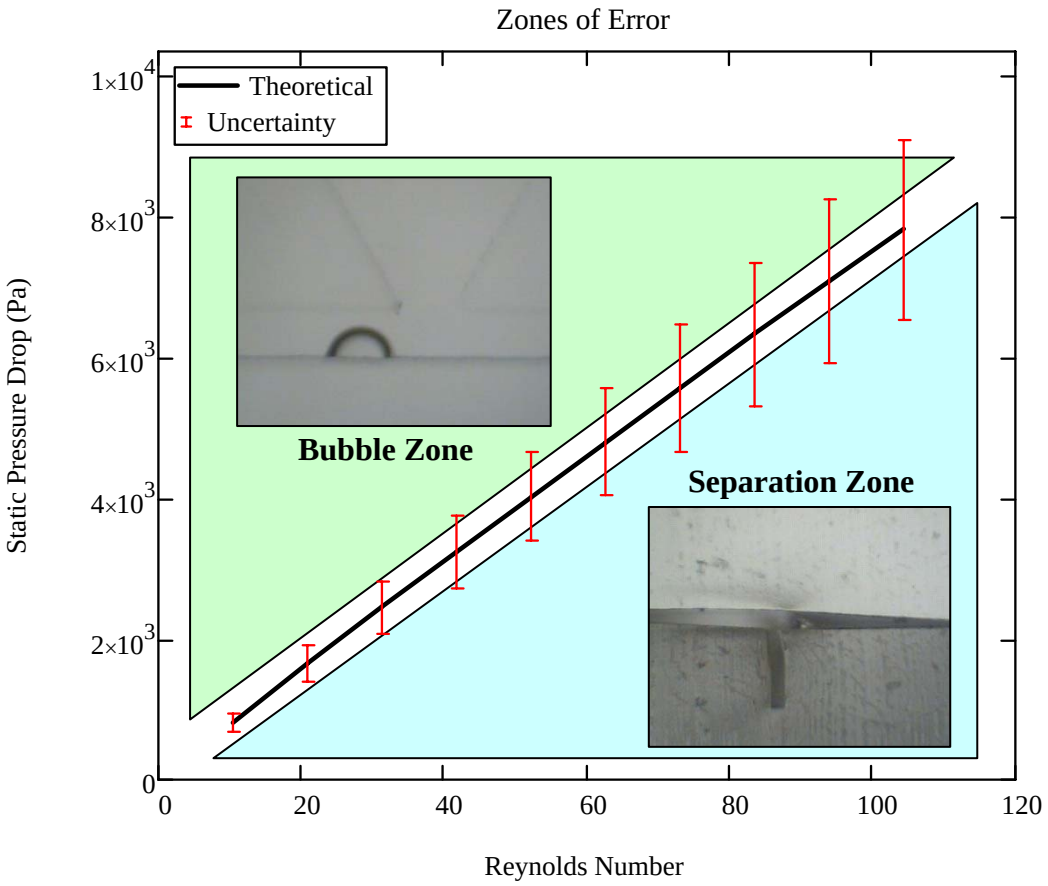

Figure 39: Zones of error for experimental results.

These findings present a possible explanation for why results from other researchers were claimed to fall either above or below macroscale theory predictions. It is hoped that before any results were reported that these tainting qualities to the flow integrity were found to be nonexistent beyond all reasonable doubt. With some of the materials used in other works being

nontransparent (such as micro-machined stainless steel), it would be difficult to observe the entire flow area without advanced imaging techniques. This is one advantage to using the transparent polymer PDMS as it allows for viewing of the entire channel with a simple microscope of ample magnification. For the sake of continuity and completeness to this discovery, Figure 2 has been presented again, this time marking the same zones of error shown above in Figure 39, the result of which can be found below Figure 40.

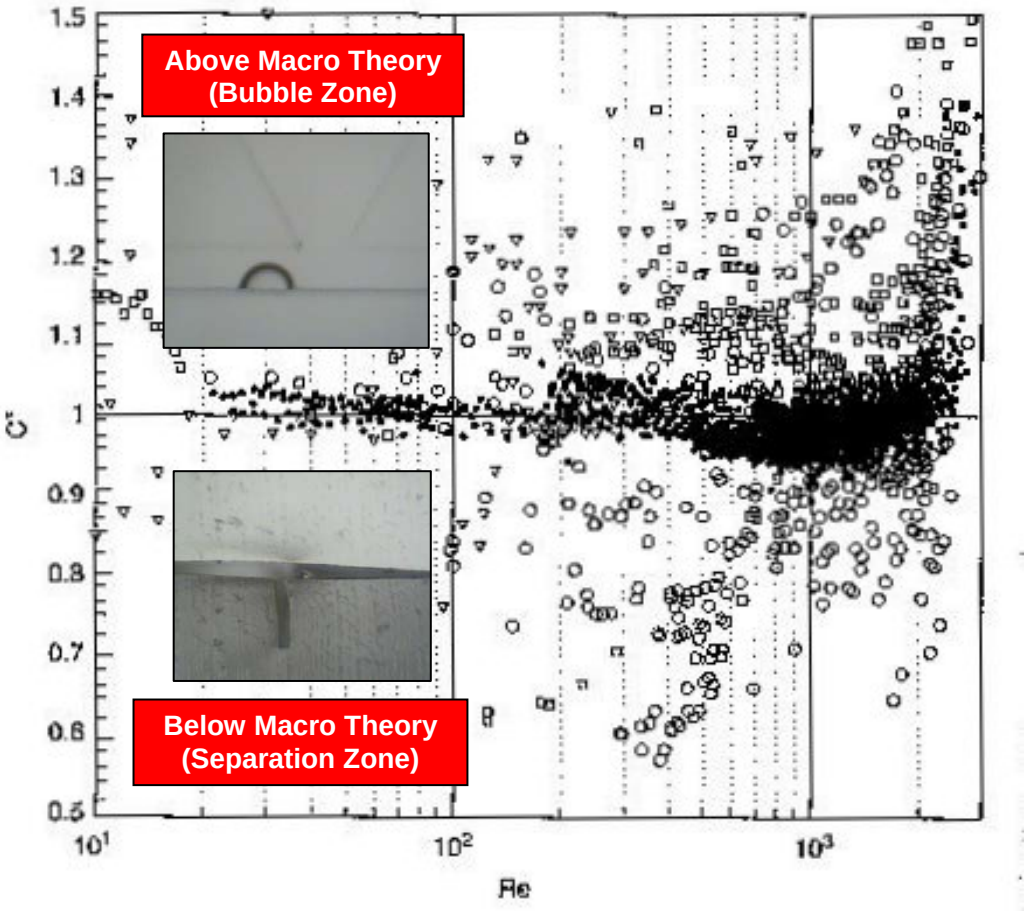

Figure 40: Figure 2 with zones of error marked.

Straight Duct Comparisons and Discussion

It is fitting at this point to display some sample results from the copious tests conducted over the duration of this work. The first few plots that will be displayed are for straight ducts tested at various channel widths (50 to 130 micrometers). Any necessary discussion will follow directly after display of the figures, so ample observation on behalf of the reader can be made during the discussion that follows. All plots shown will include points from every valid data set converted to pressure (and discarding any sets in error as described above) combined with the averaged theoretical prediction for the given channel size under analysis (based on measurements of actual channel geometry). The black line will represent this averaged theoretical prediction, and the green circles will represent actual data points measured. The vertical red error bars indicate the calculated uncertainty.

Equation 19 was used as the macroscale flow predictor for all straight duct data comparison (reprinted below).

$$p_1 - p_2 = \rho \cdot f \cdot \frac{L}{D_h} \cdot \frac{V^2}{2} \qquad \textbf{Equation 19}$$

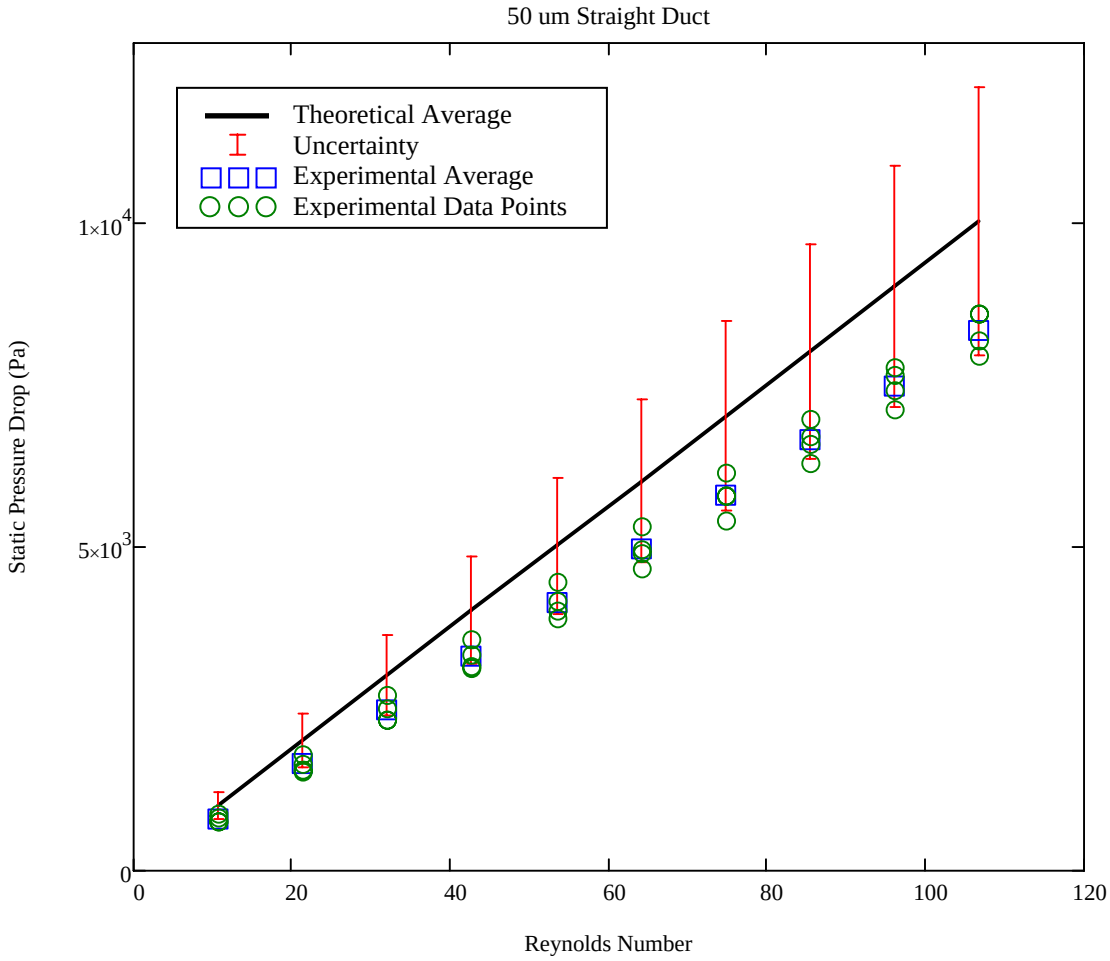

Figure 41: 50 micrometer straight duct results.

It is worth noting that the 50 micrometer straight duct channel data is consistently on the low end of the calculated uncertainty (as shown in Figure 41). This data was verified, and assuredly the channels did not leak during testing. The lower than predicted pressure drop is proposed to be the result of a summation of extremities reached by the measurement equipment and channel manufacturing process. Channels of this size were intentionally designed to the very edge of the aspect ratio limitations of the supplier's capabilities (5:1 designed height to

designed width), so anomalies were already expected to arise starting at this size. Also, measurements in this range are nearing the top full-scale error range of the pressure transducer, which is rated at 0.25 FSL. Even still, the majority of measurements fell within the accepted error range, but further testing should be conducted at and below 50 micrometers with comfortable aspect ratio manufacturing and appropriately ranged measurement equipment before any microscale flow anomalies can be concluded. Plots at all other straight duct channel sizes showed very good agreement with macroscale theory predictions.

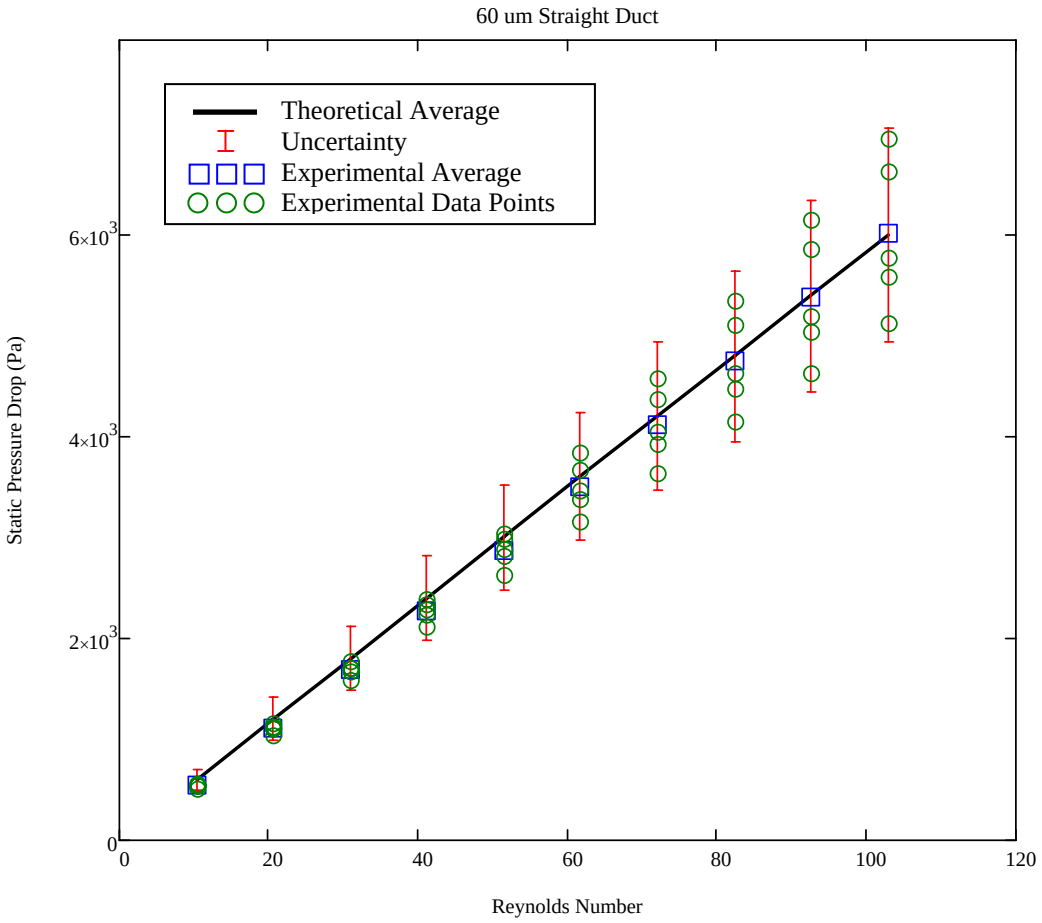

Figure 42: 60 micrometer straight duct results.

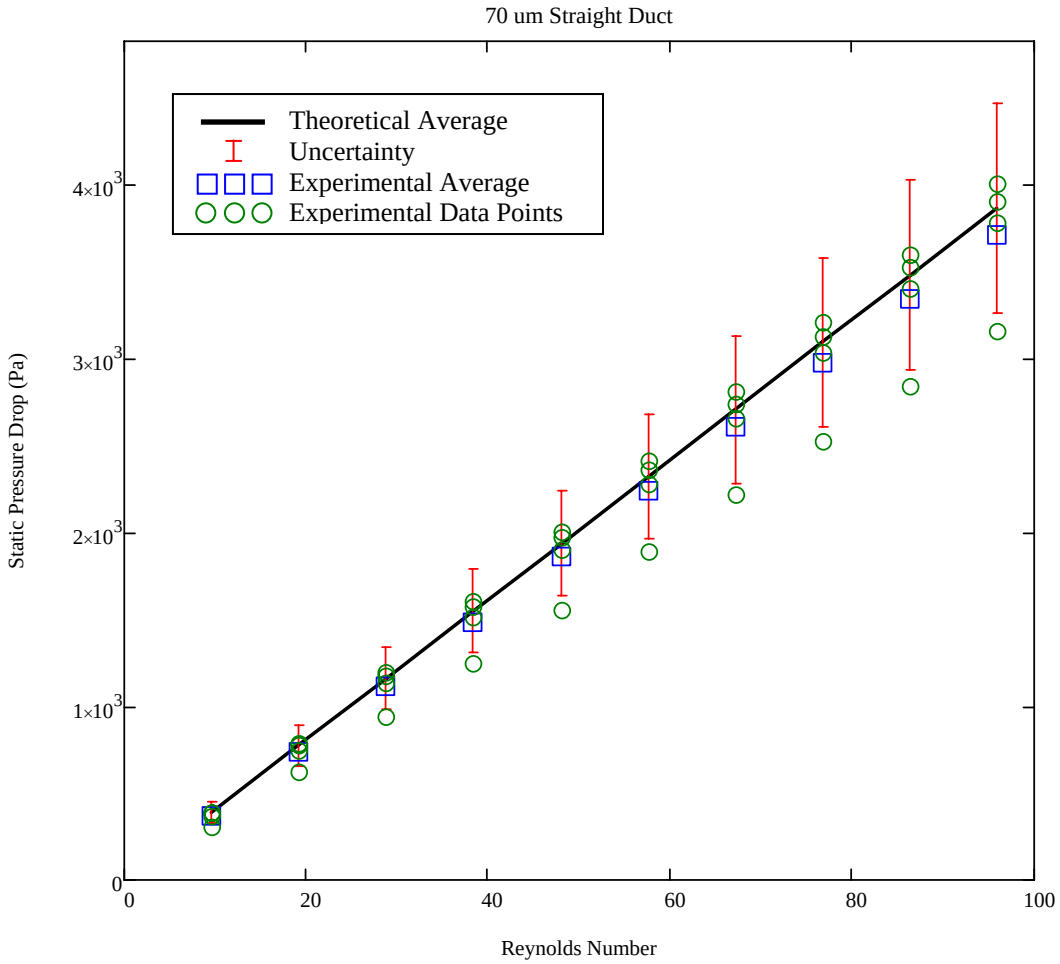

Figure 43: 70 micrometer straight duct results.

At times, the averaged plots containing multiple data points showed a single data set that was outside the range of uncertainty associated with the theoretical average (as shown above in Figure 43). At a first terse glance, this may seem like the presence of an outlier. However, in most cases this was not the final determination, as the theoretical averages were calculated by giving each of the data sets (and their geometric counterparts) equal weight. If a particular data set looked like it fell outside the range of uncertainty when viewed with other runs and compared

to the theoretical average, it was further reviewed and analyzed by comparing the specific set in question to its own theoretical prediction using the exact geometric dimensions of the particular channel (no averaging of other channel sizes factored in). This comparison nearly always produced a better fit between the theoretical prediction and the extracted data. An example of this analysis conducted for the specific data set that fell below the averaged error bars above in Figure 43 can be found in Figure 44.

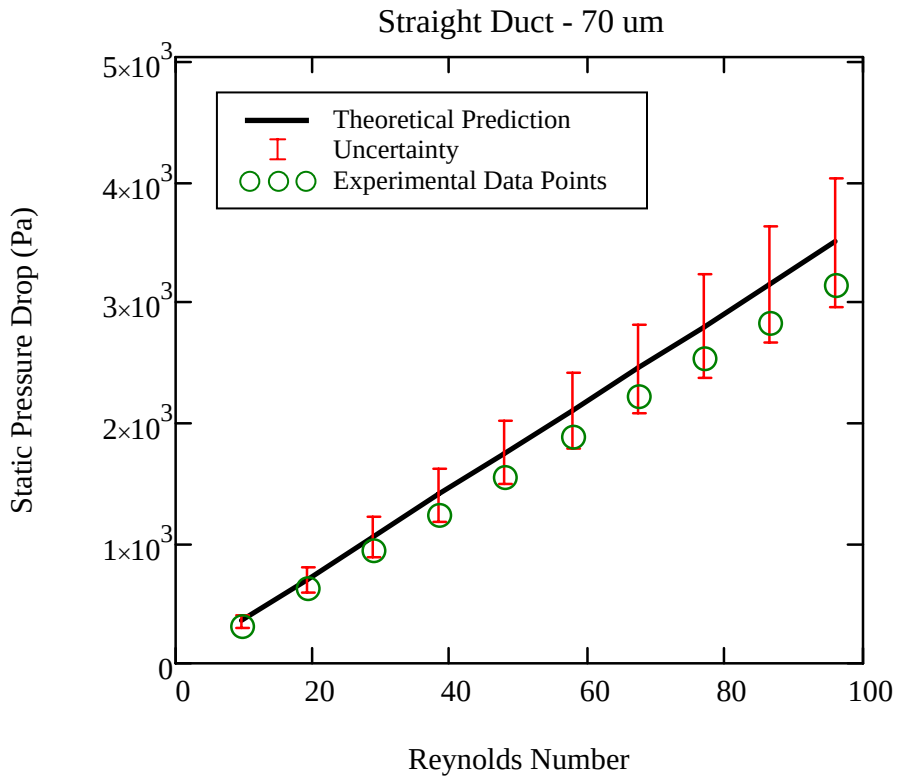

Figure 44: Analysis of a specific channel's data set compared to its own theoretical prediction.

It is for the sake of brevity that all successful runs are shown in a single plot with the overall size averaged theoretical prediction. All data presented in the following plots satisfied the secondary more rigorous comparison outlined above.

It can be seen from the figures that macroscale theoretical predictions accurately model fluid flow for the sample of straight duct microchannels tested within the range of uncertainty. Additional averaged plots for straight duct comparisons can be found in Appendix A.

Sudden Expansion Comparisons and Discussion

Next, sample plots of the tests conducted with area reduction features in the expansion flow configuration will be presented, with appropriate discussion as needed. Equation 20 was used as the macroscale theory predictor, with K_e values given by the relation outlined Equation 15 (and Figure 7).

$$p_1 - p_2 = \left(\rho \cdot \frac{V^2}{2}\right)_{area_2} - \left(\rho \cdot \frac{V^2}{2}\right)_{area_1} + \left(\rho \cdot K \cdot \frac{V^2}{2}\right)_{area_{small}} + \left(\rho \cdot f \cdot \frac{L}{D_h} \cdot \frac{V^2}{2}\right)_{area_1} + \left(\rho \cdot f \cdot \frac{L}{D_h} \cdot \frac{V^2}{2}\right)_{area_2} \quad \textbf{Equation 20}$$

Dynamic Pressures Minor Losses Major Losses

$$K_e = (1 - AR)^2 \quad \textbf{Equation 15}$$

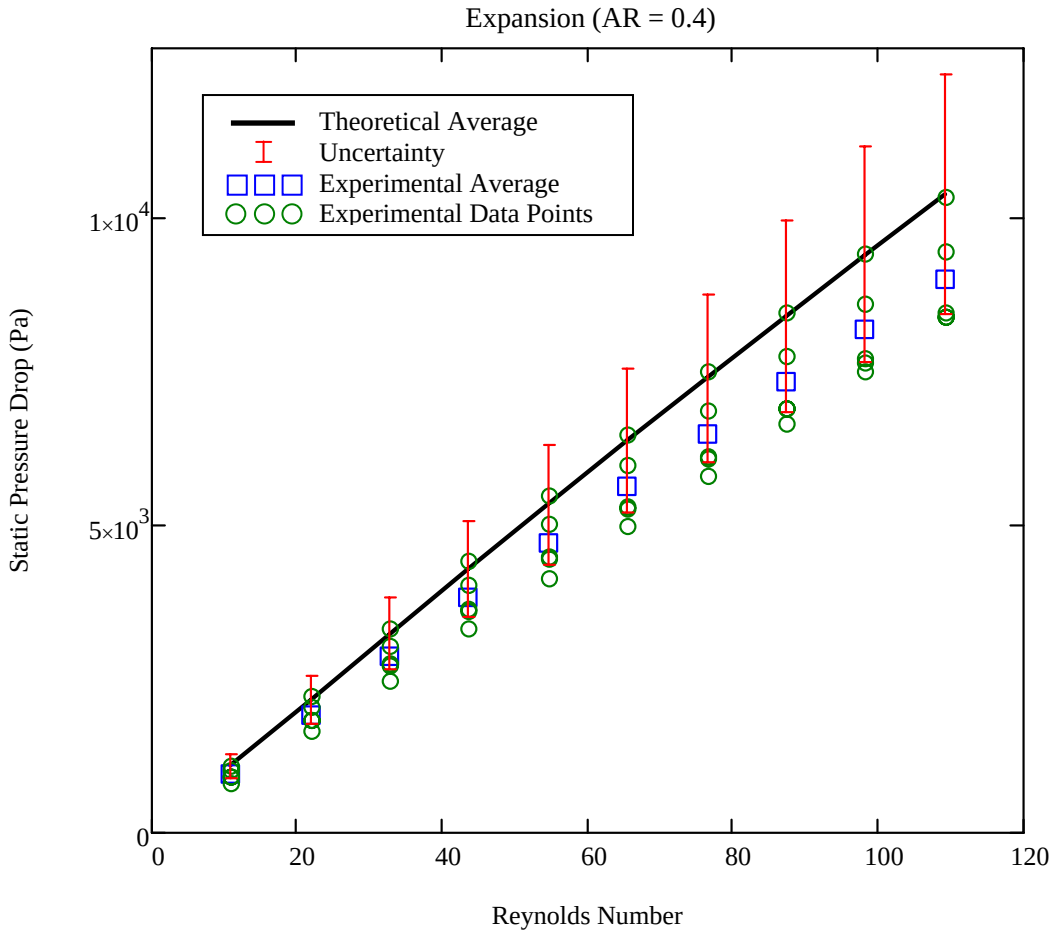

Figure 45: Expansion results for area ratio of 0.4.

Similar phenomena to the higher predictions by theory at the smallest size for straight ducts (50 micrometers) can bee seen for the sudden expansion from 50 micrometers to 130 micrometers (AR ~ 0.4), though not as extreme. This is thought to be for the same reasons proposed earlier for straight duct comparisons, though included in these reasons should be the rounding effects seen in the expansion feature (refer to Figure 19) for aspect ratio's that are at (or very close) to the limitations of the fabrication process (5:1). All other area ratios for sudden expansion show excellent agreement with macroscale theoretical predictions.

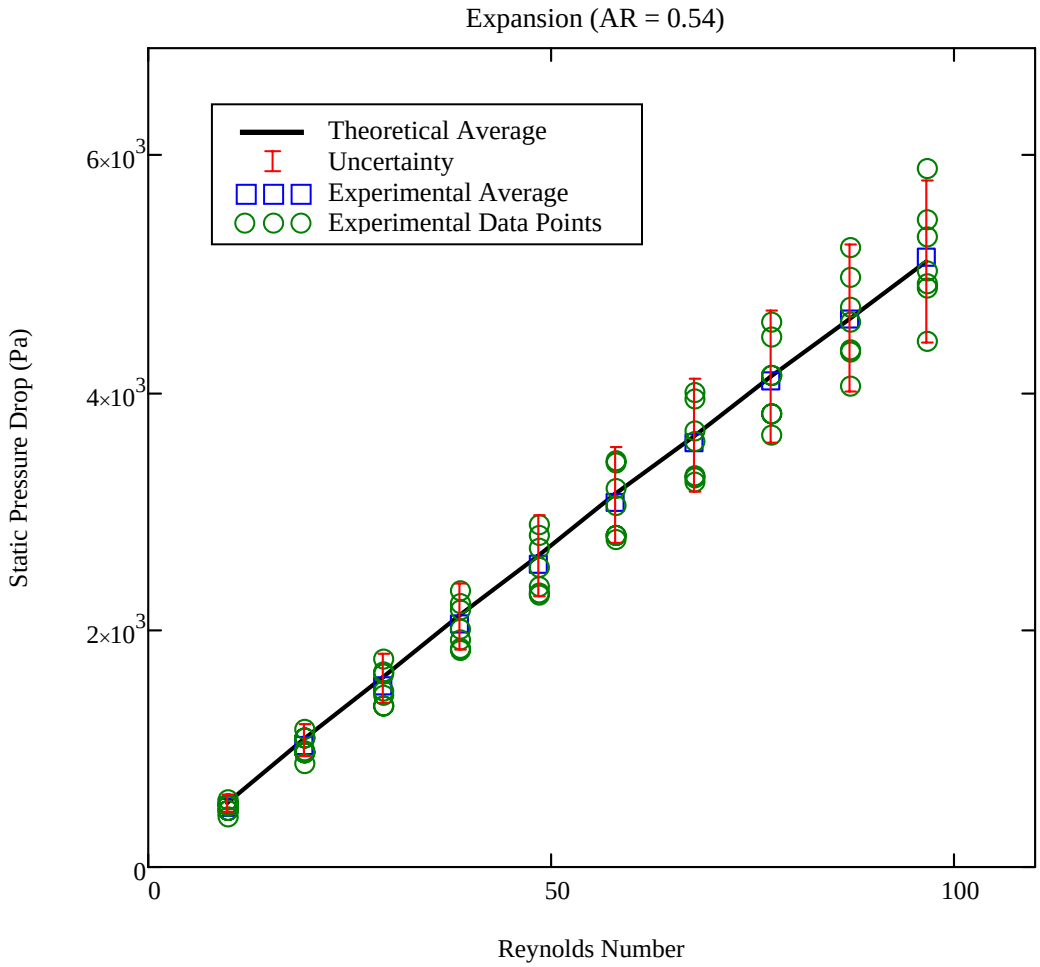

Figure 46: Expansion results for area ratio of 0.54.

Additional averaged plots for sudden expansion comparisons can be found in Appendix B.

Sudden Contraction Comparisons and Discussion

Microchannels with sudden contractions showed very little (if any) deviation from macroscale predictions, even for sizes that caused some low-end bias in prior plots. For these comparisons, Equation 20 was once again employed, only the minor loss coefficient was for that

of describing a sudden contraction (K_c) instead of a sudden expansion (K_e), utilizing adequate empirical correlations for its values (as indicated in Figure 7).

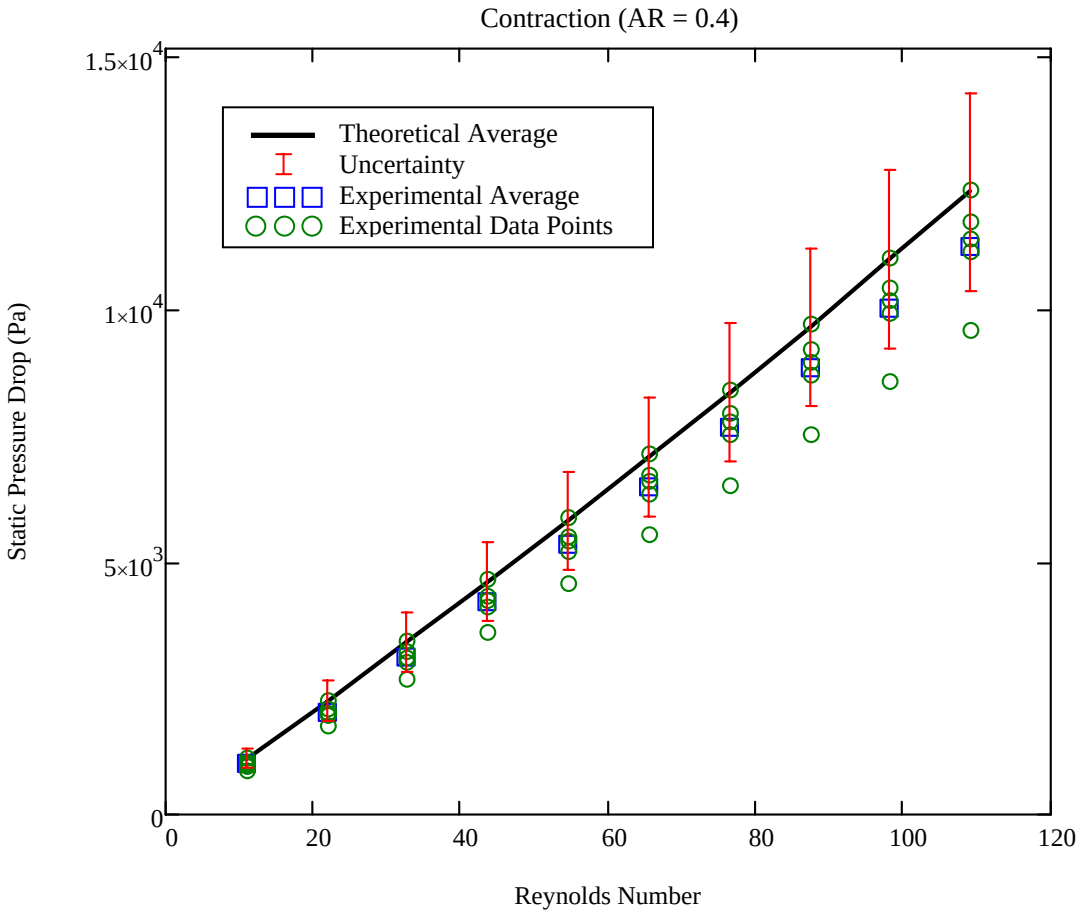

Figure 47: Contraction results for area ratio of 0.4.

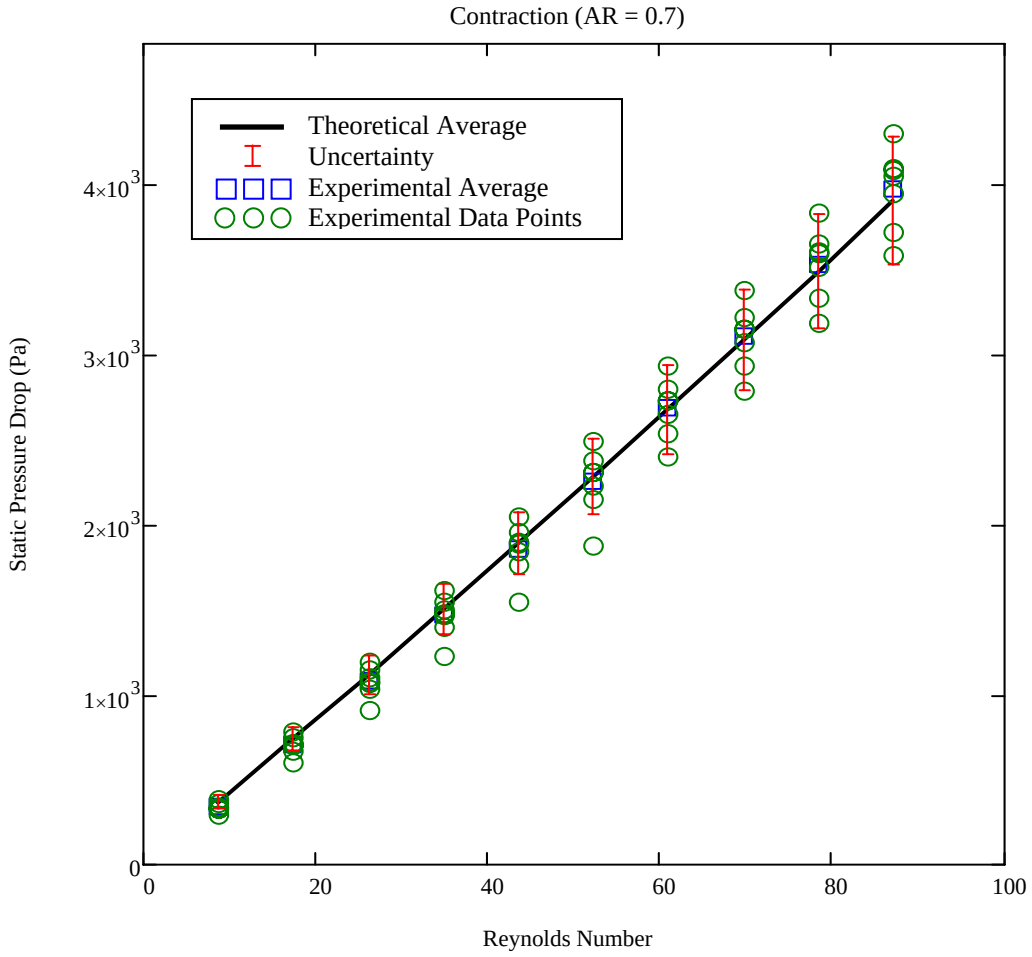

Figure 48: Contraction results for area ratio of 0.7.

Additional averaged plots for sudden contraction comparisons can be found in Appendix C.

Additional Considerations

Even though the channels contained anomalies mentioned before as a result of the fabrication process (rounded corners of area reduction feature, etc.), the flow through these channels were still predicted accurately by macroscale relations. It can be surmised, then, that the head loss experienced as a result of flow through these microchannels is due largely to the major head losses (usually more than 90% of total head loss), hence the designation of "major," while the minor head losses usually accounted for much less (less than 10%) of the total head loss. This was later verified by some simple calculations to be accurate. For the simple geometry tested in this work, the expansion/contraction minor losses can almost be neglected from the flow model calculations without losing too much fidelity in the pressure drop results. This effect was also verified by some simple manipulations of the data. It is not recommended that analysts or researchers neglect any term in their loss calculations, however, (*especially* at these small scales) unless it significantly decreases the complexity of a flow model and its impact to the accuracy of the final solution is well understood. Please refer to Appendices A, B, and C for additional plots comparing macroscale predictions to experimental data.

CHAPTER FIVE: CONCLUSIONS

Given the controversial undertones in the field of microfluidics research, it was desired to provide a robust behavioral analysis of pressure drop experienced by liquid flow through simplified features, as most microfluidics research aims at analyzing broad systems containing numerous complex flow geometries and system components. Microchannels ranging in size from 50 microns to 130 microns were chosen that exhibited straight duct geometries (for replication of prior work), as well as sudden expansions and contractions in flow geometry due to the gaping chasm of research conducted on channels with these features.

Microchannels were designed and cast in the low cost, durable polymer PDMS and irreversibly sealed to another blank slab of PDMS by bonding techniques that utilized oxygen-plasma treatment, thereby allowing the microchannels to withstand internal pressures up to 20psi. This oxygen-plasma treatment deposited a thin coating on the microchannel walls, providing a hydrophilic film that permitted ample wetting of the channel surfaces by the test fluid. Over 300 experiments were conducted on the two PDMS chips (each containing 99 different channels) using a reliable test philosophy developed primarily by Hansel [19], with improved techniques developed during the channel piercing process. Pressure measurements were extracted and compared to theoretical predictions using accepted macroscale fluid mechanics in the form of Bernoulli's equations modified to account for major and minor head losses.

Given the surmounting evidence provided in this work, it can be concluded that macroscale theory predictions for uniform, steady, incompressible, internal flow through straight

ducts, as well as ducts with sudden area expansions/reductions serve as an accurate model for the flow behavior, with additional correlations and correction factors to account for microscale anomalies being unnecessary. These results have been validated for square shaped channel profiles with widths ranging from 50 microns to 130 microns, area ratios ranging from 0.4 to 1.0, with a channel height of 104 microns by this work. The flow regime was laminar, and remained in the Re = 7 to Re = 130 domain. The importance of precision technique when piercing the entrance, exit, and high/low pressure ports was discovered to be extremely vital in the successful testing of microchannels cast in PDMS. Processes described herein will hopefully guide future microfluidics research efforts when microchannels fabricated using this material are tested. Furthermore, anomalies experienced by other researchers within this size and Reynolds number range were most likely due to any number of error variables (or combination thereof) induced into the analysis in the form of fabrication limitations, test set-up, channel design, equipment selection, and overall experimentation philosophies. The two most prevalent failure modes uncovered in this work were the presence of bubbles in the channel test section, witch caused the pressure drop data to fall above that of macroscale theory predictions, and separation between the PDMS slabs around the microchannels due to rough handling or unsatisfactory technique when piercing channels, which caused the data to track lower than macroscale theory predictions.

It is recommended that supplementary research be conducted to further isolate the expansion/contraction feature, as flow effects analyzed in this work were predominately governed by the major loss (friction factor) term. It is also strongly advised that reliable manufacturing techniques be employed to fabricate channels smaller than 50 micrometers in width, and pressure losses measured using equipment with a suitable range. Finally, it is hoped

that no matter how convoluted or controversial a subject may become, researchers with a love for discovery and the dissemination of findings remain at forefront of the conclave.

APPENDIX A: ADDITIONAL PLOTS FOR STRAIGHT DUCT TESTS

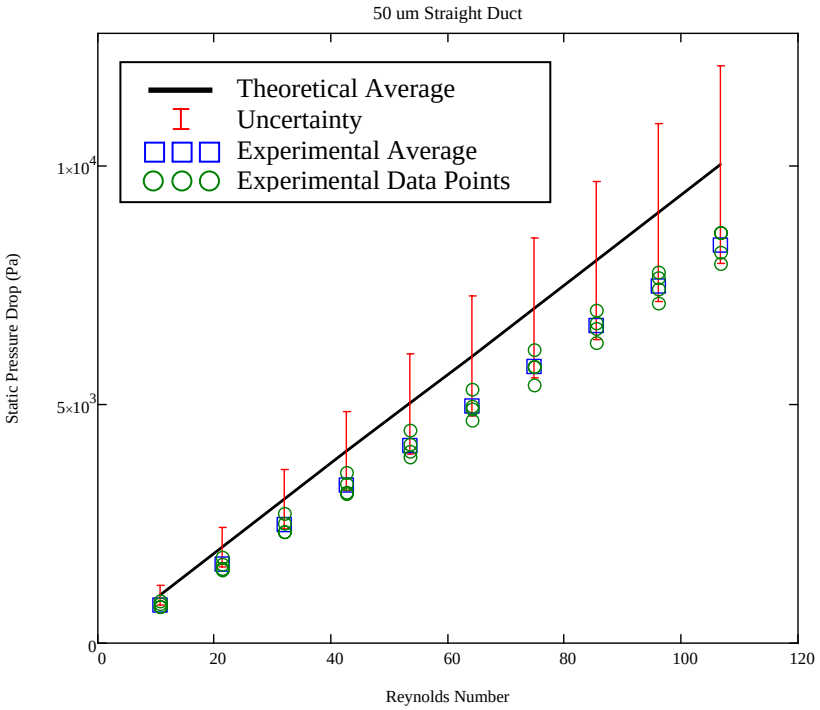

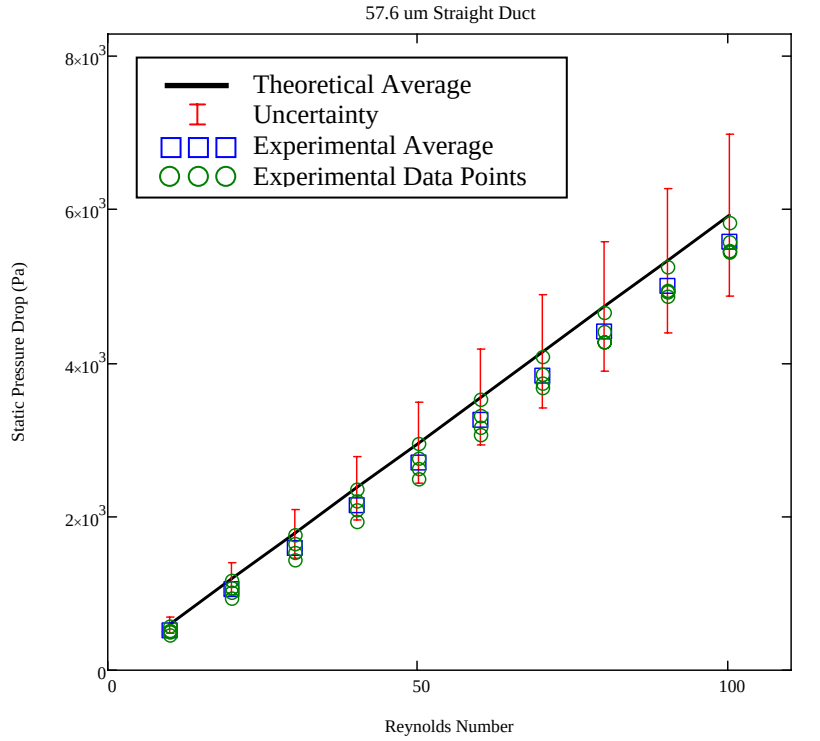

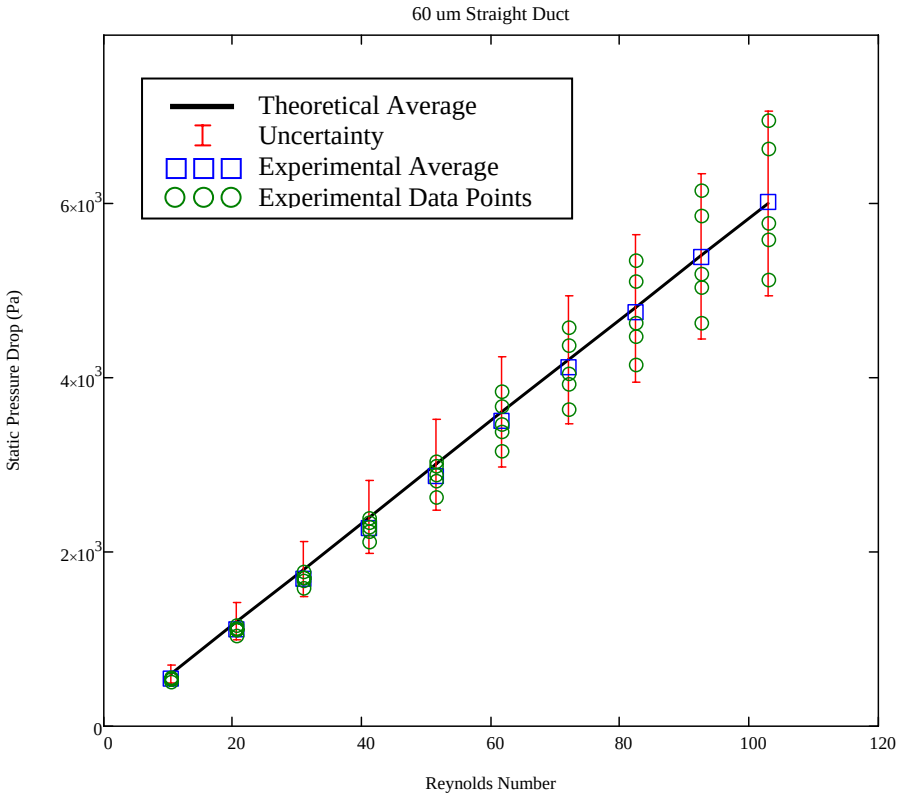
60 um Straight Duct
Theoretical Average
Uncertainty
Experimental Average
Experimental Data Points
Static Pressure Drop (Pa)
Reynolds Number
0
2×10^3
4×10^3
6×10^3
0
20
40
60
80
100
120

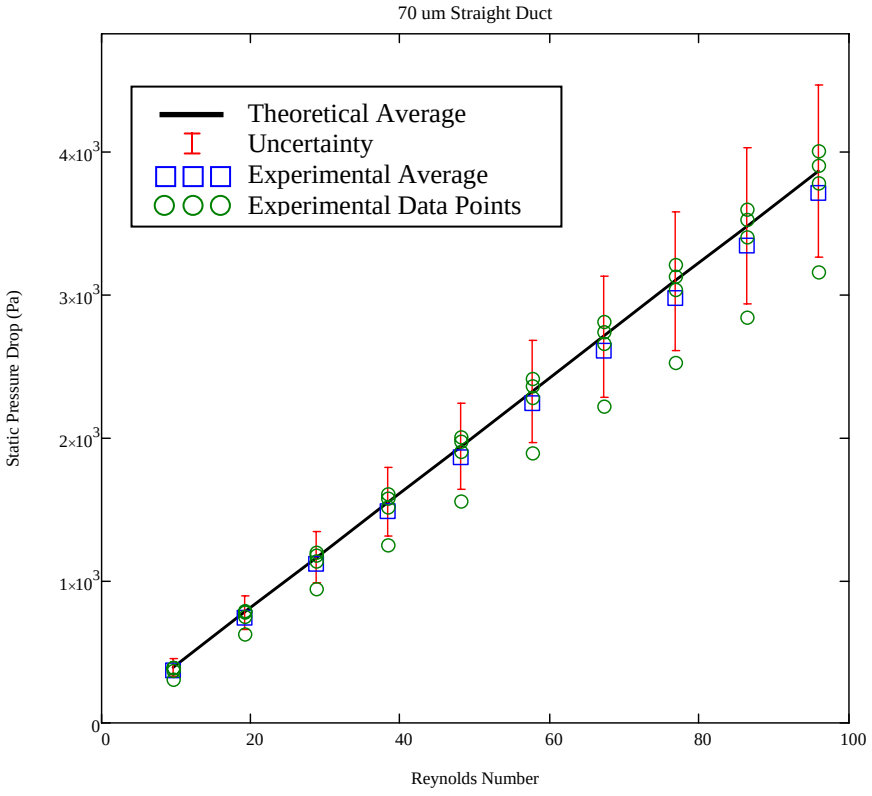
70 um Straight Duct
Theoretical Average
Uncertainty
Experimental Average
Experimental Data Points
Static Pressure Drop (Pa)
Reynolds Number
0
1×10^3
2×10^3
3×10^3
4×10^3
0
20
40
60
80
100

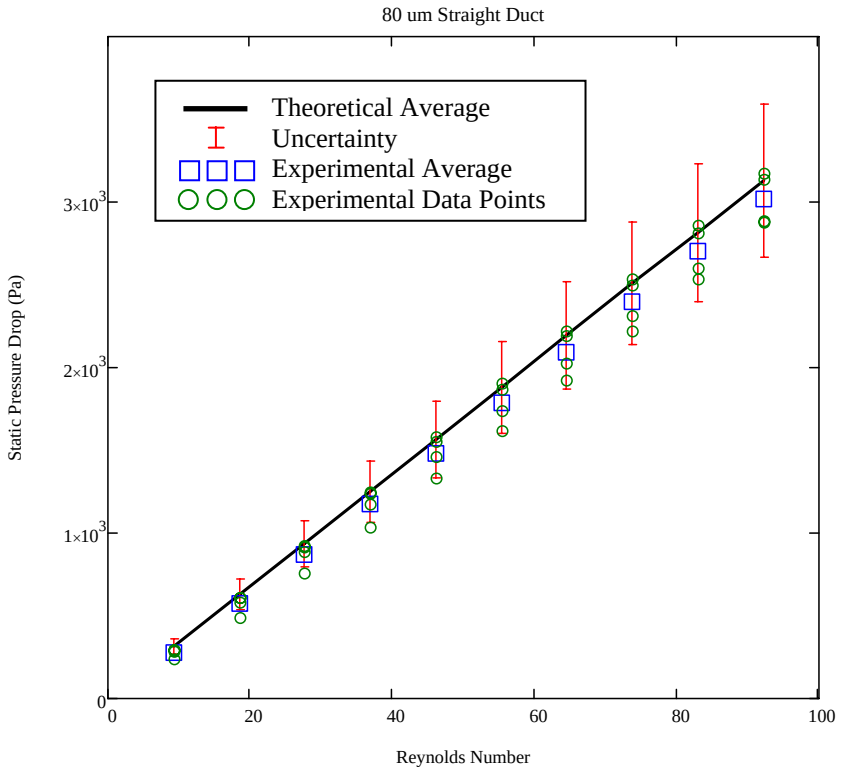
80 um Straight Duct
Theoretical Average
Uncertainty
Experimental Average
Experimental Data Points
Static Pressure Drop (Pa)
Reynolds Number
0
1×10^3
2×10^3
3×10^3
0
20
40
60
80
100

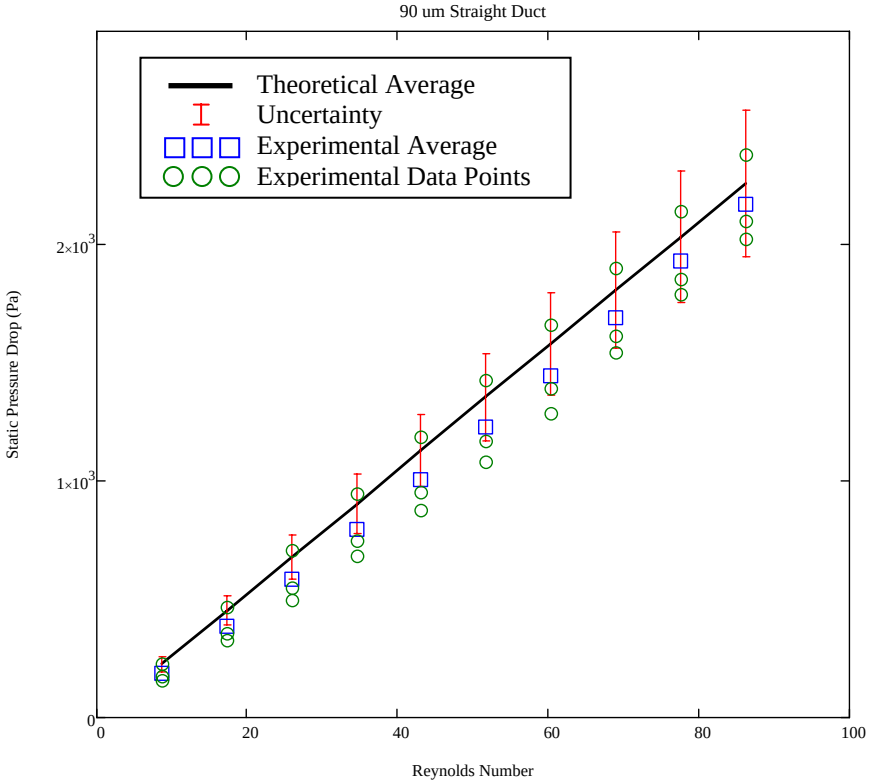
90 um Straight Duct
Theoretical Average
Uncertainty
Experimental Average
Experimental Data Points
Static Pressure Drop (Pa)
Reynolds Number
0
1×10^3
2×10^3
0
20
40
60
80
100

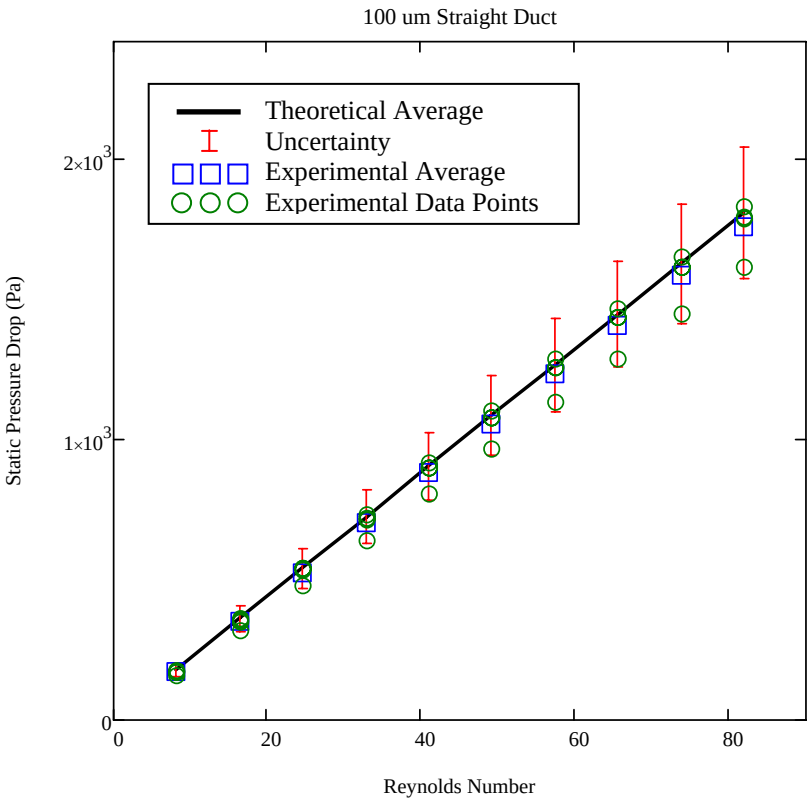
100 um Straight Duct
Theoretical Average
Uncertainty
Experimental Average
Experimental Data Points
Static Pressure Drop (Pa)
2×10^3
1×10^3
0
0
20
40
60
80
Reynolds Number

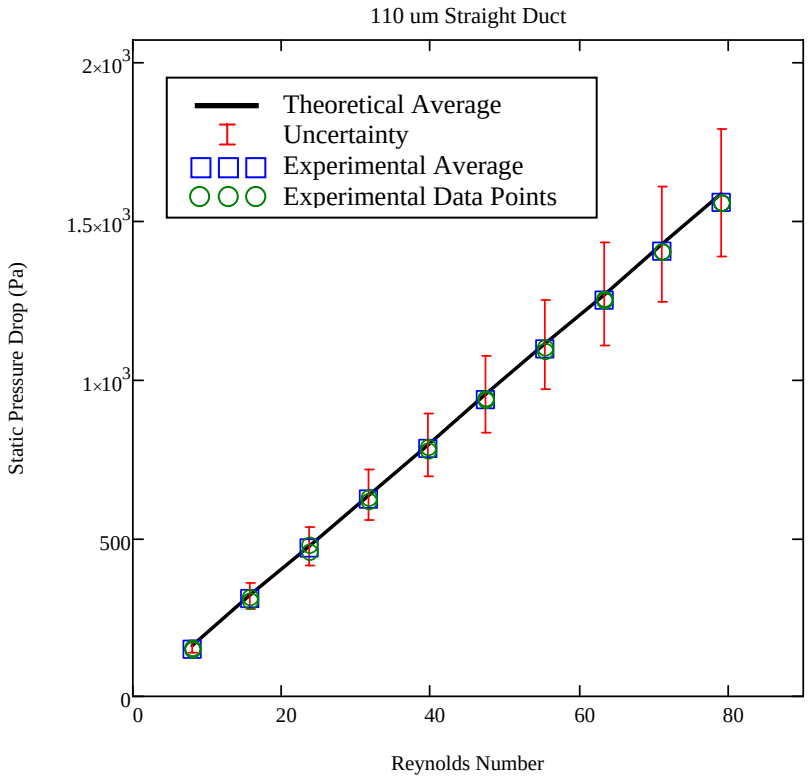
110 um Straight Duct
Theoretical Average
Uncertainty
Experimental Average
Experimental Data Points
Static Pressure Drop (Pa)
2×10^3
1.5×10^3
1×10^3
500
0
0
20
40
60
80
Reynolds Number

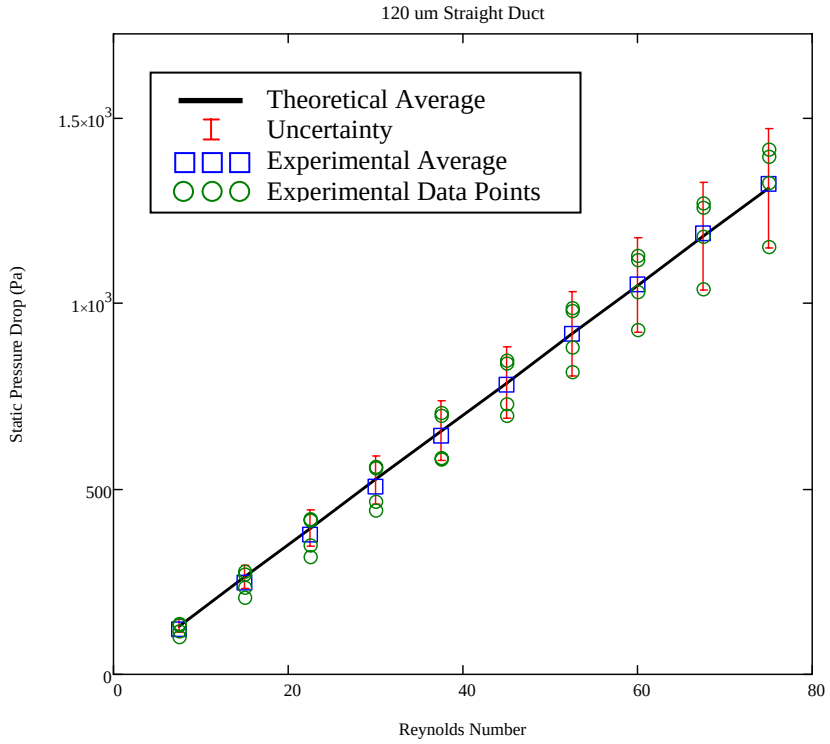
120 um Straight Duct
Theoretical Average
Uncertainty
Experimental Average
Experimental Data Points
Static Pressure Drop (Pa)
Reynolds Number
0
500
1×10^3
1.5×10^3
0
20
40
60
80

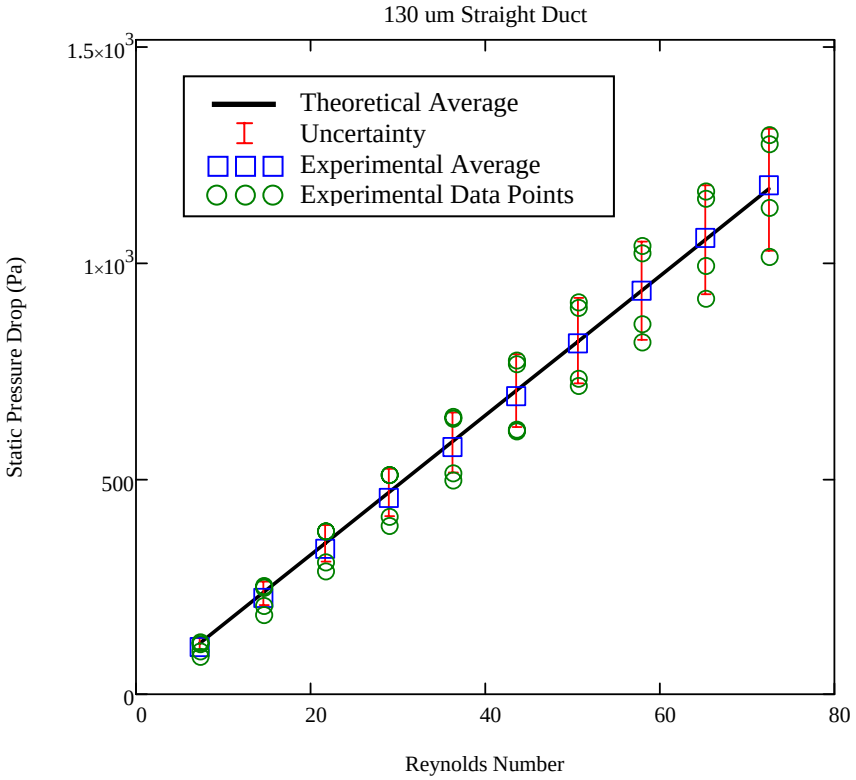
130 um Straight Duct
Theoretical Average
Uncertainty
Experimental Average
Experimental Data Points
Static Pressure Drop (Pa)
Reynolds Number
0
500
1×10^3
1.5×10^3
0
20
40
60
80

APPENDIX B: ADDITIONAL PLOTS FOR EXPANSION TESTS

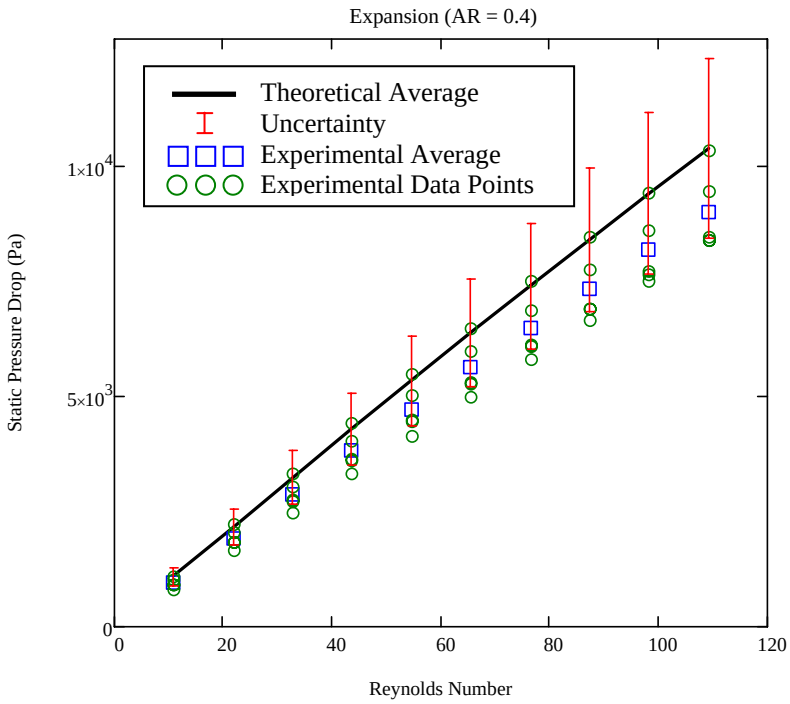

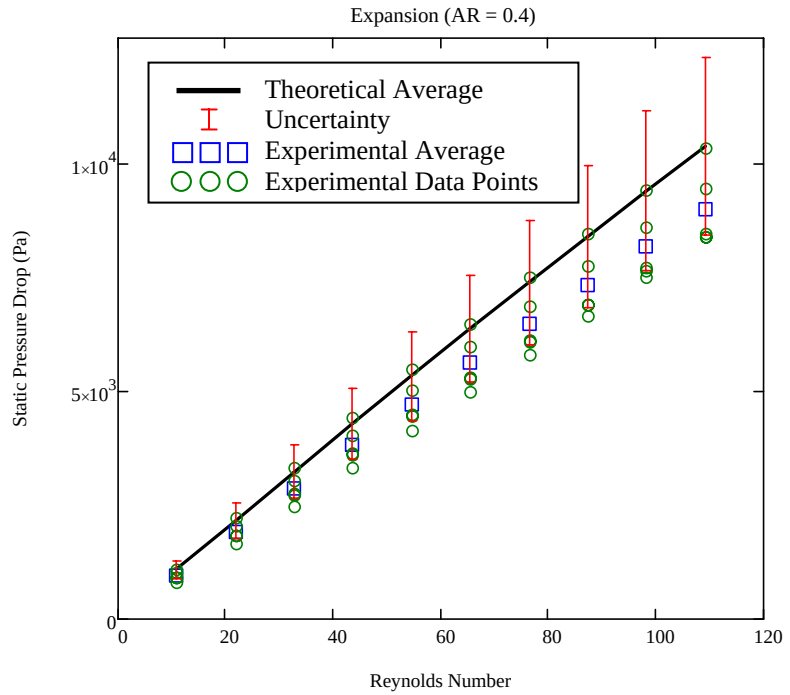

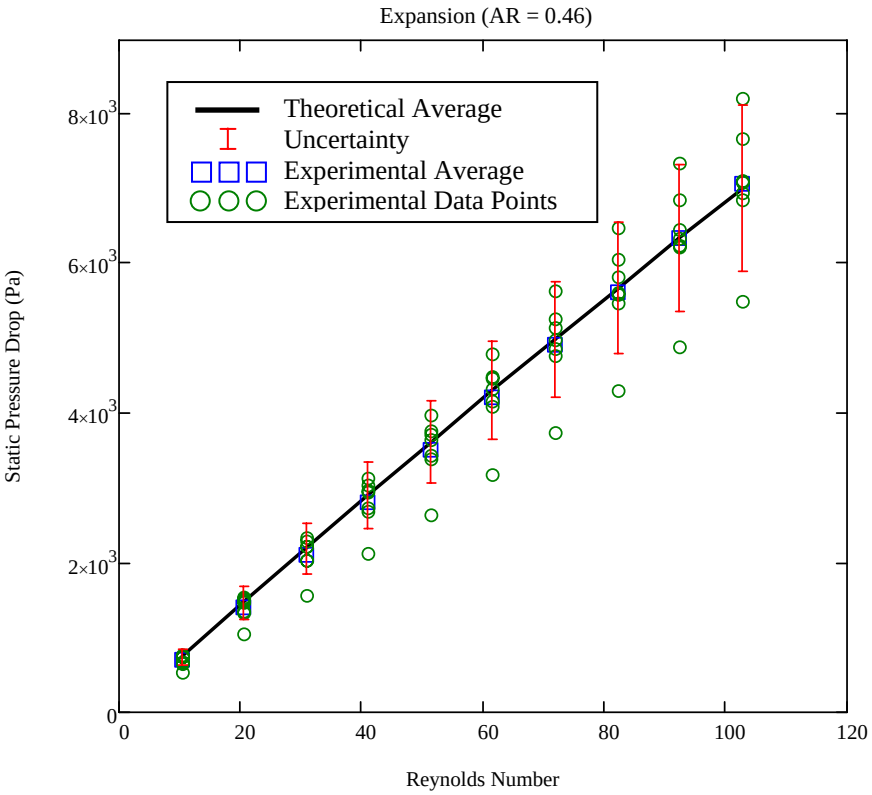
Expansion (AR = 0.46)
Theoretical Average
Uncertainty
Experimental Average
Experimental Data Points
Static Pressure Drop (Pa)
Reynolds Number
0
2×10^3
4×10^3
6×10^3
8×10^3
0
20
40
60
80
100
120

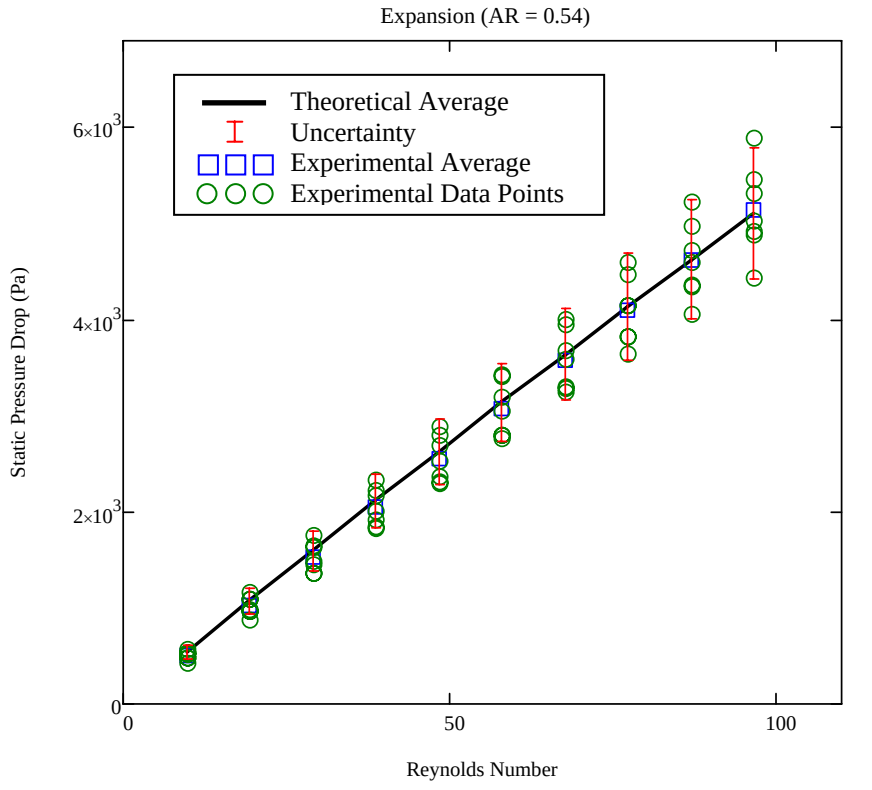
Expansion (AR = 0.54)
Theoretical Average
Uncertainty
Experimental Average
Experimental Data Points
Static Pressure Drop (Pa)
Reynolds Number
0
2×10^3
4×10^3
6×10^3
0
50
100

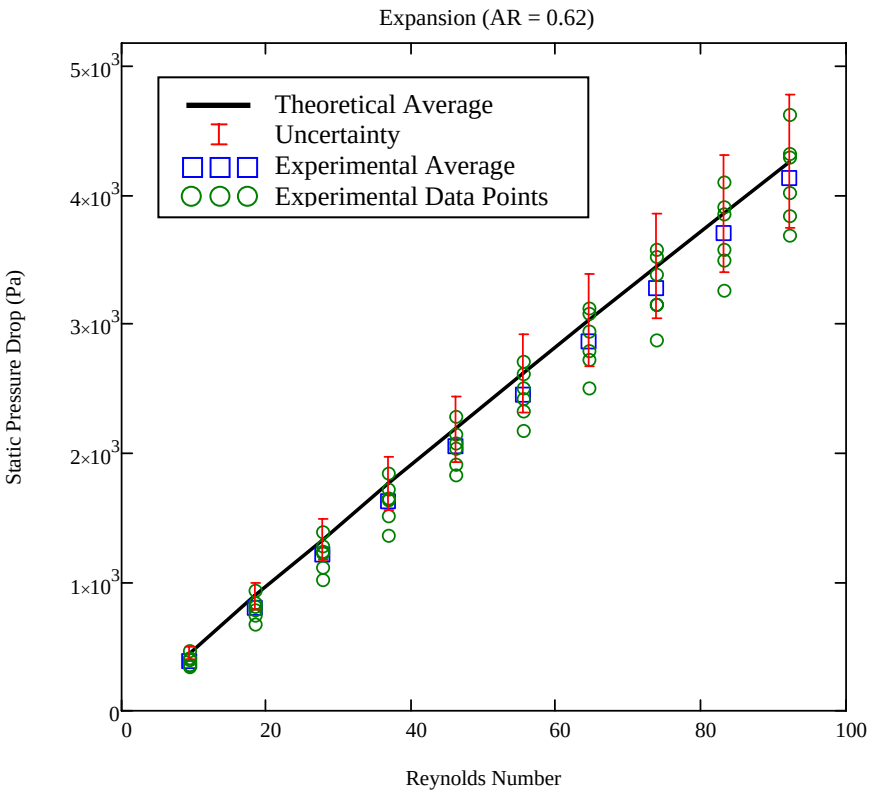
Expansion (AR = 0.62)
Theoretical Average
Uncertainty
Experimental Average
Experimental Data Points
Static Pressure Drop (Pa)
Reynolds Number
0
1×10^3
2×10^3
3×10^3
4×10^3
5×10^3
0
20
40
60
80
100

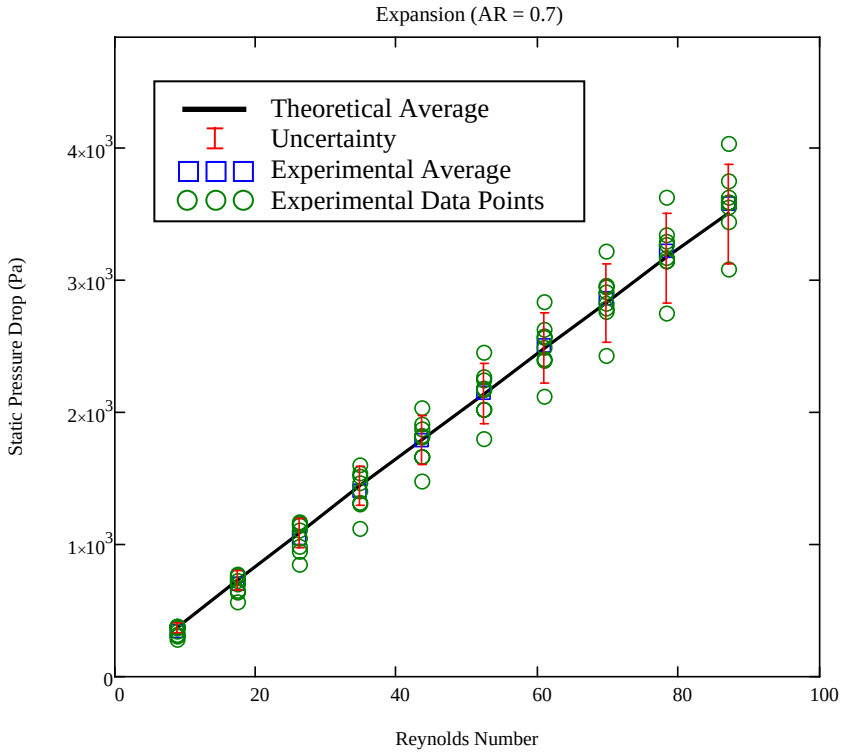
Expansion (AR = 0.7)
Theoretical Average
Uncertainty
Experimental Average
Experimental Data Points
Static Pressure Drop (Pa)
Reynolds Number
0
1×10^3
2×10^3
3×10^3
4×10^3
0
20
40
60
80
100

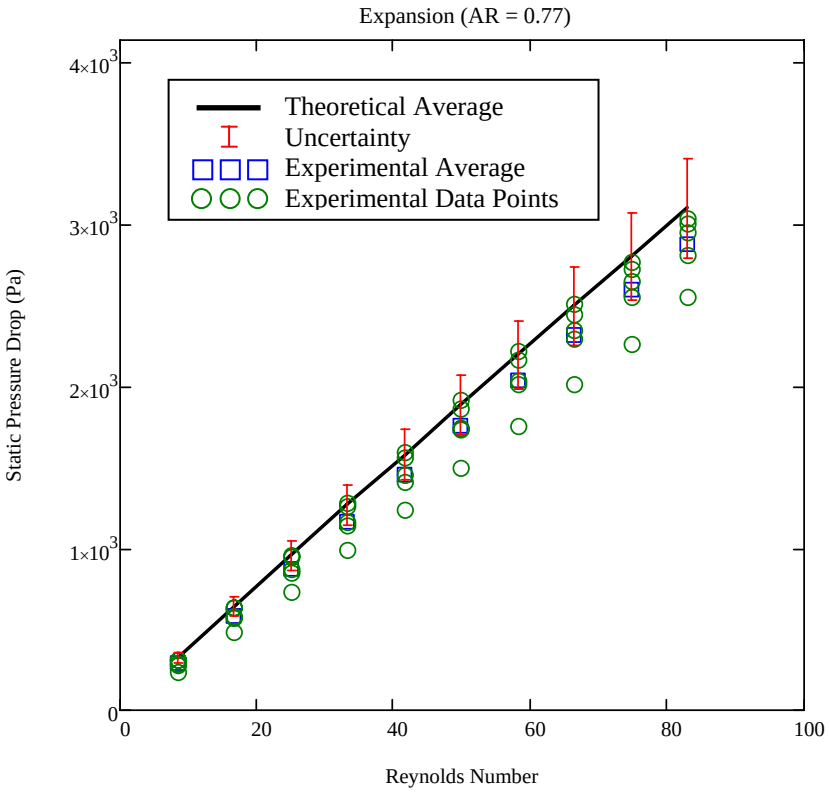
Expansion (AR = 0.77)
Theoretical Average
Uncertainty
Experimental Average
Experimental Data Points
Static Pressure Drop (Pa)
Reynolds Number
0
1×10^3
2×10^3
3×10^3
4×10^3
0
20
40
60
80
100

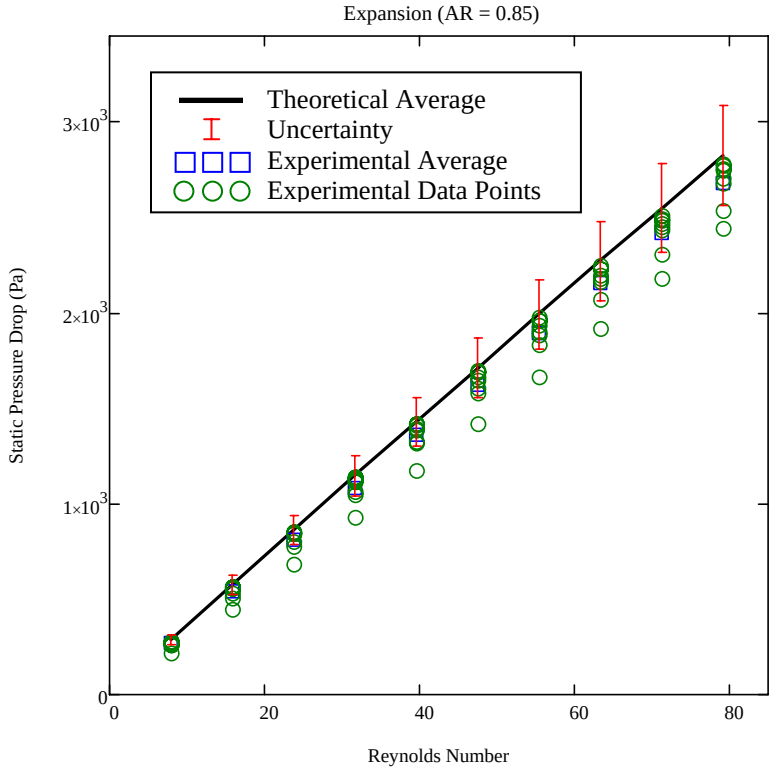
Expansion (AR = 0.85)
Theoretical Average
Uncertainty
Experimental Average
Experimental Data Points
Static Pressure Drop (Pa)
Reynolds Number
0
1×10^3
2×10^3
3×10^3
0
20
40
60
80

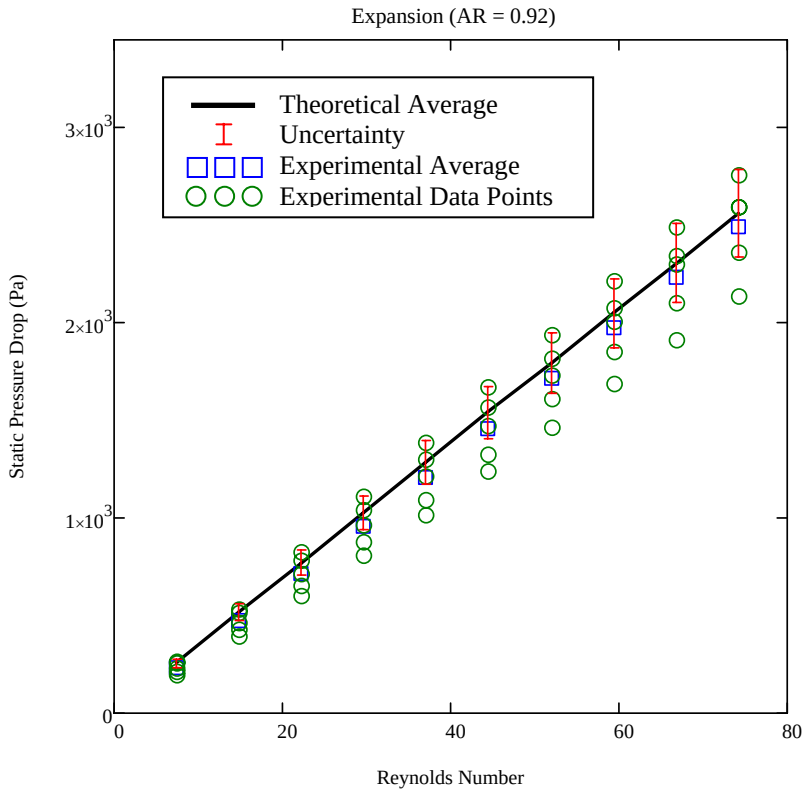
Expansion (AR = 0.92)
Theoretical Average
Uncertainty
Experimental Average
Experimental Data Points
Static Pressure Drop (Pa)
Reynolds Number
0
1×10^3
2×10^3
3×10^3
0
20
40
60
80

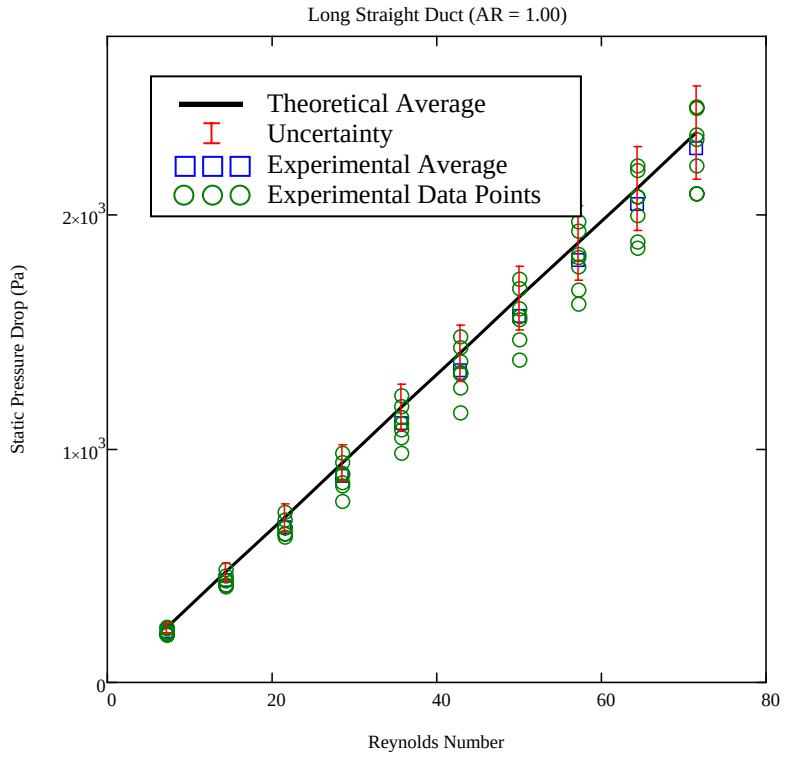
Long Straight Duct (AR = 1.00)
Theoretical Average
Uncertainty
Experimental Average
Experimental Data Points
Static Pressure Drop (Pa)
Reynolds Number
0
1×10^3
2×10^3
0
20
40
60
80

APPENDIX C: ADDITIONAL PLOTS FOR CONTRACTION TESTS

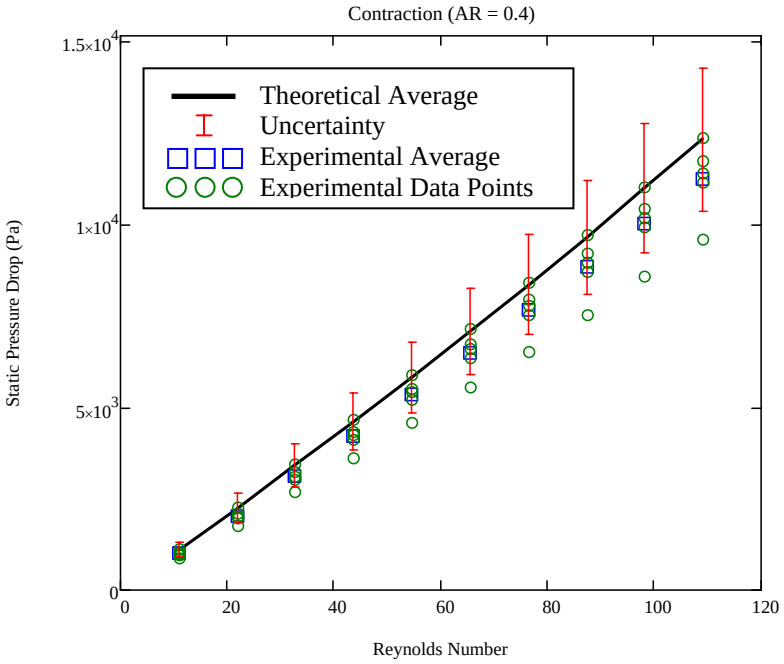

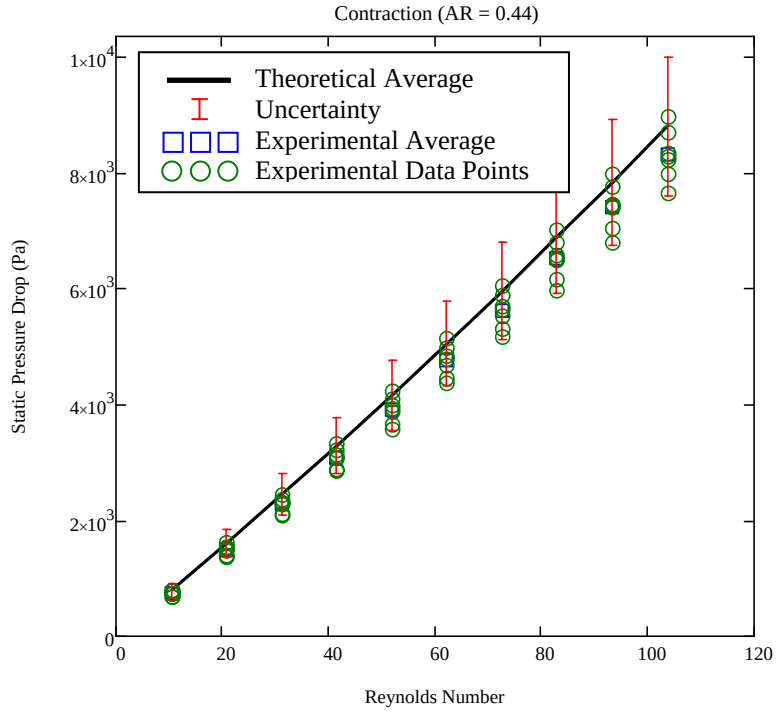

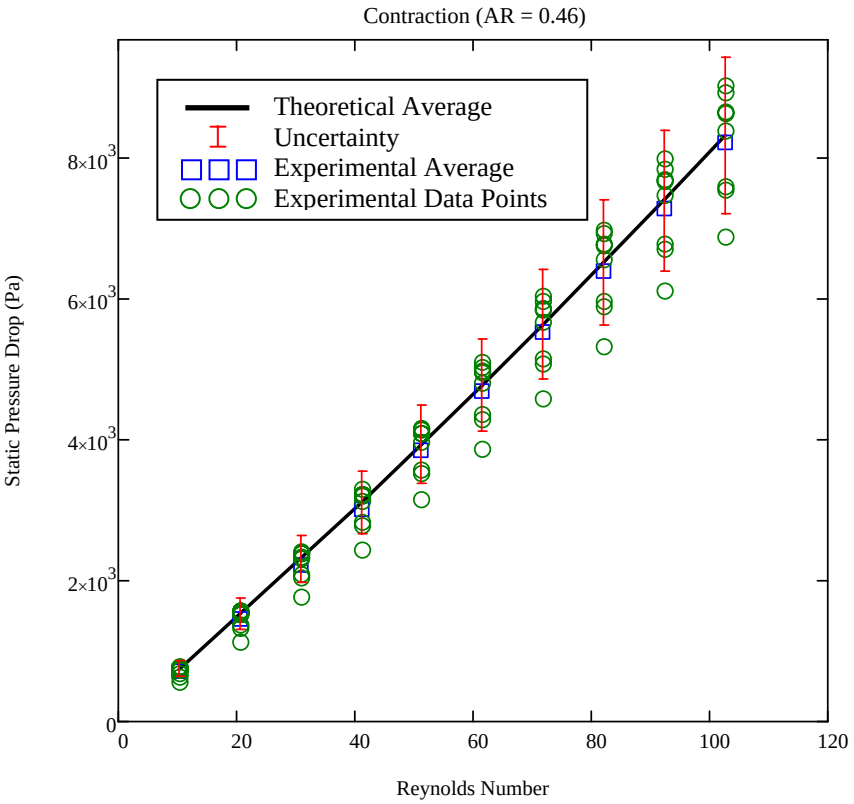
Contraction (AR = 0.46)
Theoretical Average
Uncertainty
Experimental Average
Experimental Data Points
Static Pressure Drop (Pa)
Reynolds Number
0
2×10^3
4×10^3
6×10^3
8×10^3
0
20
40
60
80
100
120

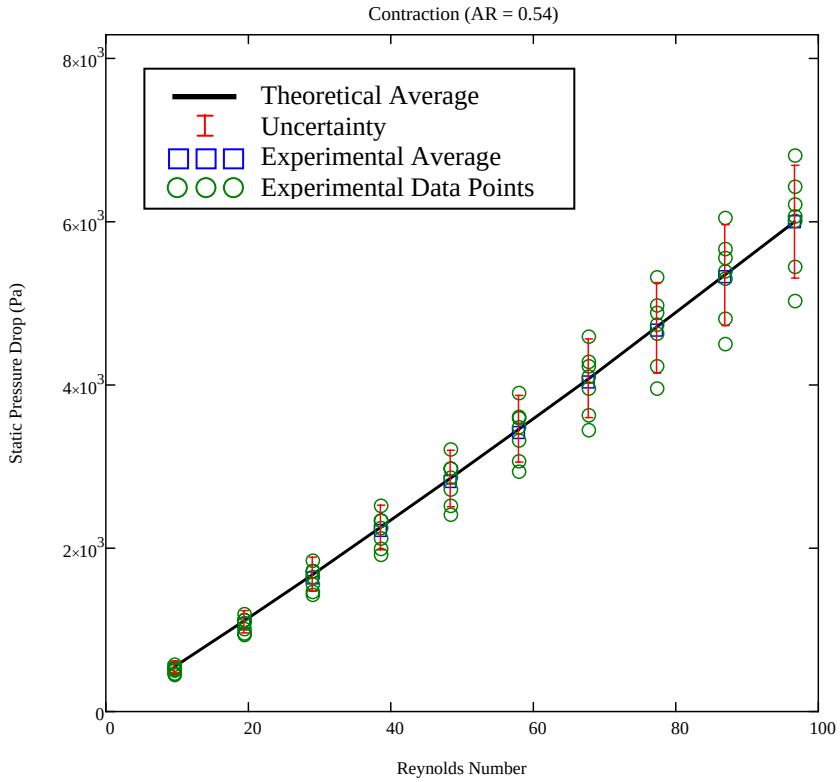
Contraction (AR = 0.54)
Theoretical Average
Uncertainty
Experimental Average
Experimental Data Points
Static Pressure Drop (Pa)
Reynolds Number
0
2×10^3
4×10^3
6×10^3
8×10^3
0
20
40
60
80
100

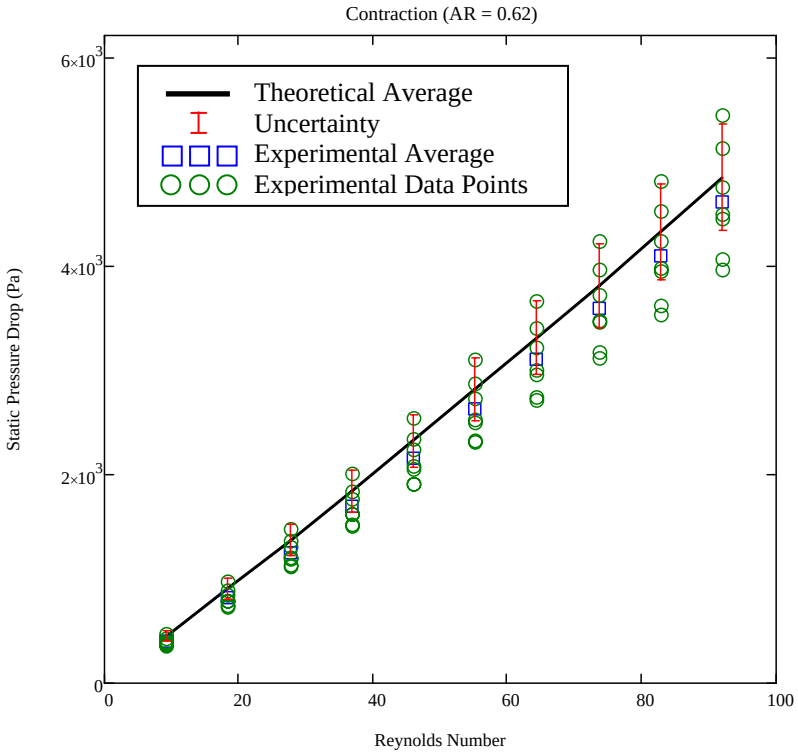
Contraction (AR = 0.62)
Theoretical Average
Uncertainty
Experimental Average
Experimental Data Points
Static Pressure Drop (Pa)
Reynolds Number
0
2×10^3
4×10^3
6×10^3
0
20
40
60
80
100

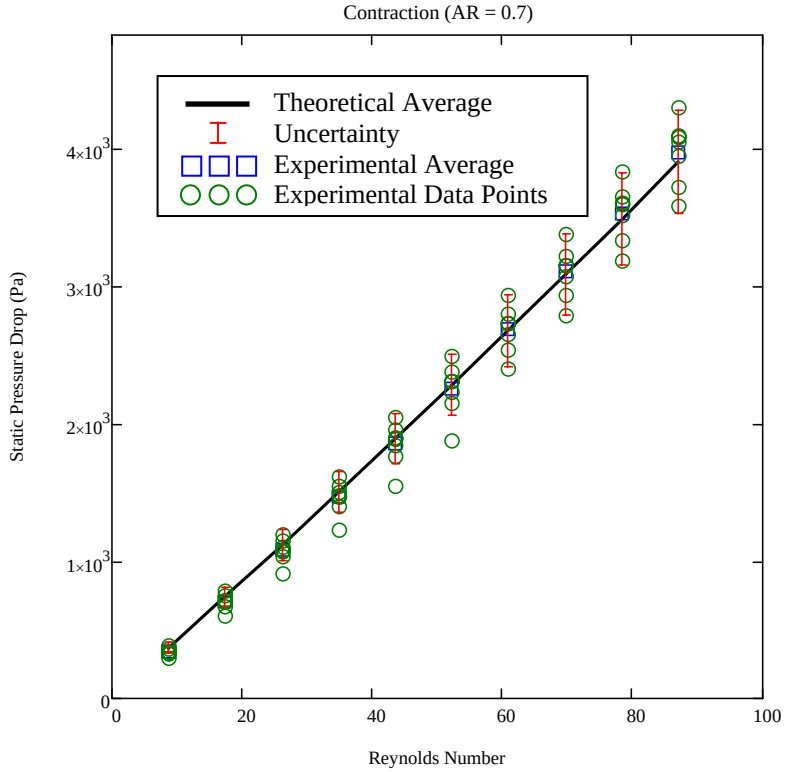
Contraction (AR = 0.7)
Theoretical Average
Uncertainty
Experimental Average
Experimental Data Points
Static Pressure Drop (Pa)
Reynolds Number
0
1×10^3
2×10^3
3×10^3
4×10^3
0
20
40
60
80
100

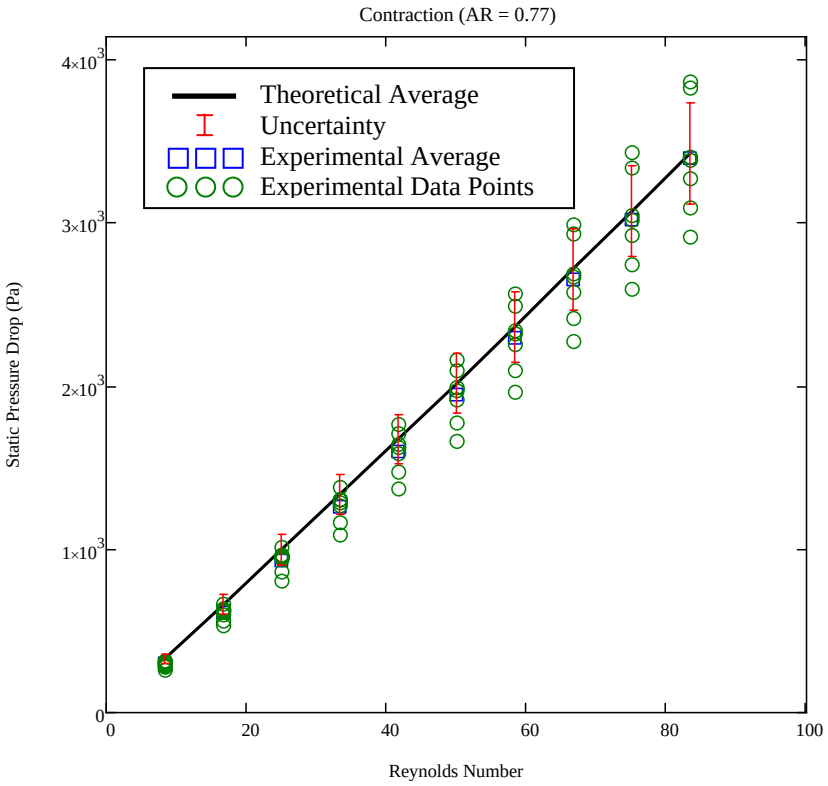
Contraction (AR = 0.77)
Theoretical Average
Uncertainty
Experimental Average
Experimental Data Points
Static Pressure Drop (Pa)
Reynolds Number
0
1×10^3
2×10^3
3×10^3
4×10^3
0
20
40
60
80
100

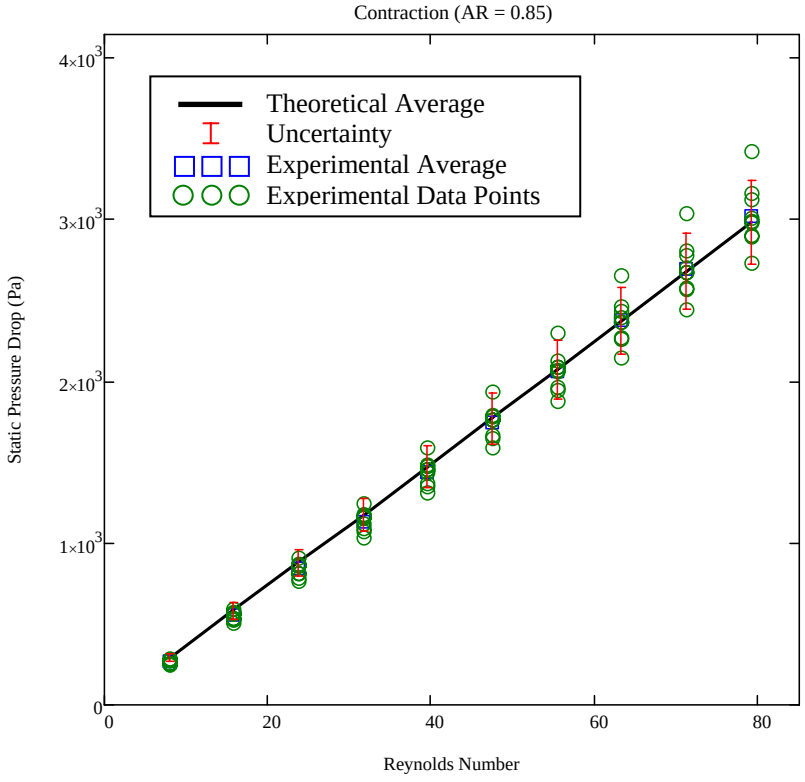
Contraction (AR = 0.85)
Theoretical Average
Uncertainty
Experimental Average
Experimental Data Points
Static Pressure Drop (Pa)
Reynolds Number
0
1×10^3
2×10^3
3×10^3
4×10^3
0
20
40
60
80

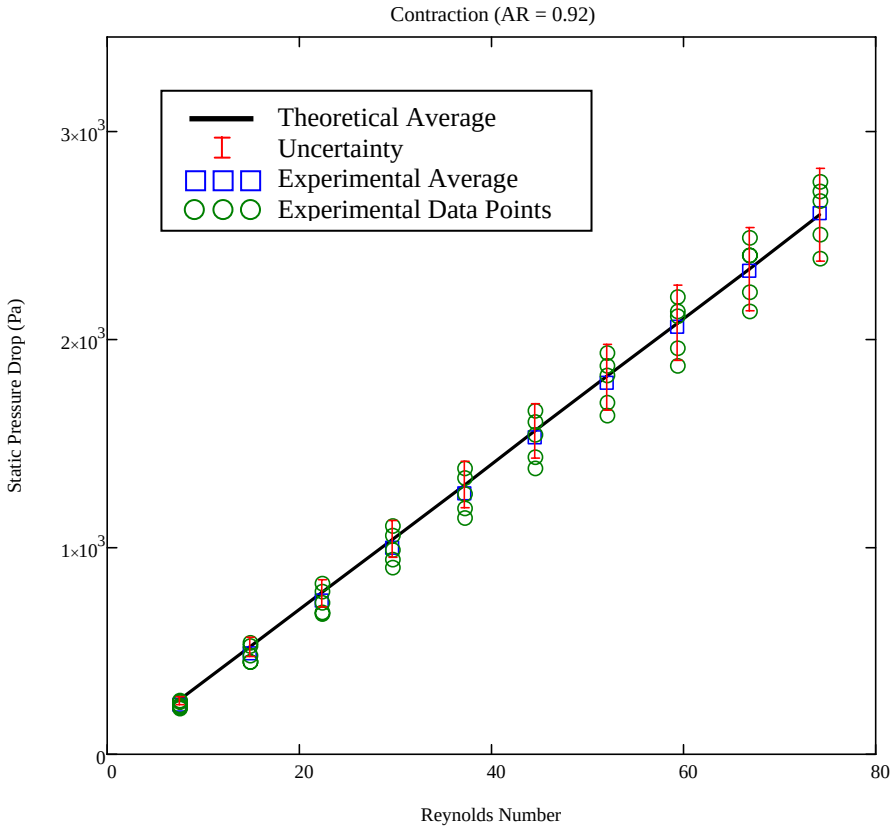
Contraction (AR = 0.92)
Theoretical Average
Uncertainty
Experimental Average
Experimental Data Points
Static Pressure Drop (Pa)
Reynolds Number
0
1×10^3
2×10^3
3×10^3
0
20
40
60
80

APPENDIX D: THESIS DEFENSE PRESENTATION

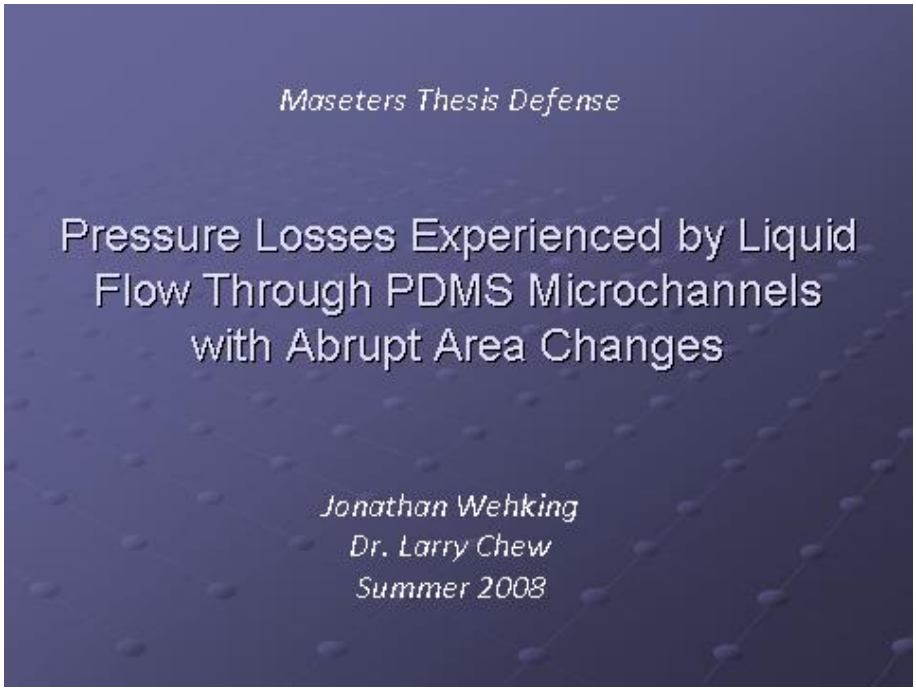

Vision and Scope

- Evaluate validity of macroscale internal, incompressible, viscous flow theory for microscale flow regime (Ch. 6 in Fox & McDonald, Ch.6 in White).

- Hansel (Spring 2008) — Sweeping Bends
- Wehking (Summer 2008) — Expansions/Contractions
- Hallenbeck (Fall 2008) — Nozzles/Diffusers

Prior Work (Parameter Space)

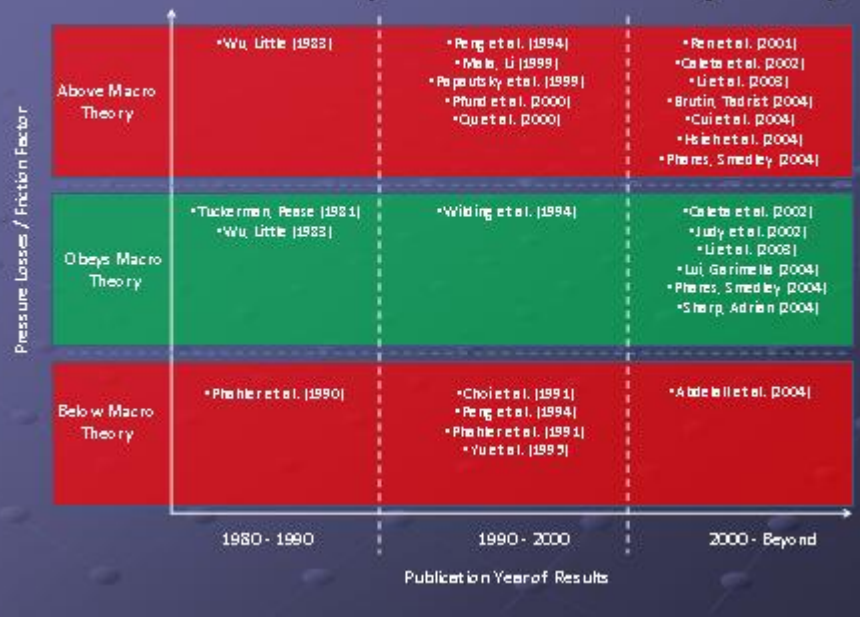

Compilation of Research Results

- Each shape represents a different group's experimental results.

$$C = \frac{(f \cdot Re)_{experimental}}{(f \cdot Re)_{theoretical}}$$

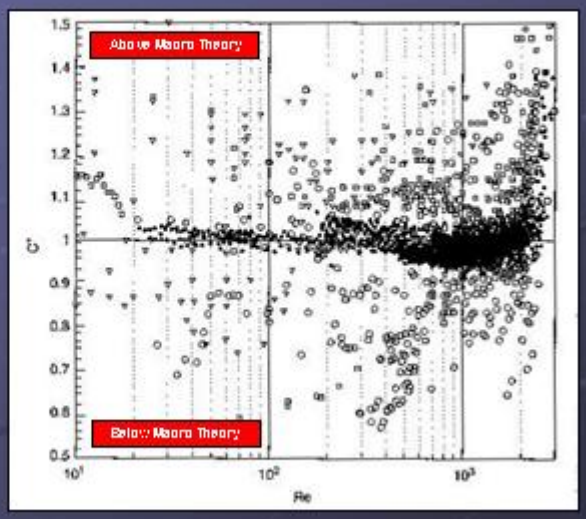

Prior Work – Expansion/Contraction

- Abdelall et al. (2004) conducted experiments on a single area ratio (micro machined stainless steel) channel of size order d_1=1.60mm d_2=0.84mm (AR=0.276).
- Focused mainly on two-phase flow at this scale.
- Data exhibited greater losses for contractions, and less losses for expansion than macro-scale theory predicts for single-phase (liquid) flow.
- Provided correlation for two phase contraction flow losses accounting for significant velocity slip.

Abdelall et al. Results

Expansion

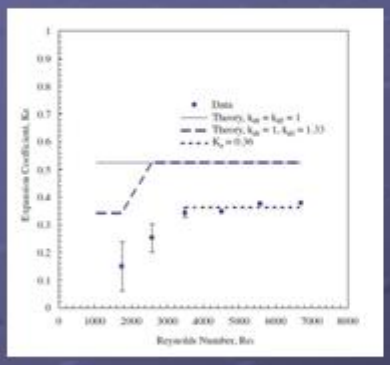

Experimental values fell consistently *below* macroscale predictions.

Contraction

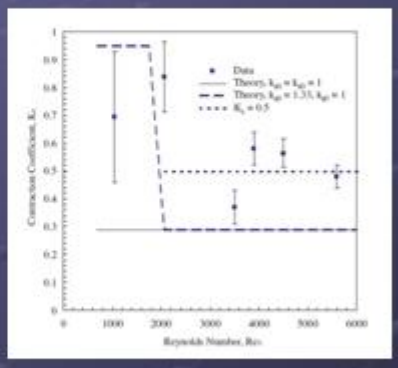

Experimental values fell consistently *above* macroscale predictions.

Deliverables for this Work

- Verify straight duct theory for the following parameters:
  - Re = 5 – 150
  - Width Size Range = 50um – 130um (square cross-section)
- Conduct analysis and comparison to macro-scale theory on single phase liquid flow through sudden expansion / contraction microchannels for the following parameters:
  - Re = 5 – 150
  - Area Ratios = 0.4 – 1.0
- Refine experimental set-up and test procedures for measuring pressure drop in microchannels.

Methodology

- Overview of macroscale hydrodynamic theory
- Channel design and layout
- Material selection
- Experimental set-up

Macro/Micro Gas Regime

Knudsen Number (Kn): Dimensionless quantity to test whether continuum assumption holds or if statistical analysis must be used (DSMC or MD).

$$Kn = \gamma / L_s$$

(γ = mean free path of gas, L_s = channel dimension)

$10 < Kn$	Free molecular Flow
$10^{-1} < Kn < 10$	Transitional flow regime (Macro theory no longer valid)
$10^{-3} < Kn < 10^{-1}$	Modified slip BCs
$Kn < 10^{-3}$	Continuum assumptions valid

Macro/Micro Fluid Regime

Lattice Spacing (δ): Equivalent replacement for γ in Kn calculations when considering fluids.

$$\delta = (V_l / N_A)^{1/3}$$

(V_l = Molar Volume, N_A = Avogadro's Number)

(δ = 0.3 nm for water)

Equivalent Knudsen Number calculations for water:

Kn ~ 3 x 10^{-4} (1μm gap)

Kn ~ 6 x 10^{-6} (50μm gap)

Lower size limit for continuum mechanics assumption ~ 3 nm

Macro-scale fluid mechanics should adequately describe flow.

Macroscale Flow Mechanics

- Major head loss equation due to frictional effects:

$$H_{loss\ major} = f \cdot \frac{L}{D} \cdot \frac{\rho V^2}{2}$$

- Darcy friction factor for rectangular flow cross-section:

$$f = \frac{1}{Re} \cdot \frac{64}{\frac{2}{3} + \frac{11}{24} \cdot \frac{h}{w}\left(2 - \frac{h}{w}\right)}$$

- Bernoulli equation factoring in major head loss:

$$P_1 + \frac{1}{2} \cdot \rho V_1^2 = P_2 + \frac{1}{2} \cdot \rho V_2^2 + H_{loss\ major}$$

Minor Loss Consideration

- Losses due to Sudden Expansion / Contraction:

$$H_{loss,minor} = \frac{1}{2} \cdot K \cdot V_{small}^{2}$$

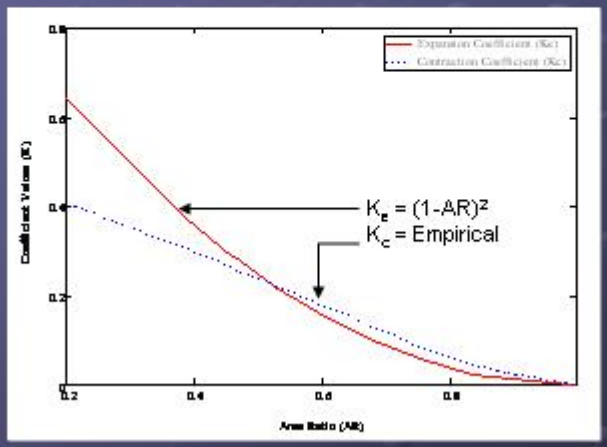

Final Theoretical Prediction Equation

- Final form of the Bernoulli equation factoring in major and minor head losses:

$$p_1 - p_2 = \left(\rho \frac{v^2}{2}\right)_{area_2} - \left(\rho \frac{v^2}{2}\right)_{area_1} + \left(\rho \cdot K \frac{v^2}{2}\right)_{area_{small}} + \left(\rho f \cdot \frac{L}{D_h} \cdot \frac{v^2}{2}\right)_{area_1} + \left(\rho f \cdot \frac{L}{D_h} \cdot \frac{v^2}{2}\right)_{area_2}$$

Dynamic Pressures | Minor Losses | Major Losses

Test Section Layout

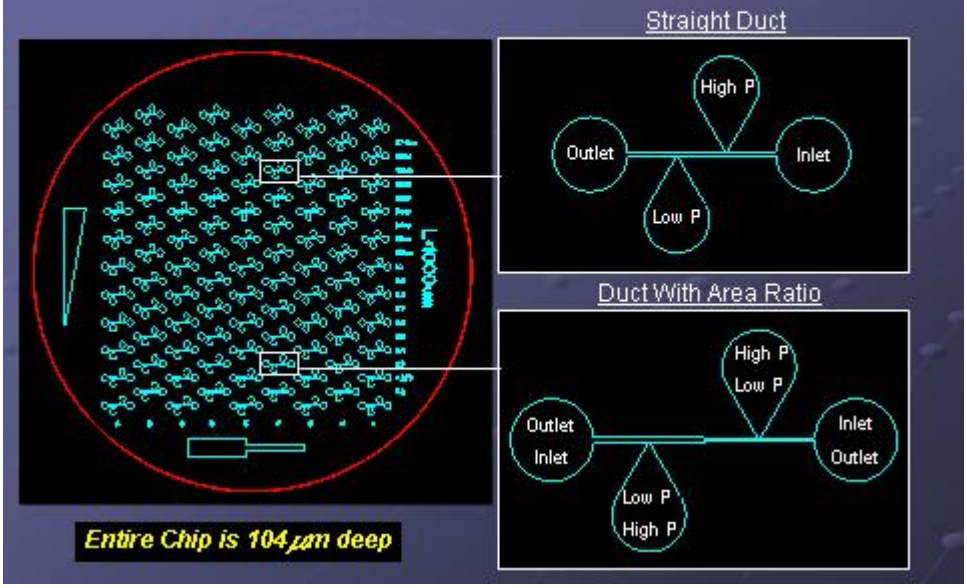

Test Section Material

- PDMS: Polydimethyl(siloxane)
  - Rubbery properties
  - Transparent
  - Low thermal conductivity
- Photoresist is hardened on silicone wafer, and PDMS is poured (cast) on top.
- Cured PDMS is peeled off, then O_2-Plasma bonded (irreversibly) to a blank slab of PDMS.
- Commercial Name: RTV615
- Manufactured By Stanford Microfluidics Foundry

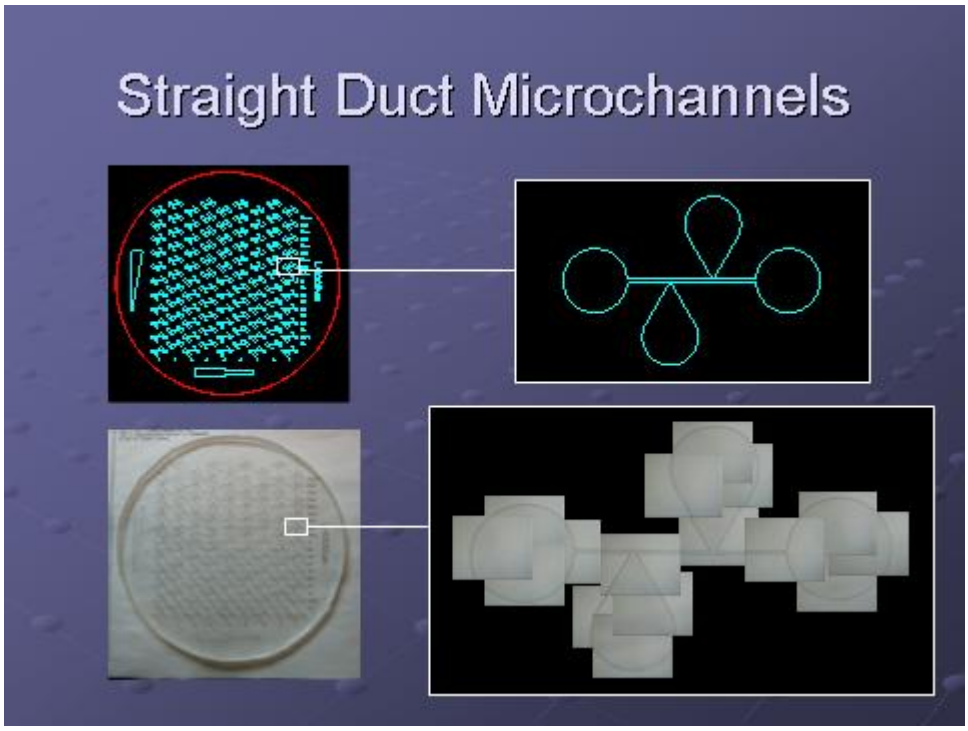
Straight Duct Microchannels

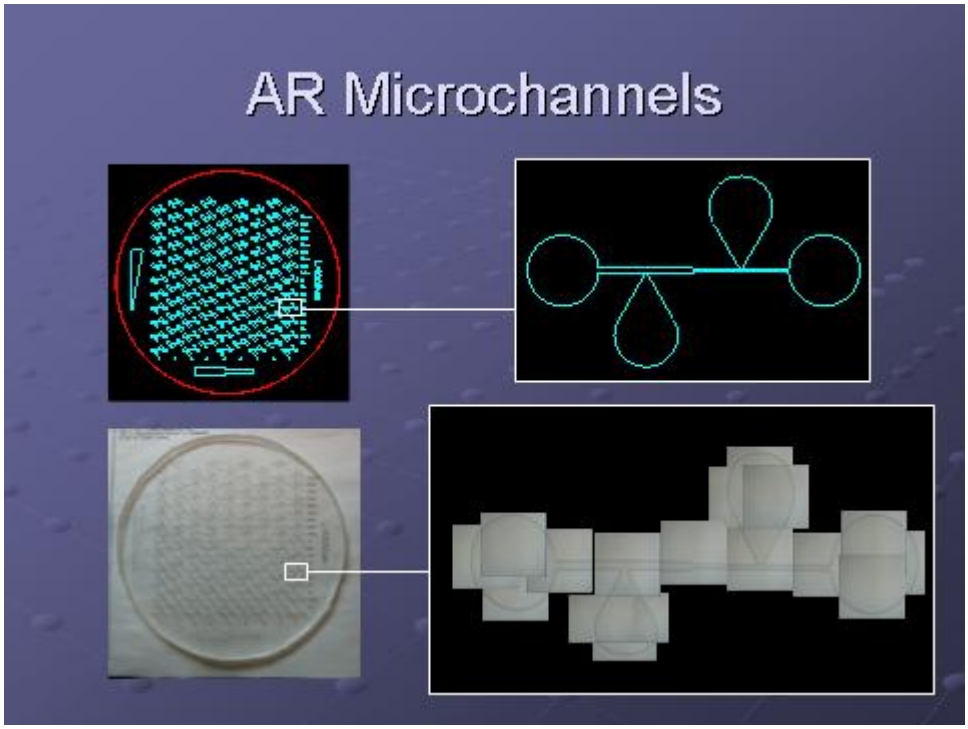
AR Microchannels

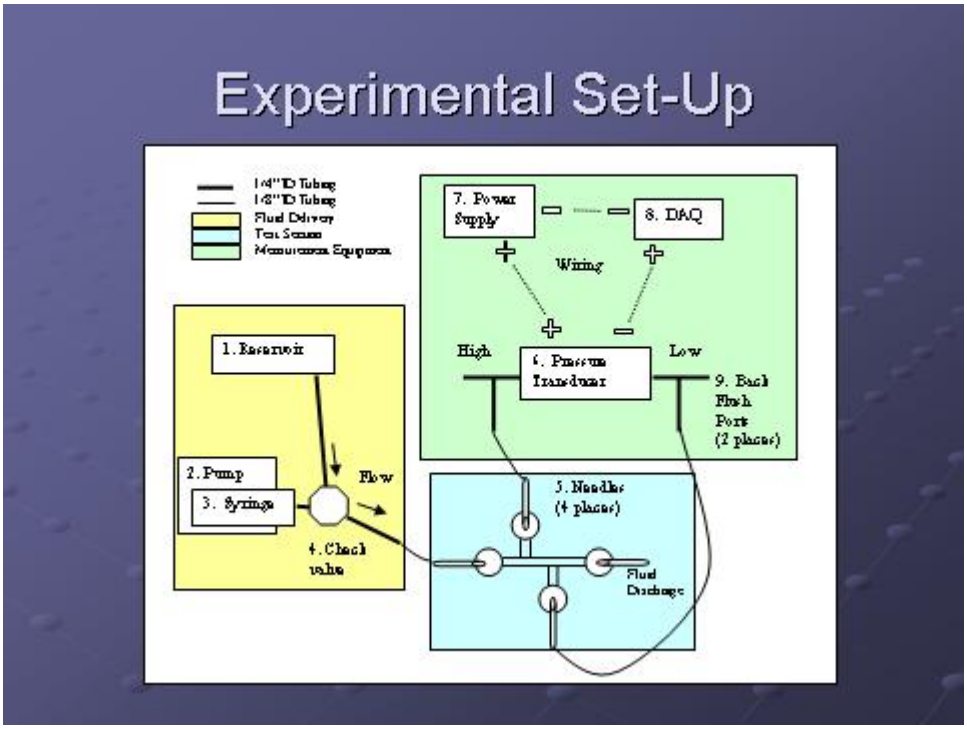
Experimental Set-Up
1/4" ID Tubing
1/8" ID Tubing
Fluid Delivery
Test Section
Measurement Equipment
7. Power Supply
8. DAQ
Wiring
High
6. Pressure Transducer
Low
9. Back Flush Port (2 places)
1. Reservoir
2. Pump
3. Syringe
Flow
4. Check valve
5. Needles (4 places)
Fluid Discharge

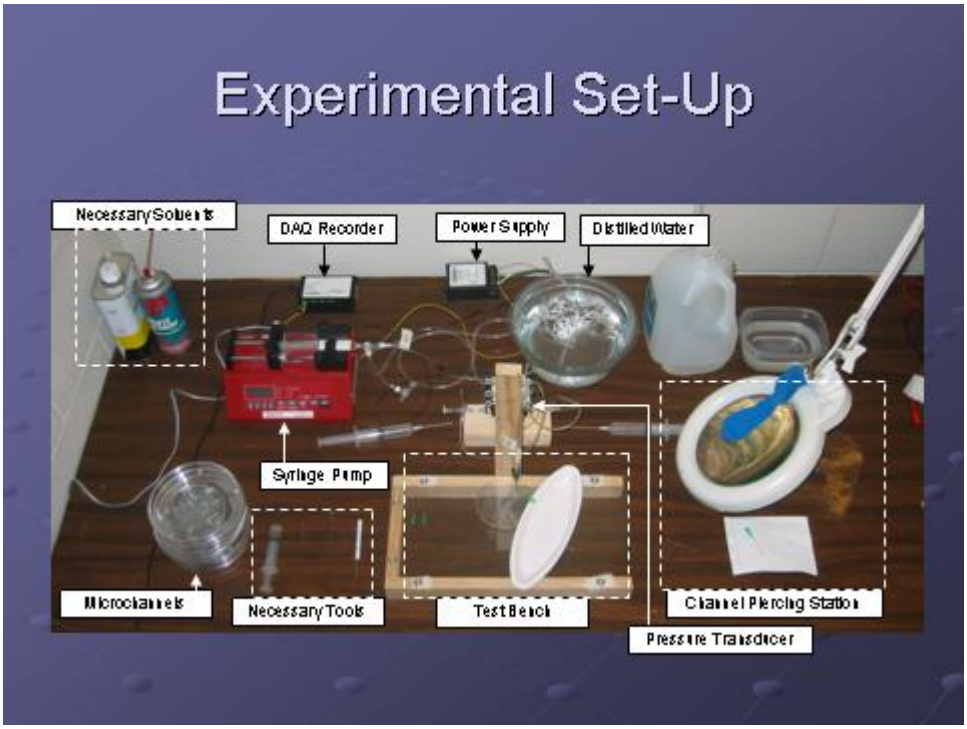
Experimental Set-Up
Necessary Solvents
DAQ Recorder
Power Supply
Distilled Water
Syringe Pump
Microchannels
Necessary Tools
Test Bench
Channel Piercing Station
Pressure Transducer

Key Test Equipment

- Fluid Delivery
  - Braintree Scientific Syringe Pump
    - Programmable flow rates & dispensed volumes
    - Flow Range Utilized = 50μL/min – 500μL/min
- Data Acquisition
  - Omega Voltage Recorder
- Pressure Transducer
  - Omega 2psid (differential pressure)

Transducer Calibration

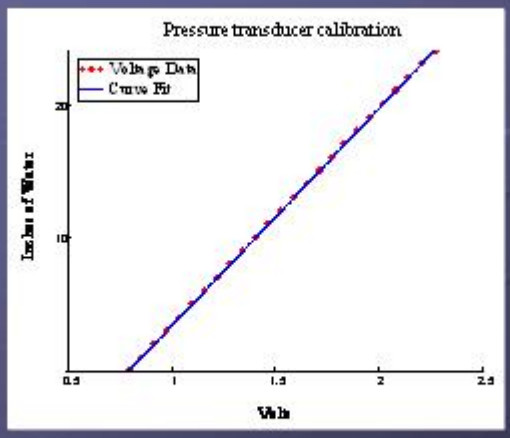

- Calibrated using U-Tube water manometer
- R^2 = 0.9999 correlation obtained

Typical Data Set

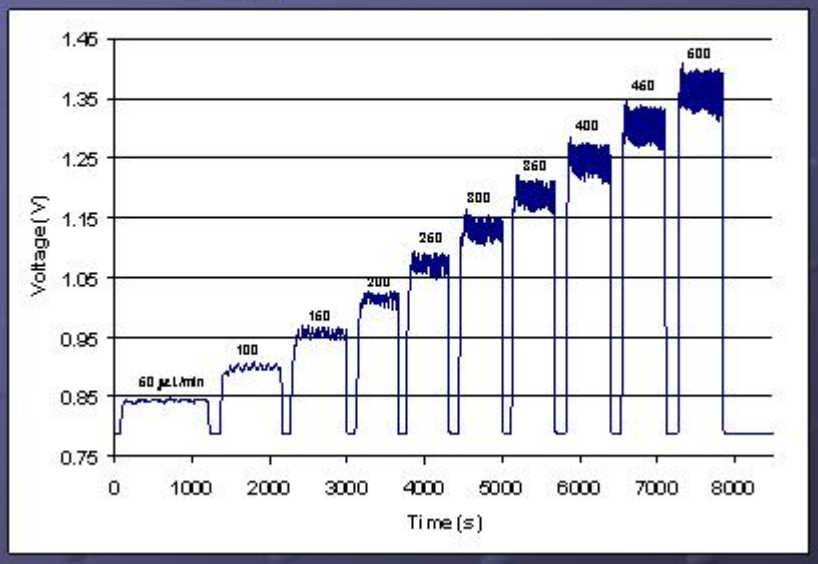

Results

- Importance of Technique
- Data Tendencies
- Manufacturing Considerations
- Discoveries / Conclusions

Regarding Technique

- Great care had to be taken in piercing the top layer of PDMS.
- Handling too vigorously resulted in separation between the PDMS slabs (inducing channel leakage).

Data Tendencies - Leakage

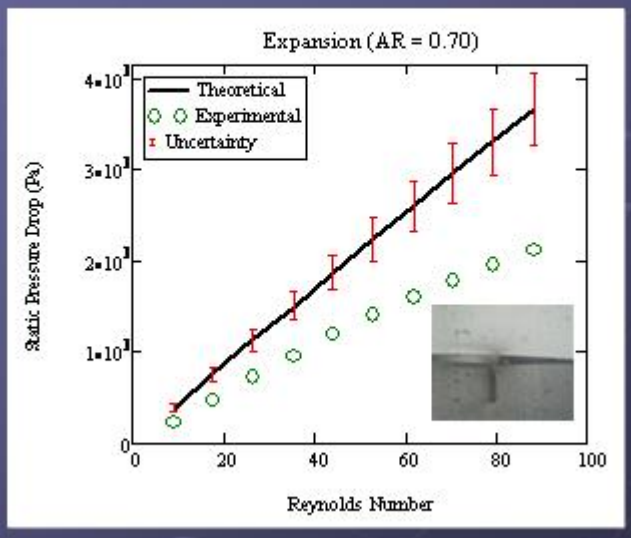

Data Tendencies - Bubbles

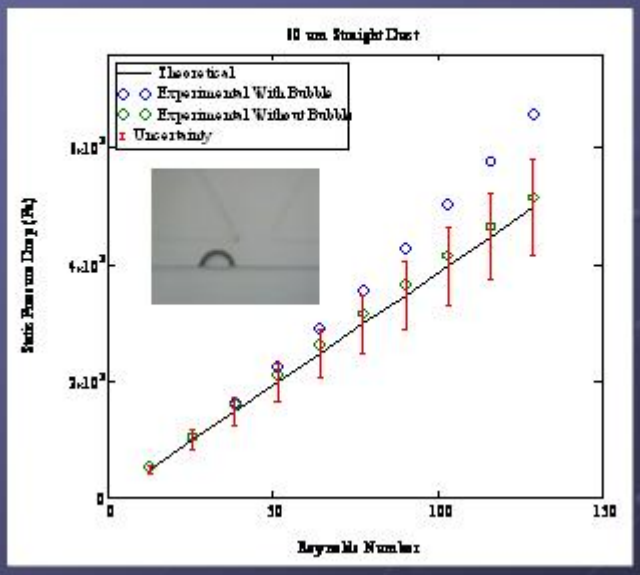

Resulting Zones of Error

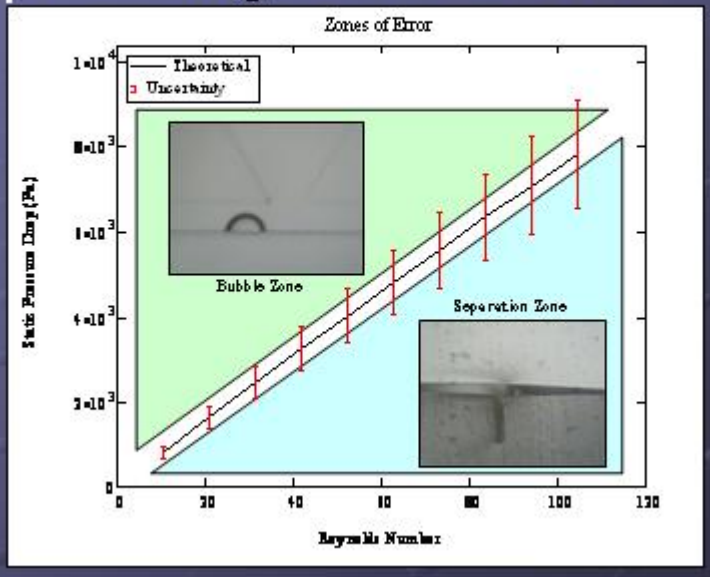

Possible Explanation of Anomalies

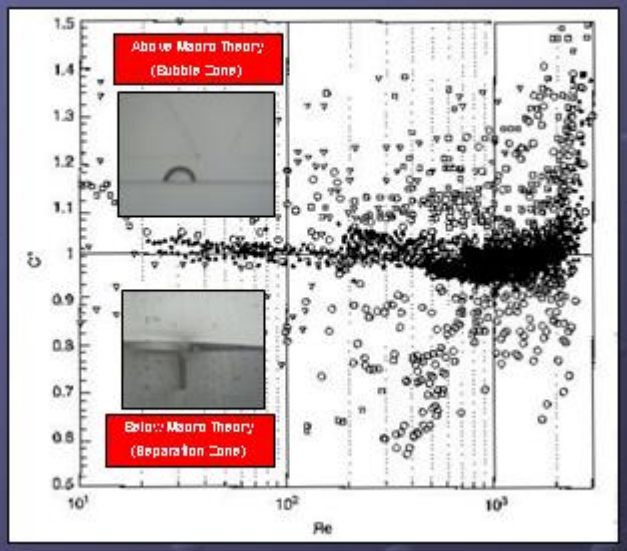

Manufacturing Considerations

- Aspect ratio limitations (5:1).
- Up to a 30μm change in channel dimensions.
- Rounding of sharp corners.

Straight Duct – 50μm

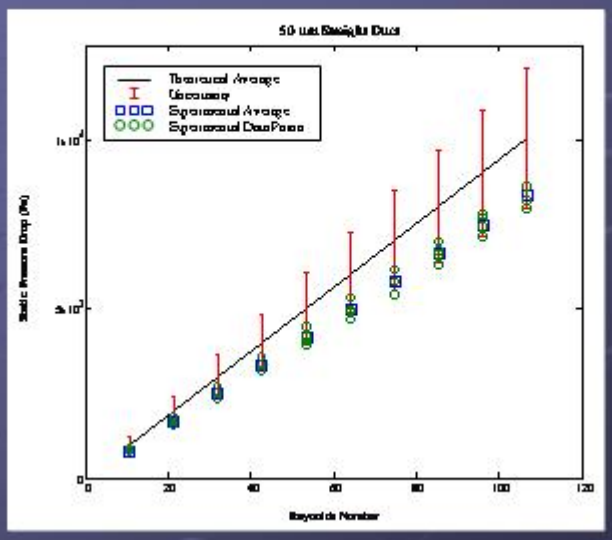

Straight Duct – 70μm

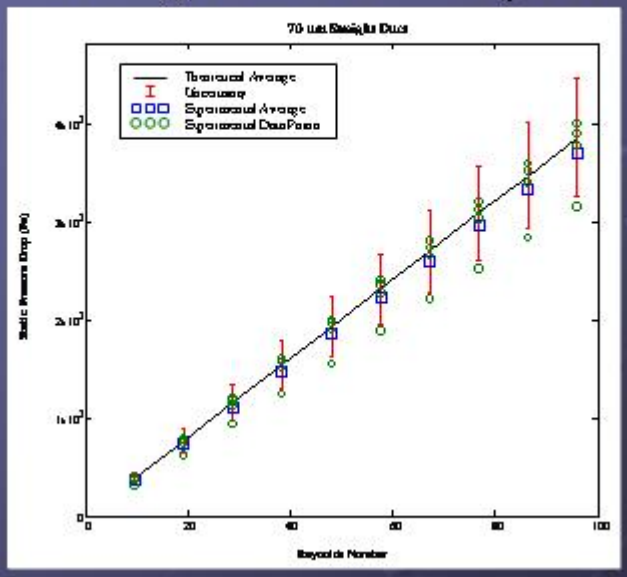

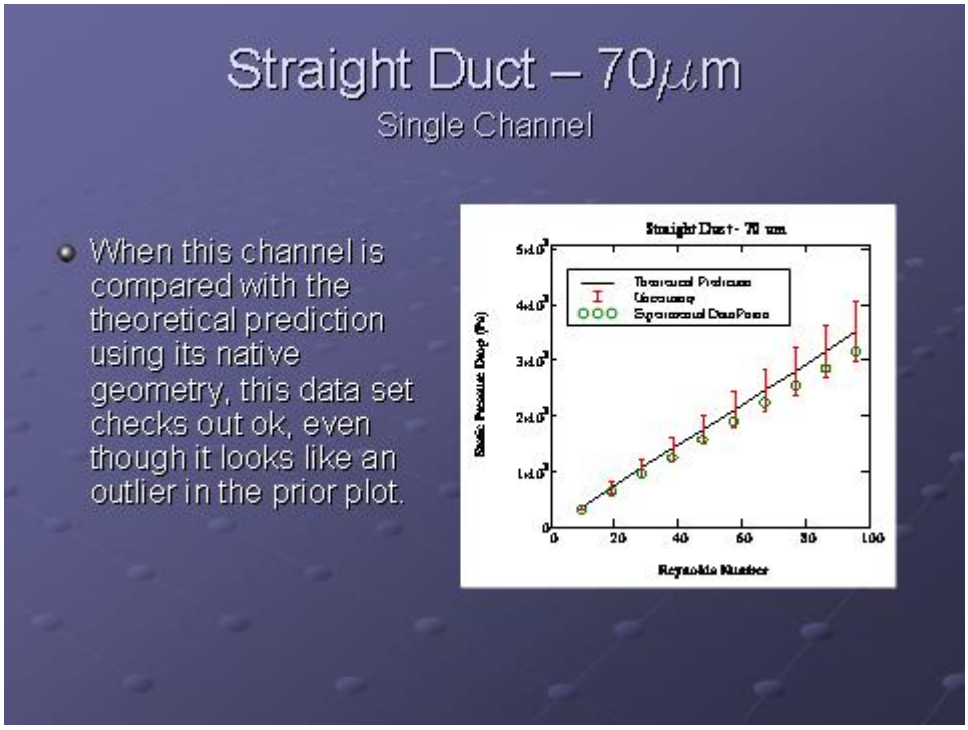

See Appendix A for additional straight duct plots.

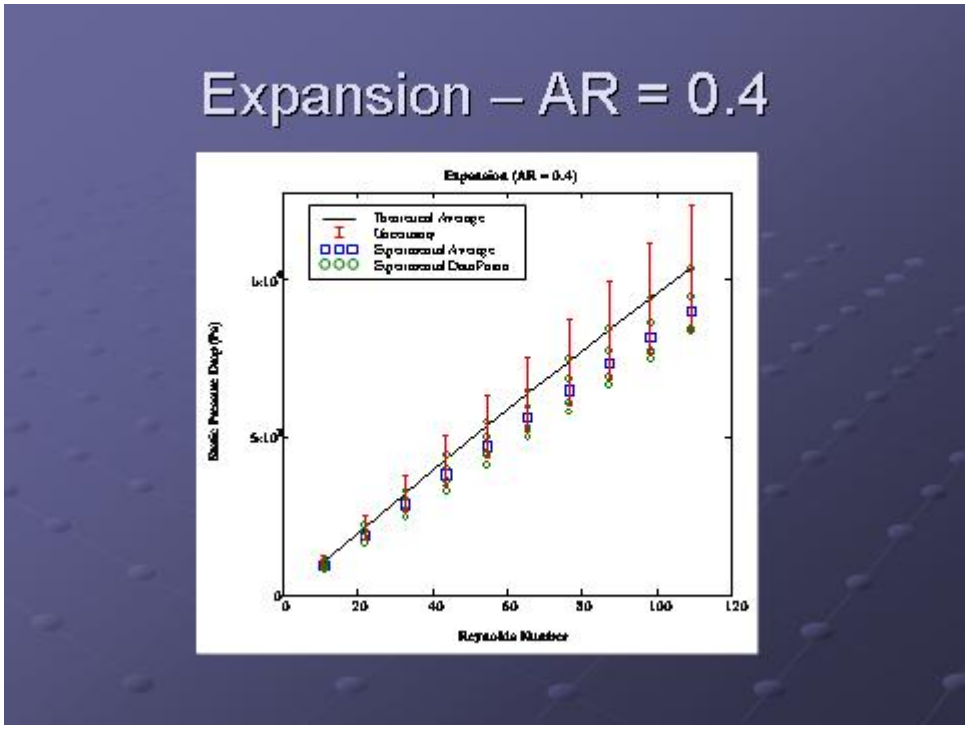

See Appendix B for additional expansion plots.

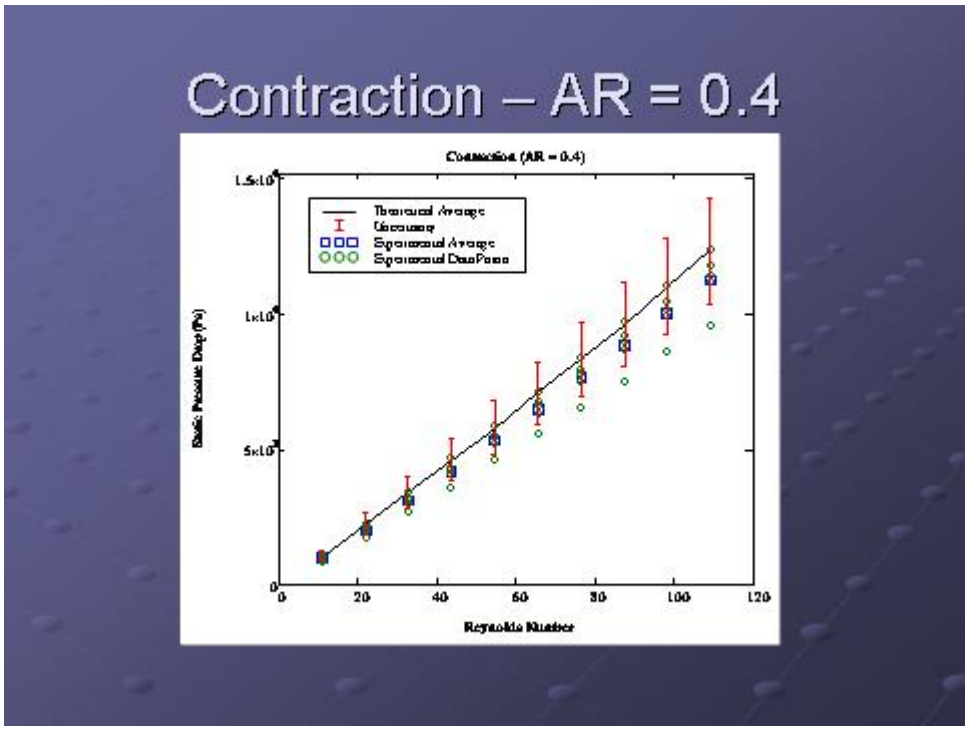

See Appendix C for additional contraction plots.

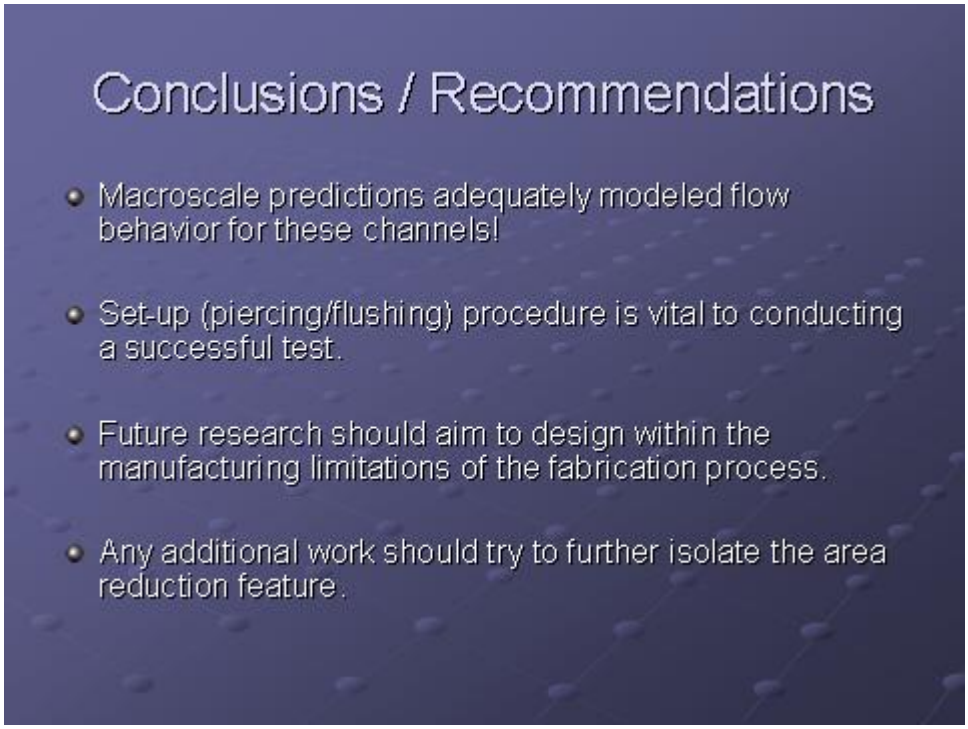

Contributions to the Field

- Shown that macroscale predictions adequately predict flow behavior for the following parameters:
  - Straight duct size range: 50μm – 130μm
  - Area ratio range (sting above channel width): 0.4 – 1.0
  - Reynolds number range: 5 – 130
- Developed and refined a precision piercing/flushing technique for microchannels cast in PDMS.
- Provided possible explanations for why prior research has shown deviation from macroscale predictions (bubbles/separation).

RERFERENCES

[1] J. C. McDonald, D. C. Duffy, J. R. Anderson, D. T. Chiu, H. Wu, O. J. A. Schueller, and G. M. Whitesides, "Fabrication of microfluidic systems in poly(dimethylsiloxane)," *Electrophoresis*, vol. 21, pp. 27-40, 2000.

[2] P. Gravesen, J. Branebjerg, and O. S. Jensen, "Microfluidics - a review," *J. Micromech. Microeng.*, vol. 3, pp. 168-182, 1993.

[3] D. Laser and J. Santiago, "A review of micropumps," *Journal of Micromechanics and Microengineering*, vol. 14, pp. R35-R64, 2004.

[4] F. F. Abdelall, G. Hahn, S. M. Ghiaasiaan, S. I. Abdel-Khalik, S. S. Jeter, M. Yoda, and D. L. Sadowski, "Pressure drop caused by abrupt flow area changes in small channels," *Experimental Thermal and Fluid Science*, vol. 29, pp. 425-434, 2005.

[5] F. M. White, *Fluid Mechanics*, 6 ed. New York: McGraw-Hill, 2008.

[6] R. W. Fox, A. T. McDonald, and P. J. Pritchard, *Introduction to Fluid Mechanics*, 5th ed: John Wiley & Sons, Inc., 2004.

[7] K. V. Sharp, R. J. Adrian, J. G. Santiago, and J. I. Molho, *The MEMS Handbook*, vol. 1, 2 ed. Boca Raton: CRC Press - Taylor and Francis, 2006.

[8] C. Rands, B. W. Webb, and D. Maynes, "Characterization of transition to tubulence in microchannels," *International Journal of Heat and Mass transfer*, vol. 49, pp. 2924-2930, 2006.

[9] D. Xu, T. Y. Ng, L. S. Pan, K. Y. Lam, and H. Li, "Numerical simulations of fully developed tubulent liquid flows in micro tubes," *J. Micromech. Microeng.*, vol. 11, pp. 157-180, 2001.

[10] J. Ducre´e, S. Haeberle, T. Brenner, T. Glatzel, and R. Zengerle, "Patterning of flow and mixing in rotating radial microchannels," *Microfluid Nanofluid*, vol. 2, pp. 97-105, 2006.

[11] A. P. Sudarsan and V. M. Ugaz, "Fluid mixing in planar spiral microchannels," *The Royal Society of Chemistry*, pp. 74-82, 2006.

[12] A. Goullet, I. Glasgow, and N. Aubry, "Effects of microchannel geometry on pulsed flow mixing," *Mechanics Research Communications*, vol. 33, pp. 739-746, 2006.

[13] M. Niklas, M. Favre-Marinet, and D. Asendrych, "Numerical simulation of microchannel network with complex geometry," *Bulletin of the Polish Academy of Sciences*, vol. 53, 2005.

[14] J. Koo and C. Kleinstreuer, "Liquid flow in microchannels: experimental observations and computational analyses of microfluidics effects," *J. Micromech. Microeng.*, vol. 13, pp. 568-579, 2003.

[15] G. P. Celata, M. Cumo, S. McPhail, and G. Zummo, "Characterization of fluid dynamic behaviour and channel wall effects in microtube," *International Journal of Heat and Fluid Flow*, vol. 27, pp. 135-143, 2006.

[16] M. E. Steinke and S. G. Kandlikar, "Single-phase liquid friction factors in microchannels," presented at ICMM05: Third International Conference on Microchannels and Minichannels, University of Toronto, 2005.

[17] W. Qu and I. Mudawar, "Experimental and Computational Investigation of Flow development and Pressure Drop in a Rectangular Micro-channel," *Journal of Electronic Packaging*, vol. 128, pp. 1-9, 2006.

[18] M. Bahrami, M. M. Yovanovich, and J. R. Culham, "Pressure Drop of Fully Developed Laminar Flow in Rough Microtube," *Journal of Fluids Engineering*, vol. 128, pp. 632-637, 2006.

[19] C. Hansel, "Mapping of Pressure Losses Through Microchannels With Sweeping-Bends of Various Angle and Radii," in *College of Engineering and Computer Science - Department of Mechanical, Materials, and Aerospace Engineering*, vol. Master of Science. Orlando: University of Central Florida, 2008, pp. 134.

[20] N.-T. Nguyen and S. T. Wereley, *Fundamentals and Applications of Microfluidics*, Second Edition ed: Artech House, Inc., 2006.

[21] V. L. Streeter, *Handbook of Fluid Dynamics*. New York: McGraw-Hill, 1961.

[22] D. C. Duffy, J. C. McDonald, O. J. A. Schueller, and G. M. Whitesides, "Rapid Prototyping of Microfluidic Systems in Poly(dimethylsiloxane)," *Department of Chemistry and Chemical Biology*, vol. 70, 1998.

[23] M. Morra, E. Occhiello, R. Marola, F. Garbassi, P. Humphrey, and D. Johnson, "On the aging of oxygen plasma-treated polydimethylsiloxane surfaces," *Journal of Colloid and Interface Science*, vol. 137, pp. 11-24, 1990.